A Thermal Expansion Coefficient Study of Several Magnetic Spin Materials via Capacitive Dilatometry

by

Kevin Liu

A thesis
presented to the University of Waterloo
in fulfillment of the
thesis requirement for the degree of
Master of Science
in
Physics

Waterloo, Ontario, Canada, 2013

I hereby declare that I am the sole author of this thesis. This is a true copy of the thesis, including any required final revisions, as accepted by my examiners.

I understand that my thesis may be made electronically available to the public.

Abstract

The work presented in this thesis detail the measurement of the thermal expansion coefficient of three magnetic spin materials. Thermal expansion coefficient values were measured by capacitive dilatometry in several key low ($T < 250$ K) temperature regions specific to each material. This thesis is separated into several key parts.

The first part establishes the theory behind observing phase transitions through the thermal expansion coefficient. Beginning with the classical definitions of the specific heat, compressibility and thermal expansion coefficient, the three properties are related using a property known as the Grüneisen parameter. To first order, the parameter allows phase transitions to be observed by the thermal expansion coefficient.

The second part introduces capacitive dilatometry; a technique used to measure the thermal expansion coefficient. Three capacitive dilatometer devices are presented in this section. The silver compact dilatometer, the fused quartz dilatometer and the copper dilatometer. Each device discusses merits and weaknesses to their designs. Particular focus is made on the fused quartz dilatometer which was built during the duration of this thesis.

The third part presents research on three magnetic spin materials; $LiHoF_4$, $Tb_2Ti_2O_7$ and $Ba_3NbFe_3Si_2O_{14}$. These materials are studied individually focusing on specific aspects.

$LiHoF_4$, a candidate material for the transverse field Ising model, provides insight to quantum phase transitions. Thermal expansion coefficient and magnetostriction along the c-axis for $T \approx 1.3-1.8$ K and transverse field $H_t \approx 0-4$ T were measured extracting critical points for a $H_t - T$ phase diagram. Existing thermal expansion coefficient measurements had evidence of possible re-entrant behaviour. With a high density of low transverse field critical points it was established that $LiHoF_4$ showed no evidence of re-entrant behaviour.

The highly debated material $Tb_2Ti_2O_7$ has a rich, controversial low temperature behaviour. Originally believed to be a spin liquid, specific heat results propose a scenario involving a sample composition dependent ordered state. Still under considerably attention, thermal expansion coefficient measurements were performed for $T < 1$ K. The results are interpreted to either fit into the proposed scenario or provide evidence for an alternate scenario.

The material $Ba_3NbFe_3Si_2O_{14}$ exhibits a magnetoelectric multiferroic phase below $T_N \approx$ 27 K; a phase where magnetic and electric order simultaneously exist. The formation of this phase is believed to have a similar structural shift observed in hexagonal perovskite multiferroic materials. The ferroelectric ordering in those materials are brought about through a centrosymmetric to non-centrosymmetric structural shift. The thermal expan-

sion and thermal expansion coefficient coefficient along the a and c axis are measured for $T > T_N$ searching for a displacive structural phase transition.

Acknowledgements

This work would not have been completed if it weren't for the many people supporting me.

First and foremost, I would like to thank Rob Hill who has been my mentor for nearly four years. Having taken me in under his wing while an undergraduate and constantly teaching me through to my graduate studies must have been no easy task. I would not be where I am now without his guidance, effort and patience. His approach to supervising has given me a lot of independence in solving problems yet he is always there when help is needed. His insight towards experimental physics and dedication towards making the best quality measurements has given me an appreciation of what it truly means to be a professor and experimental physicist. I feel that I have learned at an exponential rate through both success and failure while working under his guidance. I am truly grateful and fortunate for the skills developed while working in his laboratory. It was an honour to work for him.

I would also like to thank my friend and colleague William Toews. Both he and I started with Rob around the same time and have been through the best and worst of it. His hard work and dedication towards his research was very admirable. The time we spent together both working and playing has been invaluable. I hope he had as much fun as I did.

When I first started, John Dunn, a graduate student of Rob showed me the ropes of experimental physics. During my undergraduate, he had taken time away from his own graduate program to mentor me. He showed me much of the day to day behind running and implementing experiments. For that I am truly thankful.

Many other people from the University of Waterloo helped complete many aspects of this thesis. I would like to thank my supervisory committee members Jan Kycia and Roger Melko for overseeing the progress of the graduate degree. Their input and advice regarding both theoretical and experimental aspects was invaluable. Special thanks go to Luke Yaraskavitch and Jeff Mason and the rest of the Kycia group for ensuring that liquid helium was available when needed. This thesis would not have been completed if it were not for the hard work from both Science Technical Services. From the machining group, Andrew Dubé for cutting the fused quartz components and general machining, Hiruy Haile for general machining and machine shop supervision and lastly Harmen Vander Heide for design consulting. Thanks also go to Kurnomir Dvorski and Zhenwen Wang of the electrical group for support with electrical components.

I would also like to thank the students who contributed to content presented in this thesis. Andrew Macdonald for his contributions to measuring $LiHoF_4$ and Garnet Akeyr for his participation in the development of the fused quartz dilatometer and aid in measuring $Ba_3NbFe_3Si_2O_{14}$.

Lastly I would like to thank friends and family for their unending support. In no particular order thanks go to Kier Von Konigslow, David Pomaranski, Benji Wales, Christopher McMahon, Kyle Denison and Patryk Gumann for the fun times. Much love to my mother, my father and sister for supporting me.

Dedication

This is dedicated to friends and family.

Table of Contents

List of Tables

List of Figures

Chapter 1

Introduction

Technology and material development have always gone hand in hand. An advancement in technology might come about from improving the performance of a material. For a case such as this, one can look back in history to the Iron Age. The first iron tools were hardly an improvement over bronze tools and did not become obsolete until iron was combined with carbon to make steel. Although improvements such as these are still important, attention has shifted toward developing materials with new properties to bring about better technology.

Consider a more recent development of technology through this method. The lithium battery set itself apart from other batteries for its long life credited to the use of lithium within the compound. However, being non-rechargeable and having relatively high cost made them unpopular in certain portable electronics. The development of the lithium ion battery was a monumental advancement in technology; a more durable and rechargeable version of the lithium battery. This was ultimately achieved by the development of a new lithium compound with a reversible reaction. It is material developments such as these that bring about new possibilities in technological advancement.

To the same degree, exotic phases in newly developed materials may bring about vast advances in technology. However, this is a tall order as many factors can alter the phase of a material; in particular the temperature. One such case are superconductors where a critical temperature divides the normal conducting phase and superconducting phase. With temperature as one of the major driving factors, it is imperative that similar temperature points in other exotic materials be determined. Through the measurement of thermal expansion coefficient, it is possible to determine these temperature points.

This thesis begins with the discussion of the theory behind observing phase transitions through the thermal expansion coefficient. From there, the experimental process of measuring the thermal expansion coefficient through capacitive dilatometry is presented. Lastly, three exotic magnetic spin materials are studied through the measurement of the thermal expansion coefficient. This thesis is structured in the following manner:

The first chapter briefly covers several aspects of classical thermodynamics eventually defining the thermal expansion coefficient. A relationship between specific heat and thermal expansion coefficient is drawn; a crucial development for the justification of measuring the thermal expansion coefficient.

The next chapter discusses capacitive dilatometry; a technique used to measure the thermal expansion coefficient. The merits and drawbacks of one existing and two new dilatometer devices used by the group are discussed. The chapter also outlines the assembly, calibration and implementation of the new devices.

The thermal expansion coefficient results of three different exotic magnetic spin materials are discussed in the next chapters. The first material $LiHoF_4$ was investigated at low transverse magnetic field strengths near the classical critical point. Previous thermal expansion coefficient measurements by the group showed strong evidence of re-emergent behaviour in this region. This work focused on increasing the point density of critical points in this region to verify this possibility.

Next, $Tb_2Ti_2O_7$ is studied at $T < 1$ K. Previous thermal expansion coefficient measurements by the group revealed a feature at approximately 100 mK. Since then, new information on the material has been published bringing about a renewed vigour to the study of this material. Higher resolution measurements of the thermal expansion coefficient verified the existence of a 100 mK feature and as well as a 500 mK feature previously unobserved by the group. This work presents two interpretations of the results.

The last material, $Ba_3NbFe_3Si_2O_{14}$ exhibits a magnetoelectric multiferroic phase below $T \approx 26$ K; a simultaneous existance of magnetic and ferroelectric ordering. This material is believed to undergo a structural shift to achieve such a state. Thermal expansion coefficient measurements along several crystallographic axes are measured in search for evidence of a displacive structural phase transition.

Supporting content found in the appendices include the schematics for the capacitive dilatometer devices and other supporting equipment. Tutorials on installing coaxial lines, using the Igor WaveMetrics analysis program and miscellaneous guides are also included.

Chapter 2

Theoretical Background

Imagine a situation where a pouch of water is placed in a freezer. The outcome of this situation is already known but contemplate how the situation would appear without this prior knowledge. That is, liquid water is placed in a freezer and some time later becomes a solid. Approaching this situation scientifically rules out any chemical change (as the pouch is completely inert and contains only water) yet there is a clear physical change. One would ask what quantifiable changes have occurred and what had caused them? One of several quantifiable property that distinguishes solid from liquid would be the density. As to the cause of the change, the reasonable and correct answer would be the temperature as it was the only variable that changed. It could then be reason that there must be a limit in temperature at which solid water can exist. This point in temperature becomes important to understanding the underlying physics of the two phases. In many materials finding similar temperature points are crucial toward discovering phases where new properties could exist. Finding such temperature points can be done by measuring the coefficient of thermal expansion.

This chapter will discuss how phase transitions are detected through the thermal expansion coefficient. The portion covers some thermodynamic definitions to clarify certain definitions used throughout the chapter. Next the thermodynamic quantities compressibility, specific heat and coefficient of thermal expansion are defined. Finally, a relationship between these three quantities are drawn leading how the thermal expansion coefficient is related to phase transitions.

2.1 Thermodynamics

Classical and Statistical Thermodynamics

The area of thermodynamics is very broad yet well defined in the sense that it can describe many different situations but follows just four laws. It does no justice to sum the essence of thermodynamics into a small section however this is not a thermodynamics textbook and will merely cover the information needed to proceed. The study of thermodynamics refers generally and somewhat ambiguously to the study of heat. It can be further broken down into two parts; classical and statistical thermodynamics. Classical thermodynamics is a phenomenological theory using macroscopic properties of bulk matter without explicitly considering the microscopic structure. Conversely, statistical thermodynamics considers the microscopic structure of the system that give rise to its macroscopic behaviour. This is important as bulk matter is truly comprised of many particles resulting in a large number of degrees of freedom ($> 10^{23}$). The bridge between the two thermodynamic worlds is achieved by considering the statistical average of the particle properties and distribution. That is to say the macroscopic properties of a system are governed by the configurations of the particles which constitute it. However, the discussion of general thermodynamics need not consider the specific microscopic structure. This is the case in the following sections where the interaction between bulk properties do not need to emerge from a specific microscopic configuration.

The following sections follow several thermodynamic textbooks. For further reading, please refer to Reichl[1], Stanley[2], Allis[3] and Carter[4].

States, State Variables and Response Function

The (system) state is said to be the configuration (of the system) governed by macroscopic properties. If the state is independent of time, it is in equilibrium and its macroscopic properties are referred to as state variable. It is then possible to relate an equilibrium state to any other provided it obeys the same equation of state; a formula describing the state and involves state variables. An example of this outcome is the well known ideal gas law relating the state variables of pressure, temperature and volume. Needless to say, to understand the state of a material requires further investigation into state variable.

A state variables can be either intensive or extensive. If a state variable is intensive, it does not change in value if the system increases in space and degrees of freedom while on the other hand, an extensive state variable does. Examples of extensive variables would be volume V, particle number N and entropy S while examples of intensive variables would be pressure P, temperature T and chemical potential μ. It is important to recognize the designation as more complicated state variables are often comprised of several state variables. Of the state variables mentioned, temperature and entropy are unique as they relate to the thermal configuration of the system while the rest to the mechanical configuration.

A set of state variables known as response functions express the result of changing one state variable to another. Experimentally, these state variables are ideal to measure as it is the quantifiable response in one state variable normalized to a quantified change in another. Examples of response functions of a system are heat capacity C, coefficient of thermal expansion α and isothermal compressibility β. It is through these response functions that make the detection of phase transitions possible. Before supporting this claim, these response functions are first defined.

2.2 Compressibility, Specific Heat and Coefficient of Thermal Expansion

Compressibility and Bulk Modulus of Elasticity

Compressibility is the volume response of a system to an altering of pressure. This can be done in two ways; isothermally (constant T) or adiabatically (constant S). Physically one would liken isothermal compression to a compression on a closed (constant particle number N) system so slow that the temperature of the system is always in equilibrium with the surrounding environment while an adiabatic compression is so fast that the heat of the system remains the same or in perhaps a more physical notion the temperature of the system increases. The isothermal and adiabatic compressibility are respectively:

$$\beta_T = -\frac{1}{V_0}\left(\frac{\partial V}{\partial P}\right)_T \tag{2.1}$$

$$\beta_S = -\frac{1}{V_0}\left(\frac{\partial V}{\partial P}\right)_S \tag{2.2}$$

Alternatively, the inverse of the compressibility of a system is called the bulk modulus B is the pressure response due to a change in volume. The adiabatic bulk modulus would then be the inverse of the adiabatic compressibility (2.3). While the bulk modulus along the isothermal isopleth is not shown, it can be easily inferred from the isothermal compressibility.

$$B_S = \frac{1}{\beta_S} = -V_0\left(\frac{\partial P}{\partial V}\right)_S \tag{2.3}$$

Specific Heat

Specific heat describes the amount of heat energy necessary for a temperature change. It is the measure of how much heat energy is required to increase the temperature of the system per degree Kelvin. The heat change in terms of thermodynamic state variables is given as $dQ = TdS$. In a similar manner to compressibility, the specific heat can occur along two different isopleths; constant pressure or constant volume. In the case of constant pressure, this would be likened to changing temperature so slowly that the system's pressure remains constant with the surrounding environment. For constant volume, this would be an abrupt change in temperature so quick the volume does not change or alternatively the pressure increases. The isobaric and isochoric specific heat respectively are:

$$C_P = \left(\frac{\partial Q}{\partial T}\right)_P = T\left(\frac{\partial S}{\partial T}\right)_P \tag{2.4}$$

$$C_V = \left(\frac{\partial Q}{\partial T}\right)_V = T\left(\frac{\partial S}{\partial T}\right)_V \tag{2.5}$$

From an experimental perspective, it is typically much easier to establish constant pressure over constant volume as the restriction of volume with changing temperature becomes difficult due to the thermal expansion coefficient; a volume change due to temperature change.

Coefficient of Thermal Expansion

The coefficient of thermal expansion (or thermal expansion coefficient) is the measure of volume change due to a change in temperature. Unlike the response functions above where one could visualize the situation to be purely mechanical or thermal, the thermal expansion coefficient describes a mechanical response to a thermal fluctuation. This however is not so bizarre and in some sense can be more physically intuitive than specific heat. Naturally to observe the volume response, the pressure must remain constant. The coefficient of thermal expansion is defined as:

$$\alpha_P = \frac{1}{V_0}\left(\frac{\partial V}{\partial T}\right)_P \tag{2.6}$$

Before proceeding, a quick side note regarding an alternate format of the coefficient of thermal expansion; the thermal expansion. Certain groups prefer to publish publish results using the thermal expansion instead of the coefficient. The thermal expansion (2.7) is related to and from the thermal expansion coefficient by differentiation or integration respectively.

$$\frac{V - V_0}{V_0} = \frac{\Delta V}{V_0} \tag{2.7}$$

$$\alpha = \frac{\partial(\frac{V-V_0}{V_0})_P}{\partial T} \tag{2.8}$$

$$= \frac{1}{V_0}\left(\frac{\partial(V - V_0)}{\partial T}\right)_P \tag{2.9}$$

$$= \frac{1}{V_0}\left(\frac{\partial V}{\partial T}\right)_P \tag{2.10}$$

$$\int \alpha dT = \int \frac{1}{V_0}\left(\frac{\partial V}{\partial T}\right)_P dT \tag{2.11}$$

$$= \left(\frac{V + C}{V_0}\right)_P \qquad C \equiv -V_0 \tag{2.12}$$

These response functions will play a critical role in the next section. The compressibility was introduced first as its concept can be discussed through mechanical work of a piston system. In the event of specific heat, this becomes slightly more difficult to describe. However, one can develop an analog between mechanical work to thermal work (heat) done on the system. The thermal expansion coefficient describes a change in volume due to temperature change which from an intuitive standpoint can often be more readily realizable than compressibility or specific heat. With these response functions adequately defined, the next step is to relate phase transitions to the thermal expansion coefficient.

2.3 Phases and Phase Transitions

The phase of a system is the set of states (and by extension state variables) which are valid for a specific equation of state. Phases are identified from another if there is a distinct difference in properties. Recalling the scenario at the beginning of the chapter, the density could be used to distinguish the two phases. Phase diagrams are created by mapping phases with governing state variables as axes. Each phase is separated by a phase boundary; the set of points where both phases coexist. A phase transition occurs when one such phase boundary is crossed where the system enter one phase by leaving another. A generic P-T phase diagram for a simple substance is seen in Fig. 2.1. This next section will show how phase transitions can be observed through response functions.

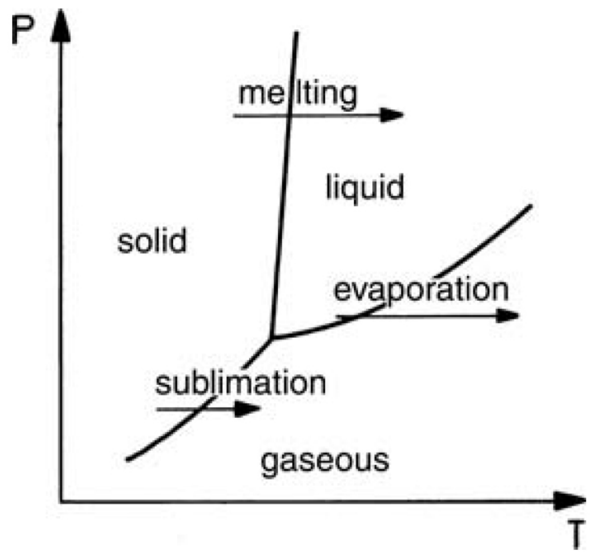

Figure 2.1: Generic P-T phase diagram of a simple substance from Schwabl [5]. A phase boundary separates the phases from one another. Crossing a phase boundary results in a phase transition.

The Thermodynamic Potential

The thermodynamic potential must first be defined and it will serve to relate the response functions to one another. The thermodynamic potential can be thought of as the available energy in a thermodynamic system which in many ways is analogous to the potential energy in a conserved mechanical system. In a similar fashion to the potential energy, the thermodynamic potential is comprised of several contributing terms. The thermodynamic potentials to be discussed are the internal energy, the Helmholtz function and the Gibbs function respectively given as:

$$U = TS + PV + \sum_i \mu_i N_i \tag{2.13}$$

$$A = U - TS \tag{2.14}$$

$$G = U - TS + PV \tag{2.15}$$

To proceed, each one is considered in differential form removing any unchanging contributions. The first to be considered is the internal energy. Systems studied in this thesis have conserved particle quantity thus the change in particle number dN is zero. The change in internal energy can be said to be the heat gain on the system dQ and work done by the system dW. These two terms can be though of thermal and mechanical pistons respectively.

$$dU = dQ - dW = TdS - PdV \tag{2.16}$$

Applying this to the Gibbs (2.15) and Helmholtz (2.14) thermodynamic potential functions, in their respective differential form yields the following results.

$$dA = -SdT - PdV \tag{2.17}$$

$$dG = -SdT + VdP \tag{2.18}$$

Two factors drive the change in the thermodynamic potential; a thermal fluctuation dT and a mechanical one (dV for Helmholtz and dP for Gibbs). For internal energy, entropy change dS acts as the thermal fluctuation and volume dV as the mechanical one.

The Helmholtz function describes a situation where temperature and volume are the independent state variables that can be adjusted while pressure and entropy respond to the change. Likewise the Gibbs function describes a situation where the temperature and pressure are adjustable while the volume and entropy respond.

Ultimately, regardless of whether a system is confined by temperature and pressure or temperature and volume, the thermodynamic potential is the available (free) energy of the system. Ergo, the quantity of free energy along any state variable isopleth cannot be discontinuous ensuring that there is no spontaneous gain or release of energy from varying state variables. This implies that the thermodynamic potential at the phase boundary must be continuous; a crucial consequence used later. The next step is to link the thermodynamic potential to response functions.

Gibbs and Response Functions

The first step is to relate the Gibbs function to response functions. The equivalent derivation for Helmholtz functions can be made by following this section so will not be shown. First consider the differential form of the Gibbs function (2.18) and how entropy and volume are related to it:

$$dG = -SdT + VdP = \left(\frac{\partial G}{\partial T}\right)_P dT + \left(\frac{\partial G}{\partial P}\right)_T dP \tag{2.19}$$

$$S = -\left(\frac{\partial G}{\partial T}\right)_P \qquad\qquad V = \left(\frac{\partial G}{\partial P}\right)_T \tag{2.20}$$

Experimentally, neither the volume or especially the entropy can be measured in this way as the Gibbs function itself is not directly measurable. Instead, the specific heat (2.4) and compressibility (2.1) are related to the Gibbs function:

$$C_P = T\left(\frac{\partial S}{\partial T}\right)_P = -T\left(\frac{\partial^2 G}{\partial T^2}\right)_P \tag{2.21}$$

$$\beta_T = -\frac{1}{V_0}\left(\frac{\partial V}{\partial P}\right)_T = -\frac{1}{V_0}\left(\frac{\partial^2 G}{\partial P^2}\right)_T \tag{2.22}$$

Since the Gibbs function cannot be discontinuous along any isopleth, the second derivatives specific heat and compressibility must exist. Although this doesn't have any direct implication to the end result, it establishes that these variables exist and are measurable in real materials. However, it isn't exactly clear how this works towards detecting phase transitions.

Consider a system with two temperature dependent phases. Suppose the equation of state of either phase to be quite distinct from one another; they are not explicitly known but do exist. The Gibbs functions on either phase are then unique and connect continuously at the phase boundary as necessary. If one were to graph the progression of the Gibbs function with temperature (Fig. 2.2a) while holding other independent state variables constant, a distinct alter curve profile exists at the phase boundary. A corresponding plot of entropy to this situation (Fig. 2.2c) would show a gap related to this phase change. By extension the specific heat which is proportional to the temperature derivative of entropy would show a divergence approaching the phase boundary. Based on this situation, a phase transition is observed as a divergence in specific heat. Conversely, if a divergence in specific heat is observed, it should be indicative of a phase transition. This is indeed true where the Gibbs function could alter very subtly across a phase transition (Fig. 2.2b). These transitions are called first order and higher order transitions based on what order the discontinuity occurs. If the thermal expansion coefficient can be expressed as a function of the specific heat, measuring the thermal expansion coefficient should similarly reveal phase transitions.

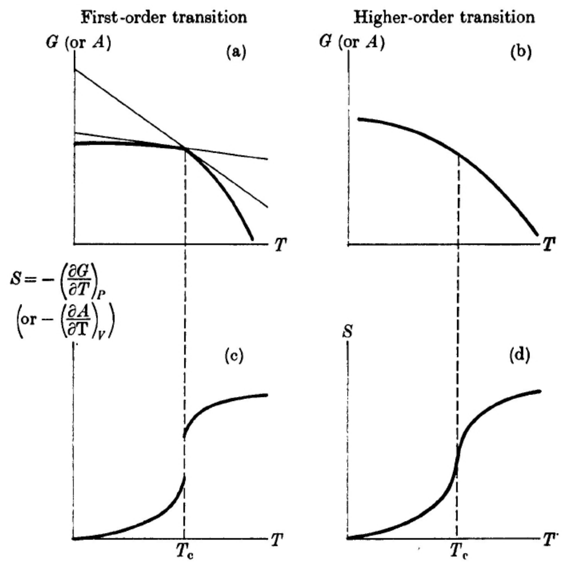

Figure 2.2: Schematic of first order and higher order phase transitions from Stanley [2]. In both cases the specific heat (not shown) shows a divergence linked to a phase transition.

Consider how the thermal expansion coefficient fits into the situation. Recall that the thermal expansion coefficient deals with the volume response to a temperature change under fixed pressure. The fact that pressure and temperature are constrained mean that it has the same requirements as the Gibbs function and should be related. This is indeed the case and using Maxwell's relation, the thermal expansion coefficient (2.6) related to the Gibbs function is:

$$\alpha = \frac{1}{V_0}\left(\frac{\partial^2 G}{\partial T \partial P}\right) \tag{2.23}$$

The thermal expansion coefficient can then be alternatively expressed using (2.20):

$$\alpha = -\frac{1}{V_0}\left(\frac{\partial S}{\partial P}\right)_T \tag{2.24}$$

Intuitively, this consequence is difficult to comprehend and after much deliberation, it is not clear as to how one can describe this physically. Therefore, the mathematical truth of this will have to suffice. The next step invokes an identity commonly used in thermodynamics whose full proof can be found in Reichl [1]. A function of three variables but only two independent have a canonical relation between the three variables which in this situation is (explicitly) the following:

$$-\left(\frac{\partial S}{\partial P}\right)_T = \left(\frac{\partial S}{\partial T}\right)_P \left(\frac{\partial T}{\partial P}\right)_S \tag{2.25}$$

The thermal expansion coefficient becomes:

$$\alpha = \frac{1}{V_0}\left(\frac{\partial S}{\partial T}\right)_P \left(\frac{\partial T}{\partial P}\right)_S \tag{2.26}$$

Recalling the specific (2.4), the coefficient of thermal expansion related to the specific heat is:

$$\alpha = C_P \frac{1}{TV_0}\left(\frac{\partial T}{\partial P}\right)_S \tag{2.27}$$

Further rearrangement and expansion of the derivative leads to:

$$\alpha = C_P \frac{1}{TV_0}\left(\frac{\partial T}{\partial V}\right)_S \left(\frac{\partial V}{\partial P}\right)_S \tag{2.28}$$

Noting that the second derivative is the compressibility (2.1), one further obtains:

$$\alpha = -C_P \beta_S \frac{1}{T}\left(\frac{\partial T}{\partial V}\right)_S \tag{2.29}$$

Lastly, the following relationship is drawn:

$$\frac{\alpha V B_S}{C_P} = -\frac{V}{T}\left(\frac{\partial T}{\partial V}\right)_S = \gamma \tag{2.30}$$

The thermal expansion coefficient is related to the specific heat C_P (2.4) and bulk modulus B_S (2.3) through the Grüeisen parameter γ. To first order, the Grüneisen parameter is weakly temperature dependent[6] which along with the bulk modulus which is completely temperature independent lead to a proportionality between the specific heat and thermal expansion coefficient with respect to temperature. Proof of this outcome can be seen with $LiHoF_4$; one of the materials studied in this thesis. Results of specific heat and coefficient of thermal expansion at the critical temperature (Fig. 2.3) when normalized show good agreement with one another. As such, there exists a temperature independent scaling factor between the two as predicted in theory.

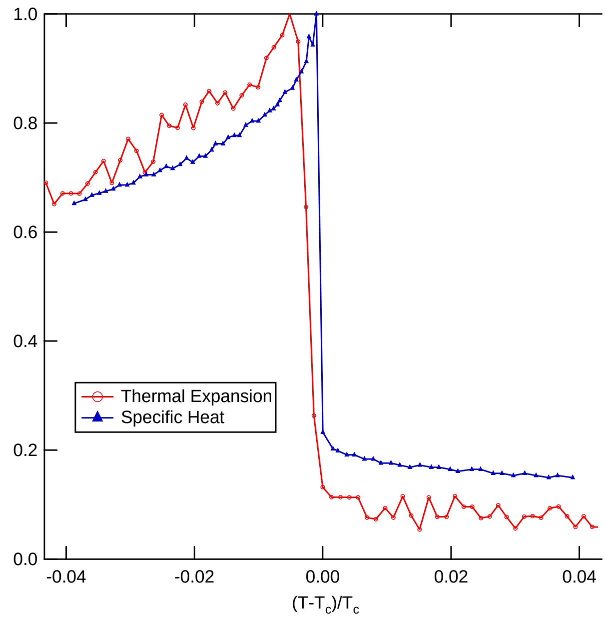

Figure 2.3: Normalized plot of thermal expansion and specific heat from Dunn's MSc thesis [7]. The phase transition is seen in both sets of data and since both are normalized, it is evident that there is a temperature independent scaling factor that relates thermal expansion to specific heat

The Grüneisen parameter is relatively constant over a wide, high temperature range [6]. However, the parameter at low temperatures may vary due to dominating terms such as phonon or electronic contributions. In each contribution, there is a corresponding Grüneisen parameter which relates a specific heat term to a corresponding thermal expansion coefficient term. Alternatively, a parameter total can then be defined which is the weighted average based on the respective heat capacities.

$$\gamma = \frac{\sum_i \gamma_i C_r}{\sum_i C_r} \tag{2.31}$$

Ultimately the Grüneisen parameter relates the thermal expansion coefficient to the specific heat. Since the bulk modulus and Grüneisen parameter (to first order) are independent of temperature, phase transitions through specific heat should be likewise observed in the thermal expansion coefficient.

Chapter 3

Capacitive Dilatometry

In the previous chapter, the thermal expansion coefficient is linked to the specific heat through the Grüneisen parameter. This justified the ability to observe phase transitions through the thermal expansion coefficient. In this chapter, the process of measuring the thermal expansion coefficient is discussed and three capacitive dilatometry devices are presented.

3.1 Introduction

Dilatometry is the measurement of dilation (expansion/contraction) of the volume of a material. The dilation or changes in volume of a material can be attributed to changes in state variables such as temperature and external magnetic field. There are several ways to measure the dilation of a material however each approach has its own benefits and drawbacks. Several methods of measuring dilation are outlined in Yates [8].

Capacitive dilatometry was chosen over the other methods for its very high sensitivity and simple yet effective approach to measuring dilation. Compared to other types such as interferometer dilatometry, minimal equipment is necessary making experiment implementation. By extension, measurement execution and data analysis become relatively straightforward. The benefit of measuring dilation through capacitance is that it can be related to a physical length change using the parallel plate capacitance equation and can be measured by a capacitance bridge. Capacitance bridges are commercially available which are capable of measuring capacitance to a high accuracy. The capacitance bridge used for measurements in this thesis has a resolution of $10^{-}7pF$ which for capacitor plate areas equal to the ones used equates to a dilation of approximately 0.002Å at $17pF$.

With thermodynamic measurement devices, particularly low temperature experiments, a key aspect is the ability to retain thermal equilibrium. This means that heating during measurement and operation of the device is an important factor. With capacitive dilatometry, there is negligible heating as there is negligible current produced with this method of measurement. In the end, capacitive dilatometry is an elegant straightforward method of measuring dilation all the while being relatively inexpensive.

Here, the method of determining the thermal expansion coefficient of a sample material through capacitive dilatometry is discussed. The general concept is established using a model capacitive dilatometer (Fig. 3.1). Once established, the thermal expansion coefficient of the sample is calculated.

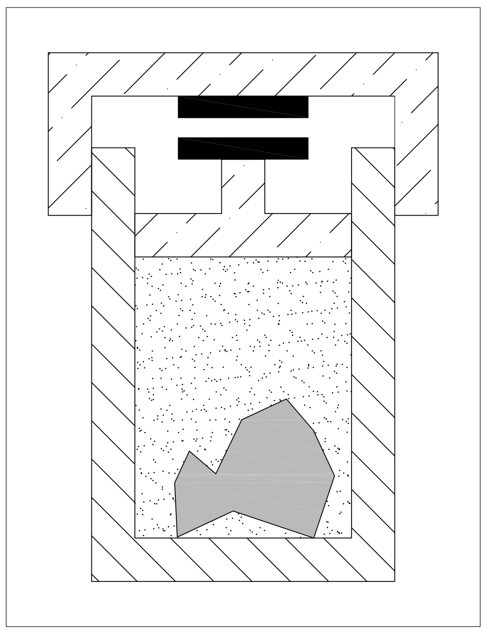

Figure 3.1: Sketch of a model capacitive dilatometer. As the material (grey) and liquid/gas (dots) thermally dilate, the piston moves a capacitor plates (black) towards or away from the other.

A material sample to be studied with unknown thermal expansion coefficient is encapsulated in a vessel with a piston wall. Along with the material, the vessel contains a liquid or gas with known thermal expansion coefficient; one that is relatively uniform and small over the temperature range of interest. On the end of the piston is an electrically conductive plate that is electrically isolated from the rest of the device. This moving plate is situated close to an identical electrically isolated plate. The second plate is attached to an fixed surface forming a parallel plate capacitor. The parallel plate capacitor equation (3.1) relates capacitance C inversely to plate separation D through the permittivity of free space ϵ_0 and capacitor plate area A.

$$C = \frac{\epsilon_0 A}{D} \propto \frac{1}{V} \tag{3.1}$$

The combined volume of the material and liquid/gas governs the position of the moving plate and hence plate separation. The volume is proportional to the plate separation given the vessel's constant cross section. Therefore, capacitance indicates the volume of the vessel. The thermal expansion coefficient is computed by differentiating the measured volume with respect to temperature using finite central differences method.

However, the thermal expansion coefficient measured is not only from the sample but also includes any other factors affecting the volume. These factors are typically referred to as the cell effect and can be defined as the contribution to the measured thermal expansion coefficient by the cell (device). The cell effect varies based on the design and materials of the dilatometer and becomes increasingly difficult to rationalize with complexity of design and use of different materials.

An expression for the thermal expansion coefficient of the sample from the measured thermal expansion coefficient is derived. The measured volume can be separated into sample and cell:

$$V_{measured} = V_{sample} + V_{cell} \tag{3.2}$$

Taking the temperature derivative, dividing by the original sample volume, rearranging and recalling the definition of the thermal expansion coefficient (2.6) gives the following:

$$\alpha_{sample} = \frac{1}{V_{0,sample}} \frac{dV_{measured}}{dT} - \frac{1}{V_{0,sample}} \frac{dV_{cell}}{dT} \tag{3.3}$$

The second term is the correction or cell effect term which must be characterized to obtain quantitative values of the thermal expansion coefficient. For ever dilatometer, the cell effect can be determined both theoretically and experimentally. The theoretical cell effect term is calculated by considering as many factors that impact the volume. The most direct contributor in this model would be the liquid/gas. Assuming this is the only contributor, the cell effect term becomes (3.4). The preference of a small thermal expansion coefficient liquid/gas stated earlier reduces the magnitude of the contribution of this term. Additionally, it is seen that using less liquid/gas would reduce this term further.

$$\frac{1}{V_{0,sample}}\frac{dV_{cell}}{dT} = \frac{V_{0,liquid/gas}}{V_{0,sample}}\alpha_{liquid/gas} \tag{3.4}$$

However, this cell effect term fails to consider the impact of the thermal expansion of the vessel itself. Considering this makes the calculation of the cell effect term much more complicated as it would affect the volume by altering the vessel's cross section. It is clear that the more complicated the device, the more difficult it becomes to theoretically calculate the cell effect term.

While the theoretical calculation should give a good estimate of the cell effect, it does not necessarily reflect the actual cell effect. Therefore, the cell effect contribution is determined experimentally. This involves measuring the thermal expansion coefficient of a known material. The difference between the measured thermal expansion and known values becomes the cell effect contribution.

$$\alpha_{sample,known} - \alpha_{measured} = \alpha_{cell,actual} \tag{3.5}$$

In practice, this model capacitive dilatometer is not feasible as it relies on several factors which are difficult if not impossible to implement. For example, finding a 'well behaved' liquid/gas would require the absence of a phase transition within the measuring temperature. Additionally, a hermetic encapsulation without compromising the piston's movement would be extremely difficult. Although it is not possible to employ this model, the logic behind the many aspects may be adopted for other designs.

The solution to the above dilemma is to measure the thermal expansion coefficient along a single direction. This is achieved by having the material in contact with the moving plate. This linear capacitive dilatometer requires that the geometry of the sample to be well defined such that the volume can be calculated. An inability to do so would mean the volumetric thermal expansion coefficient cannot be computed. However, many materials are moderately isotropic so detection of a phase transition along a single axis is still a possibility.

Without a buffer between sample and capacitor plate, the device would require an alternative restoring mechanism. This is achieved by a spring ensuring the moving capacitor plate remains in constant contact with the sample. The requirements for the spring are that it be mechanically robust and have a low spring constant. The spring must be able to reliably operate across a large range of low temperatures and withstand many thermal cycles. Furthermore, the spring motion must be restricted to ensure the capacitor plates remain as parallel as possible. Failure to do so would lead to a non-constant tilting of the capacitor plate. A low spring constant is important for materials with pressure dependency from either a thermodynamic or physical (i.e. brittle samples) perspective. Characterizing it provides an upper limit to the pressure that can be compensated for accordingly.

Three capacitive dilatometers are presented in this thesis; the silver compact dilatometer, the fused quartz dilatometer and a copper dilatomter.

3.2 Silver Compact Dilatometer

A considerable amount of research has already been invested into the development of this dilatometer. Details outlining assembly, testing and calibration of this device is found in Dunn's MSc thesis [7]. The general design was based a the dilatometer by Schmiedeshoff's *et al.* [9] with improvements on reducing components and simplifying the design. A cut-away diagram of the most recent version of the dilatometer is shown in Fig. 3.2.

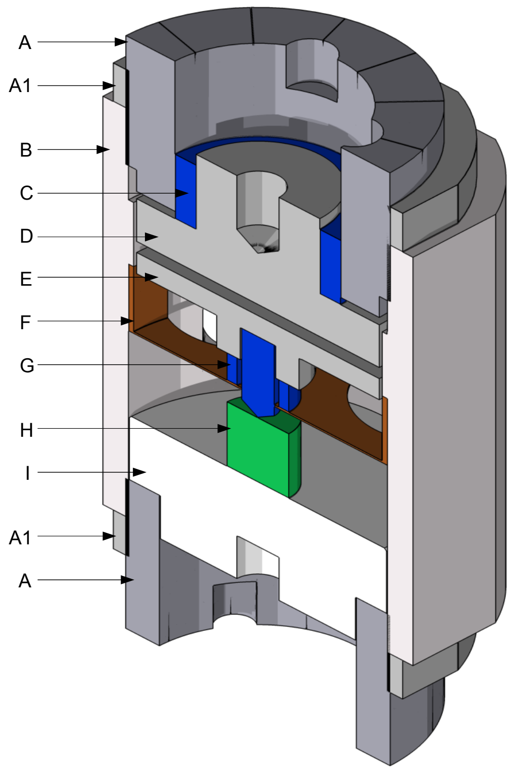

Figure 3.2: A diagram of the silver compact dilatometer. Two A304 stainless steel positioners at the top and bottom (A) thread into a silver shell (B). The positioners and the shell are threaded at 80 turns/inch, or 3.14 turns/mm. Positioners are held in place using A304 stainless steel nuts (A1). The fixed capacitor plate (D) is mounted inside the upper positioner and electrically isolated with a sapphire washer (C). The capacitance between the upper (D) and lower (E) capacitor plates is determined by the plate separation (and the plate area). The lower capacitor plate (E) is fixed to a beryllium-copper spring (F) using a sapphire pin and washer (G). The sample (H) is mounted to a sample base (I), and the lower positioner (A) is used to adjust the position of the sample base (I), and consequently press the sample (H) against the BeCu spring (F). When assembled, the dilatometer is between 23 mm and 27 mm long depending on the length of the sample. The outer cross-section of the shell is a 15 mm square, an inner circular bore contains the other components shown. All inner components are circular and concentric with the inner bore of the shell. The area of the circular capacitor plates is approximately 108 mm^2.

The dilatometer design is quite versatile as it is possible receive material samples measuring up to 5 mm by 5 mm in cross section and potentially 10 mm in length. Furthermore, the fixed capacitor plate (D) can be adjusted to increase or decrease the starting separation of the plates to compensate for the thermal expansion of the device and sample. This means that once initial measurement of the thermal expansion coefficient is performed, following experiments on the material can be measured at optimal resolution. The resolution increases at smaller plate separation seen by the separation derivative of the parallel plate capacitor equation.

$$\left.\frac{dC}{dD}\right|_{D_0} = -\frac{\epsilon_0 A}{{D_0}^2} \tag{3.6}$$

$$dC = -\frac{\epsilon_0 A}{{D_0}^2} dD \tag{3.7}$$

With a smaller initial plate separation, a larger change in capacitance is measured for a change in plate separation. With a large capacitance change, fluctuations from background noise are lowered relative to the growth of the material. For example an initial plate separation of 100 μm, a change in plate separation of 0.01Å would be under 10^-7pF; below the resolution of the capacitance bridge. Halving the initial plate separation, the same change in plate separation becomes four times as large.

Despite the versatility in this design, several drawbacks have limited an ability to make measurements on samples with small features or ones requiring quantitative results. The primary culprit behind this limitation is due to the cell effect of the silver dilatometer. The cell effect measured in Dunn's MSc thesis for the silver dilatometer is presented in Fig. 3.3. For the design involving sapphire, the cell effect becomes larger than 10^{-6} above $T \approx 25$ K. Based on the cell effect, the contribution to the measured thermal expansion coefficient becomes non negligible at higher temperatures making analysis of features on the same order of magnitude as the cell effect an issue. However, below 10 K, the cell effect is near negligible making this device ideal for measurements below 10 K.

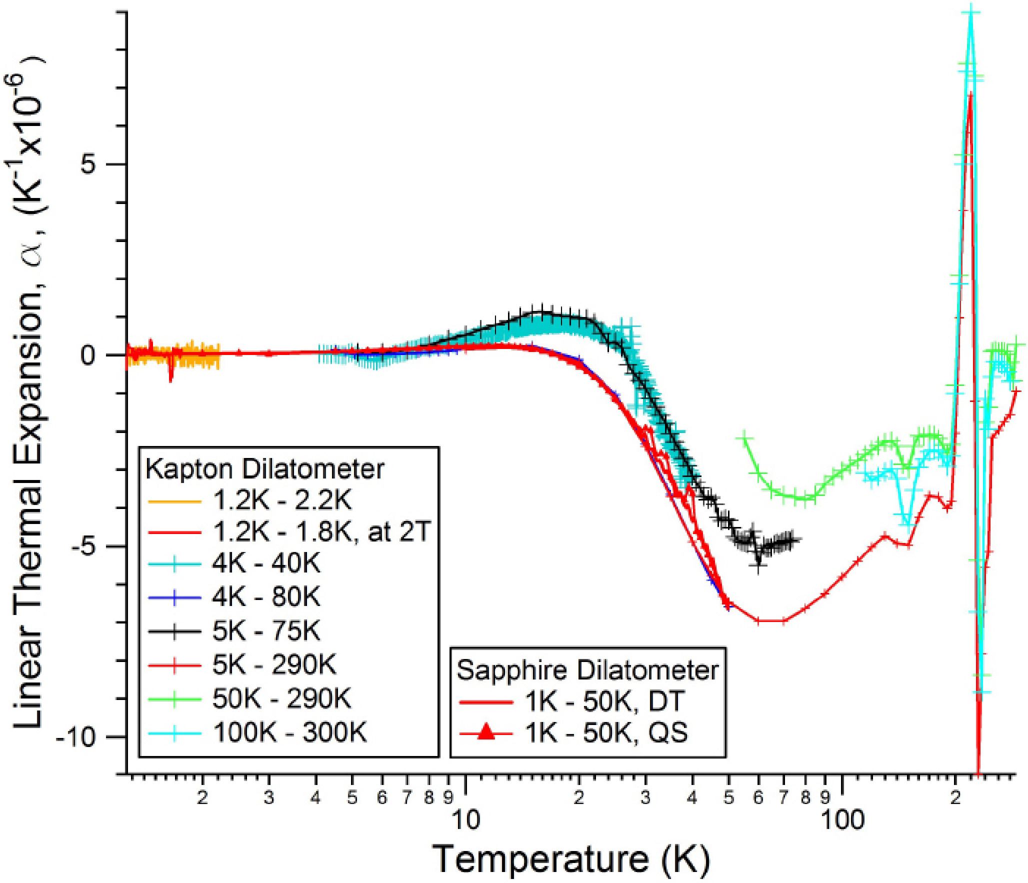

Figure 3.3: The cell effect for the silver dilatometer from Dunn's MSc thesis [7]. The cell effect was measured for the design consisting of sapphire and an older version using Kapton. The large spike in the cell effect at 200K is belived to be from the freezing of epoxies used in the design.

Further investigation into the cell effect at higher temperatures was performed to determine factors which could alter the cell effect. Knowledge of the contributing factors could lead to further minimization of the cell effect. A joint study with J. Akeyr explored several factors that were believed to affect the cell effect of the silver dilatometer.

The several possible factors that were though to have caused lack of reproducibility; the amount of torque used during preparation, initial spring deflection and different mounting agents. The thermal expansion coefficient of $Ba_3NbFe_3Si_2O_{14}$ (Chapter 6) along the a-axis was measured down to liquid nitrogen temperatures. It was found that neither varying torque nor spring deflection did not affect the results appreciably. Different mounting agents such as GE varnish and silver epoxy were found to slightly alter the profile but not the overall magnitude. Since then, mounting agents have been removed from preparation altogether when possible. An issue with the overall value of the thermal expansion coefficient still persists; the origin of which has yet to be identified.

This device is not obsolete by any means and is ideally operated at temperatures below 10 K and magnetic fields up to 14 T. The use of silver in the design permits experiments involving magnetic fields due to the considerably lower nuclear heat capacity as observed in Fig. 10.4 in Pobell [10].

Materials with thermal expansion coefficient features greater than 10^{-6} can be observed. This device is known to function as the results of $LiHoF_4$ (Chapter 4) are measured using this dilatometer. Due to the complex cell effect, the general magnitude of the thermal expansion coefficient does not provide much usable information.

3.3 Fused Quartz Dilatometer

This section of the thesis presents the development of a new dilatometer. The general concept behind the design and benefits over the silver design are discussed. A detailed guide of the assembly of the device and mounting base are presented. Effects of plate tilt and electrical grounding are separately discussed. Lastly, the quartz dilatometer is tested for the spring constant, thermal time constant and cell effect completing process of creating of a dilatometer.

3.3.1 Introduction

Despite the versatility of the silver compact dilatometer, the limitation to make accurate quantified thermal expansion measurements is an issue. This is the case when results are compared to published work related to the thermal expansion coefficient. The cause of this limitation was attributed to the use of many different materials. The solution was to create a dilatometer with the least number of different materials. Ideally, a material with a small, uniform thermal expansion coefficient should be used. Fused quartz was selected over other potential materials in consequence of work by Neumeier *et al.* [11]. The paper describes the creation, calibration and testing of a fused quartz dilatometer which this design is based upon. A cut-away diagram and photograph of the fused quartz dilatometer is shown in Fig. 3.4. The quartz design operates slightly different from the silver design.

Instead of a growing sample pushing the capacitor plates closer together, the quartz design pushes the plates further apart.

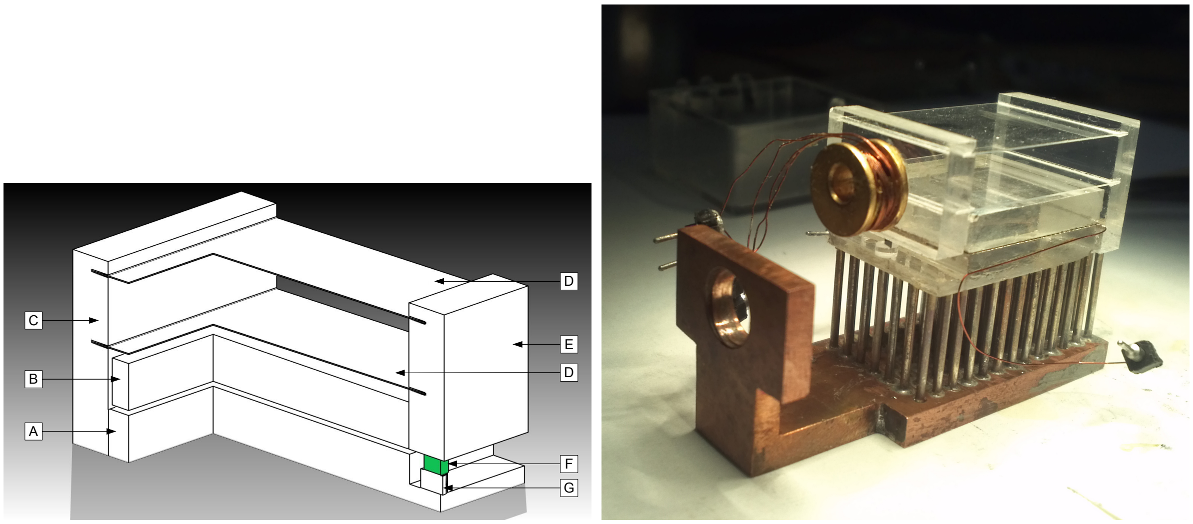

Figure 3.4: **Left:** A diagram of the fused quartz dilatometer. A capacitor is formed from facing sides of the bottom plate (A) and top plate (B) evaporated with silver. The plates are attached to the bottom (C) and top wall (E) respectively. Quartz springs (D) keep the two halves together while ensuring perpendicular movement to the faces. The sample (F) and quartz spacer (G) separate the capacitor plates and remain under small compression from quartz springs. When assembled, the dilatometer is 25 mm long and cross section of 15 mm square. The area of the rectangular capacitor plates is approximately 270 mm^2. **Right:**The assembled fused quartz dilatometer. The capacitor plate leads extend on opposite sides of the dilatometer to reduce contribution to the capacitance. A thermometer is mounted to the top plate for thermal time constant purposes. A sample can be seen atop a quartz spacer separating the two capacitor plates.

Fused quartz (silica) is amorphous silicon dioxide (SiO_2) and is readily purchasable in many shapes and sizes. Furthermore, it is an electrical insulator which is advantageous to electrically isolating the capacitor plates. Pieces of fused quartz can also be bonded to one another using sodium silicate (Na_2SiO_3); a commercially available adhesive for ceramics. The thermal expansion coefficient of fused quartz is much smaller and varies less compared to silver shown in Fig. 3.5. Particularly above 20 K where the thermal expansion coefficient of silver begins to increase considerably, fused quartz is an ideal material to use for capacitive dilatometers.

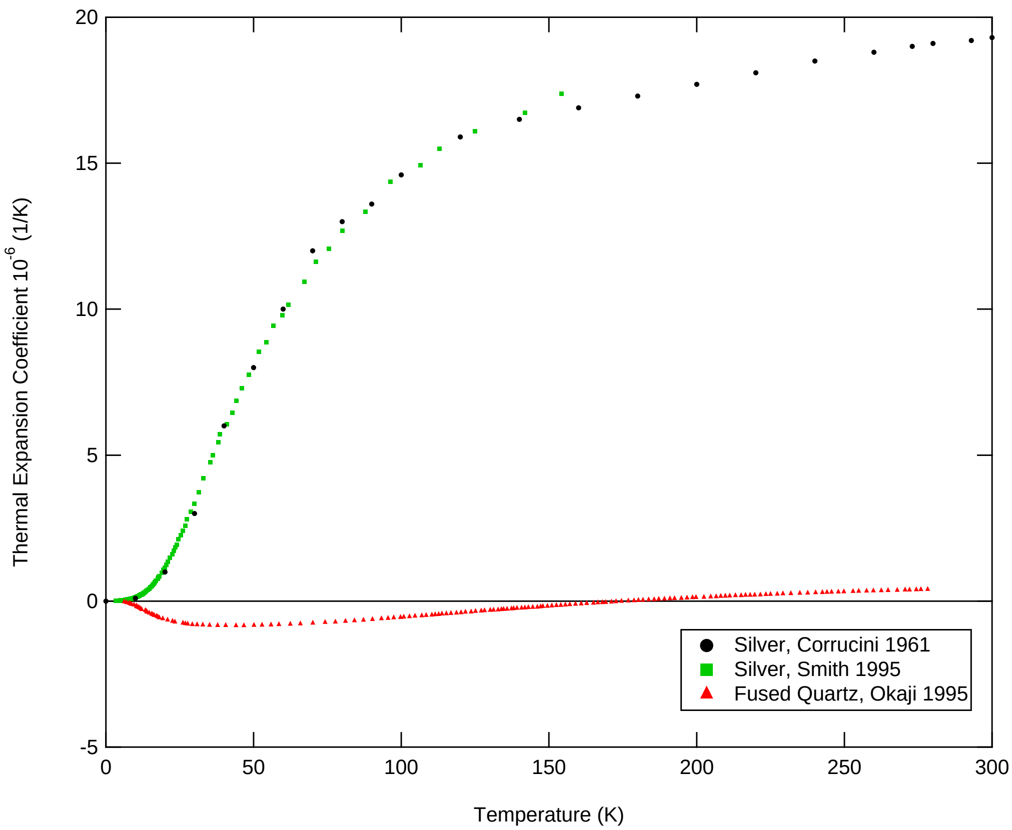

Figure 3.5: The coefficient of thermal expansion of silver and fused quartz as a function of temperature. The magnitude of the thermal expansion coefficient is a good first order estimate of the contribution to the measured thermal expansion coefficient. Values were taken from [12] for fused quartz and [13, 14] for silver.

The quartz design itself has two other notable improvements over the silver design; plate area and plate flatness. The plate faces in the silver design are restricted to a 15 mm square as they are parallel to this cross section. The 15 mm square constraint is to ensure the dilatometer fits into a rotating stage. In the quartz design, the plate faces are perpendicular to the cross section use longer length of the rotating stage. The quartz design has a plate area of approximately 270 mm^2; nearly three times the area of the silver design. Referring back to (3.7), a larger area further increases the resolution of measuring material growth. The added plate area permits measurement of materials with even smaller thermal expansion coefficients since the response is boosted further.

At increasingly small plate separation values, the flatness of the capacitance face becomes increasingly important. Small irregularities to the face would generate a non-uniform electric field impacting the capacitance. In the silver design, the plate faces are machined to the best tolerance and then polished by hand. The hand polishing, despite taking the utmost precautions will inevitably create irregularities to the face. Typically these irregularities are due to an uneven distribution of force while polishing. One could expect a variance of the face on the order of 10^{-5} m on the plate face. The quartz design evaporates silver onto lapped quartz to create capacitor plates. The silver distribution is virtually uniform creating very flat capacitor plates. One could expect a variance of the face on the order of 10^{-8} m on the plate face.

succinct

3.3.2 Assembly

The method of assembly is done in a manner to ensure the capacitor plate faces are as parallel to one another as possible. Several components are used throughout the assembly to aid in keeping components squared with one another. A portable, flat surface such as a mirror or granite scribing table is strongly suggested to be used to assemble all components. Orthogonal faced blocks are also needed to create vertical walls on which to align the components. The assembly described in this thesis uses '123' blocks which have faces that are orthogonal to one another to the degree necessary. Two '123' blocks are clamped together forming two perpendicular walls and placed atop the flat surface creating a square corner. Components can then be butted up against either wall and aligned in all directions during assembly.

The components are glued using sodium silicate (Na_2SiO_3); a standard compound used in gluing ceramics together. The solution can be purchased from a commercial chemical distributor and typically comes in a 40-60 mix of sodium silicate to distilled water. The initial mixture is quite viscous and is recommended that it be further diluted with distilled water. The ideal ratio was found to be approximately a 1-2 mix of sodium silicate to water. The glue is delivered to the necessary location using a high (thin) gauge bevel tip syringe needle. Careful application can be achieved by forming a drop of mixture on the end of the tip (with surface tension) and carefully touching it to the intended location. Since the locations which the glue should be administered are between two components, the glue should wick in by capillary action. The transparency of the quartz is allows for convenient monitoring of the flow of the mixture. Precaution is needed in the quantity administered as too much will form a brittle bulk layer prone to fracture during thermal cycles but too little prevents the components from adhering resulting in break down in several thermal cycles. While wet, the glue can be removed using distilled water but be sure to dry off all surfaces before reattempting to glue the components as the glue may flow to undesired wet locations.

The components are cut from a $\frac{1}{8}$" thick, 2" by 2" quartz piece following dimensions detailed in Appendix D. Once cut, a chamfer is put along the edge width of the top and bottom plate to eventually seat the electrical leads. The sides with the chamfers are then evaporated following the evaporation guides detailed in Appendix F. Masking tape is used to cover any portion of the components which should not have silver. The chamfer edge is not to be masked as they are necessary for the electrical leads. The thickness of the silver film evaporated onto each face is roughly 0.5 μm in thickness. If the film is too thin, voids are likely to be present while too thick, separation from the substrate is a possibility.

After the faces are evaporated, the plates are glued to the corresponding wall components. They are glued making 'L' shapes with the chamfer positioned along the wall component. The components should be oriented such that the evaporated faces are touching other when stacked.

After the glue on 'L' pieces has set, 100 μm copper wire leads are attached. This is done by carefully seating the wire deeply into the groove and carefully covering the wire with silver paint. It is recommended the wire be as straight as possible prior to seating such that no portion protrudes above the groove. Ensure that the wire leads leave opposite ends of the device to minimize contributions to the capacitance. To reduce strain on the painted portion, rest of the wire lead is glued along the sides of the plates using GE varnish.

The 'L' pieces are now connected to one another by the quartz springs. Carefully place position the pieces at their intended final location. The quartz springs as slid into the slots from the side. Carefully push the pieces together such that the springs are fully in the slots. While keeping everything lightly compressed, carefully glue the springs into the slots. Ensure that all components are correctly placed while the glue dries.

The assembled dilatometer is mounted on the holding base and any thermometers are attached. The prongs of the base are dipped in GE varnish and the dilatometer is placed on top with a weight to ensure good contact during curing. Thermometers can be attached nearly anywhere on the dilatometer using GE varnish. Typical the locations of a thermometer are next to the sample or furthest from the cooling source.

3.3.3 Mounting

Attempts to mount the quartz dilatometer proved to be more difficult than originally anticipated. At first, it was belived that the sodium silicate glue could attach the quartz dilatometer to a copper base allowing easy mounting to a cryostat. However, the substantial difference in thermal expansion coefficients between copper and quartz would destroy the adhesion. The solution was an adaptation of the beryllium copper comb used in SCUBA-2 measurements [15] for a similar circumstance.

The comb was a lattice of long thin beryllium copper tines able to flex accommodating the thermal expansion of the mounted object. Electrical discharge machining (EDM) was used to cut deep narrow channels from a block of raw material to form the high density lattice of tines. Unfortunately, EDM requires special machining facilities and can be an expensive option. Creating a low density comb using conventional machining techniques would seriously reduce the thermal conductivity to undesirable values. The compromising alternative to this dilemma is to create a comb unit using multiple components. This way, a relatively high density comb can be fabricated inexpensively.

The comb or holding base used in this thesis is made from copper wires inserted into holes on a copper base. The copper base whose design can be found in Appendix D forms a tine density based on the machined hole lattice. A square lattice of holes was made for simplicity but higher density combs may be created at a later time. The tines were made from AWG 20 ($\phi \approx 0.8$ mm) copper wires closely matching the dimensions of the tines of the SCUBA-2 comb. The tines must be thick enough to remain rigid yet narrow enough to remain flexible.

The holding base is assembled by straightening and inserting the copper wires into the holes of the copper base. The inserted wires should be slightly longer than the final length as the top will be trimmed later. The straightening is achieved by rolling wire segments between two flat surfaces. All the wires are simultaneously soldered into the holes by heating the entire base and flowing solder from the bottom. Excess solder from this process is then removed by sanding.

The tines are trimmed by machining to create flat top. Crystalbond, a temporary adhesive, is used to encase the tines preventing them from deflecting during this process. Crystalbond liquefies at sufficiently high temperatures, solidifies at room temperature and can be dissolved using acetone. A rigid metal sleeve is placed around the tines creating a volume to contain the Crystalbond. Once the Crystalbone set, the tops of the tines are flattened by milling. The copper base is reheating to remove the sleeve and liquefy excess Crystalbond. Residual Crystalbond is removed by acetone completing the assembly of the holding base. The completed base with quartz dilatometer mounted on top can be seen in Fig. 3.4 Left).

A major concern regarding the design of the current holding base is the use of lead based solder. Under 2 K, lead based solder becomes superconducting impeding thermal transport [10]. Future holding bases should use a low temperature adhesive such as silver epoxy to attach the tines to the copper base. Additionally, the copper wires used in the current holding base are pre-coated with solder. This coating should be removable by fine grit sandpaper.

3.3.4 Plate Tilt Effects

It is not realistic to assume the capacitor plates are parallel despite taking the utmost precautions to ensure that they are. Therefore, it is important to assess the impact a tilt has on the capacitance. For the silver design, a tilted circular plate capacitor equation (3.8) was derived (from [16]). The derivation was for circular plates with radius r and constant tilt a (Fig. 3.6). The C_{max} value can be experimentally determined and is the maximum capacitance measured right before the plates touch (and electrically short).

$$D = \frac{\epsilon_0 A}{C}\left[1 + \left(\frac{C}{C_{max}}\right)^2\right] \qquad C_{max} = \frac{2\epsilon_0 \pi r^2}{a} \tag{3.8}$$

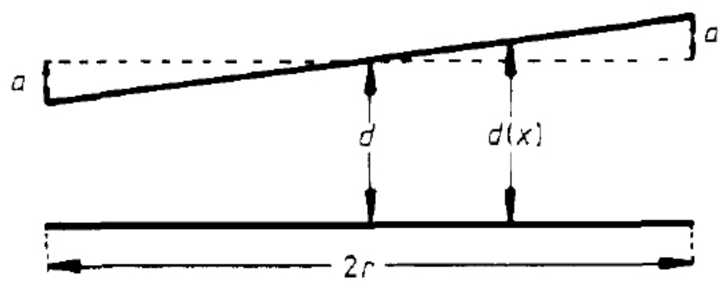

Figure 3.6: The configuration of the tilted plate used to derive the circular tilted plate equation from Pott *et al.* [16]. The tilt a creates a non-constant plate separation d along the x direction.

This equation cannot be used for the quartz dilatometer since the design uses rectangular plates. A tilted rectangular plate capacitor equation with constant tilt was derived using the same approach. This derivation also assumes the tilt is only along the length or width of the plate. The equation is derived by taking the capacitance element dC and integrating over the plate area. The plate separation varies along the length L due to the tilt a and is given by $D(x)$ where D is the central plate separation.

$$dC = \epsilon_0 \frac{dydx}{D(x)} \qquad\qquad D(x) = D + \frac{2ax}{L} \tag{3.9}$$

$$\begin{aligned} C &= \epsilon_0 \int_{-L/2}^{L/2} \int_{-W/2}^{W/2} \frac{dydx}{D + \frac{2ax}{L}} && (3.10) \\ &= W\epsilon_0 \frac{L}{2a} [\ln(1 + \frac{a}{D}) - \ln(1 - \frac{a}{D})] && (3.11) \end{aligned}$$

Conceptually, a must be less than D to obtain a capacitance value. Since $\frac{a}{D} < 1$, it is possible to power series expand.

$$C = W\epsilon_0 \frac{L}{2a} \left[\sum_{n=1}^{\infty} (-1)^{n+1} \frac{(a/D)^n}{n} - (-\sum_{n=1}^{\infty} \frac{(a/D)^n}{n}) \right] \tag{3.12}$$

The even terms in the series cancel each other while the odd terms add resulting in the following:

$$\begin{aligned} C &= LW\epsilon_0 \frac{1}{a} \sum_{n=1}^{\infty} \frac{(a/D)^{2n-1}}{2n-1} && (3.13) \\ &= LW\epsilon_0 \frac{1}{a} \sum_{n=0}^{\infty} \frac{(a/D)^{2n+1}}{2n+1} && (3.14) \end{aligned}$$

As it turns out, this is the power series expansion of $\tanh^{-1}(\frac{a}{D})$. Together with and the plate area $A = LW$ the equation becomes:

$$C = \frac{\epsilon_0 A}{a} \tanh^{-1}(\frac{a}{D}) \tag{3.15}$$

Or alternatively:

$$D = \frac{a}{\tanh(\frac{aC}{\epsilon_0 A})} \tag{3.16}$$

The parallel plate equation is recovered from this tilted rectangular plate equation for $\frac{a}{D} \to 0$. This is done by either having the plates separated much more than the tilt or a negligibly small tilt. Unfortunately, unlike the tilted circular plate equation (3.8), a corresponding C_{max} does not exist. To experimentally determine the tilt a, either it would have to be directly measured or the central separation be measured at different capacitance values. Instead, a reasonable upper limit is established with some additional analysis.

Consider the percent difference between the tilted plate equation (3.15) and parallel plate equation (3.1) as a function of plate separation (Fig. 3.7). Using a reasonable estimate of the tilt values in standard plate separation conditions, at the largest $\frac{a}{D} \approx 0.25$ the percent difference hardly exceeds 2%. Putting it into perspective, the uncertainty of measuring the sample length is estimated to be upward of 10%; an order of magnitude greater. To that end, the uncertainty of the length would be the leading cause of uncertainty over the plate tilt.

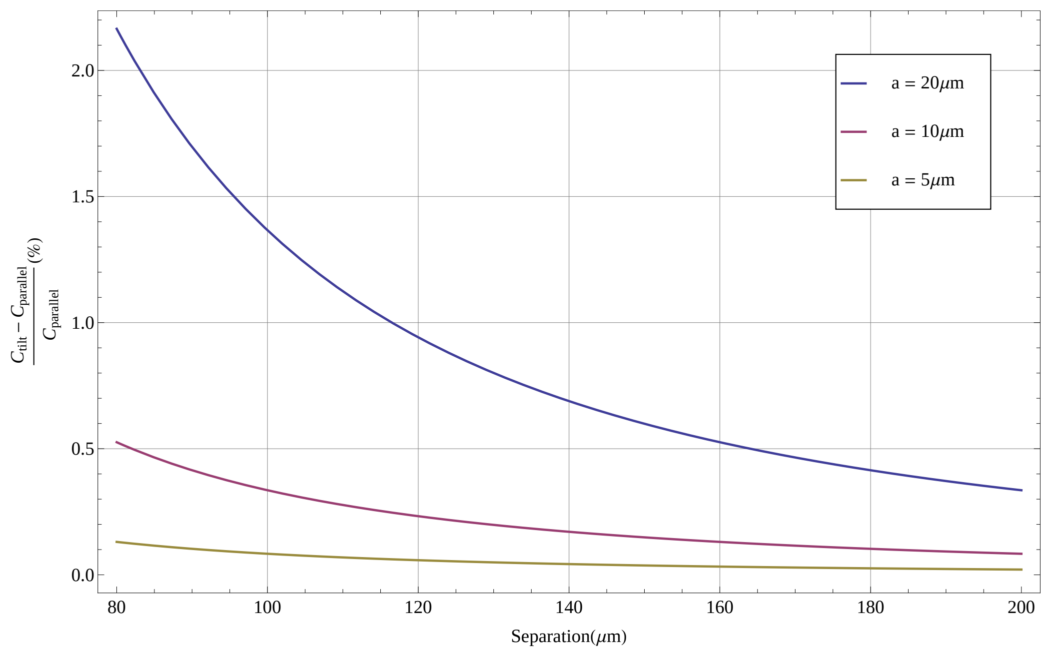

Figure 3.7: The percent difference of capacitance values at typical operating plate separation of several reasonable tilt values. Even at a large $\frac{a}{D} \approx 0.25$, the difference does not exceed 2%.

3.3.5 Fringe Effects and Shielding

A notable difference between this design and the design by Neumeier *et al.* [11] is the absence of grounding ring around the capacitor plates. In their design, a scribing tool was used on the evaporated film to create electrically isolated rings around the capacitor plates. These rings when grounded serve to reduce any edge (fringe) effects creating a more ideal parallel plate capacitor. The design presented in this thesis did not follow suit due to lack of proper tools to perform the scribing. Instead, an encapsulating grounding shield around the whole dilatometer is used. To ensure that the absence of grounding ring does not seriously affect the capacitance measurements, the edge effects are theoretically calculated. Fig. 3.8 shows the fringe field lines of a 1 dimensional capacitor without grounding rings.

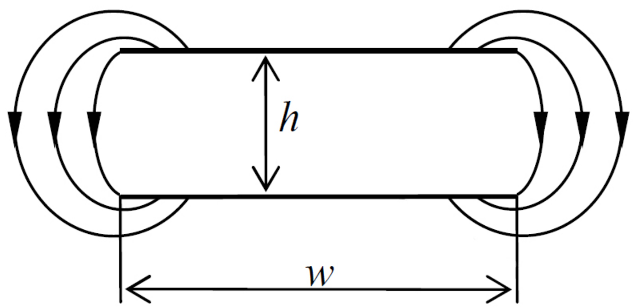

Figure 3.8: The fringe effect of a 1D capacitor with width w and plate separation h from Leus [17]. Without grounded guard rings, the non-constant electric fields generated from other regions of the plate contribute to the overall capacitance.

Several edge effect capacitance equations have been derived using different methods and approximations. Summarized in [17], equations for 1 dimensional (line) capacitors are discussed and compared. The history of edge effect calculations are quite colourful dating back to Clausius in 1852 [18]. For the purpose of this thesis, the equation by Elliott is used to draw the conclusions regarding edge effect contributions to the capacitance. The same conclusion can be reached using the other edge effect equations. Using the Schwarz-Christoffel conformal mapping approach, the capacitance per unit length as per Elliott is:

$$C = \epsilon_0 \frac{L}{D} \left[1 + \frac{D}{\pi L} \ln \left(\frac{\pi L}{D} \right) \right] \tag{3.17}$$

The first order 2 dimensional equation is obtained by assuming a separable solution to the second dimension resulting in the following:

$$C = \epsilon_0 \frac{LW}{D} \left[1 + \frac{D}{\pi L} \ln \left(\frac{\pi L}{D} \right) \right] \left[1 + \frac{D}{\pi W} \ln \left(\frac{\pi W}{D} \right) \right] \tag{3.18}$$

The length and width of the capacitor plates of the quartz capacitor are 18 mm and 15 mm and are much larger than the plate separation D. Plotting the percent difference from the ideal parallel plate capacitor equation (Fig. 3.9), edge effect does not exceed 5% in standard operating plate separation values. Adopting the same logic as the tilted plate section (3.3.4), the leading uncertainty remains to be the measurement of the sample length.

Based on these results, the absence of a grounding ring does not appear to substantially impact the capacitance. This cannot be said for stray electric fields from external sources and can anomalously contribute to the capacitance. A copper vessel whose design can be found in Appendix D is grounded shielding the capacitor from external sources.

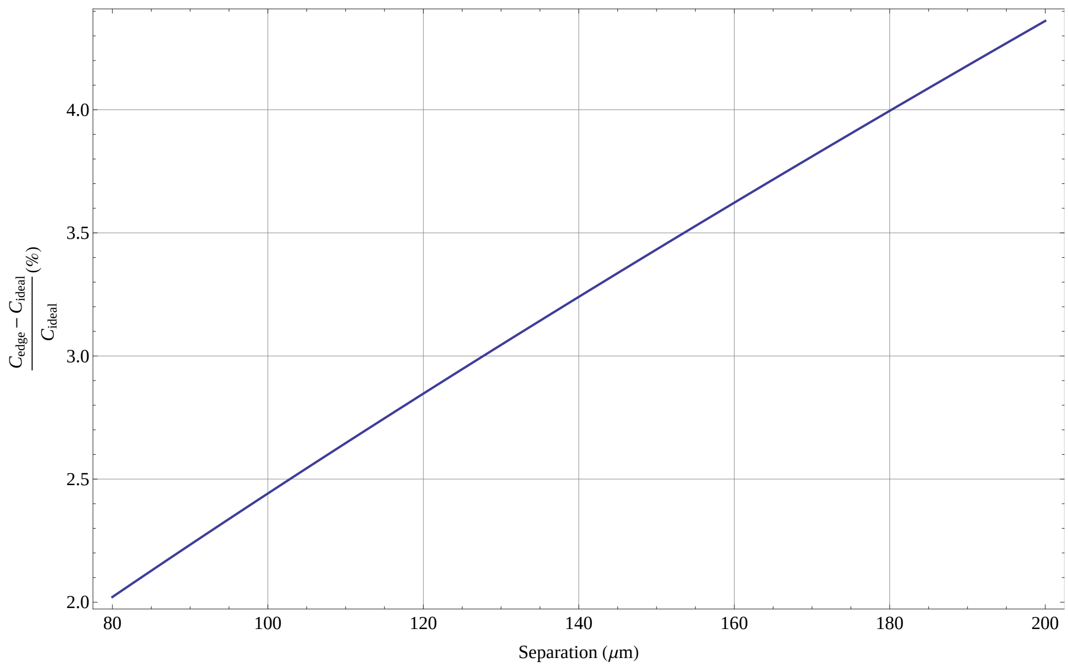

Figure 3.9: The edge effect on capacitance across typical plate separation ranges do not largely impact the result showing less than 6% deviation at a separation of 200 μm

3.3.6 Testing and Calibration

Several aspects of the quartz dilatometer should be characterized before using it to measure materials. The spring constant must be measured to know the amount of pressure the sample will be under. Thermal time constants are also calculated to estimate the time needed for the device to reach thermal equilibrium. Lastly, the experimental cell effect must be measured and characterized.

The Spring Constant

The spring constant was measured by gradually separating the capacitor plates using increasing force. A lever-fulcrum system was used to translate the downward gravitational force of the weights to an upward force. The fulcrum was placed equidistant from either end such that the ratio of forces were unity. Assuming the parallel plate capacitor equation is obeyed, the spring constant it taken as the linear gradient of the force as a function of spring displacement measured from the difference in plate separation (Fig. 3.10). The spring constant was found to be 1677±5.21 N/m.

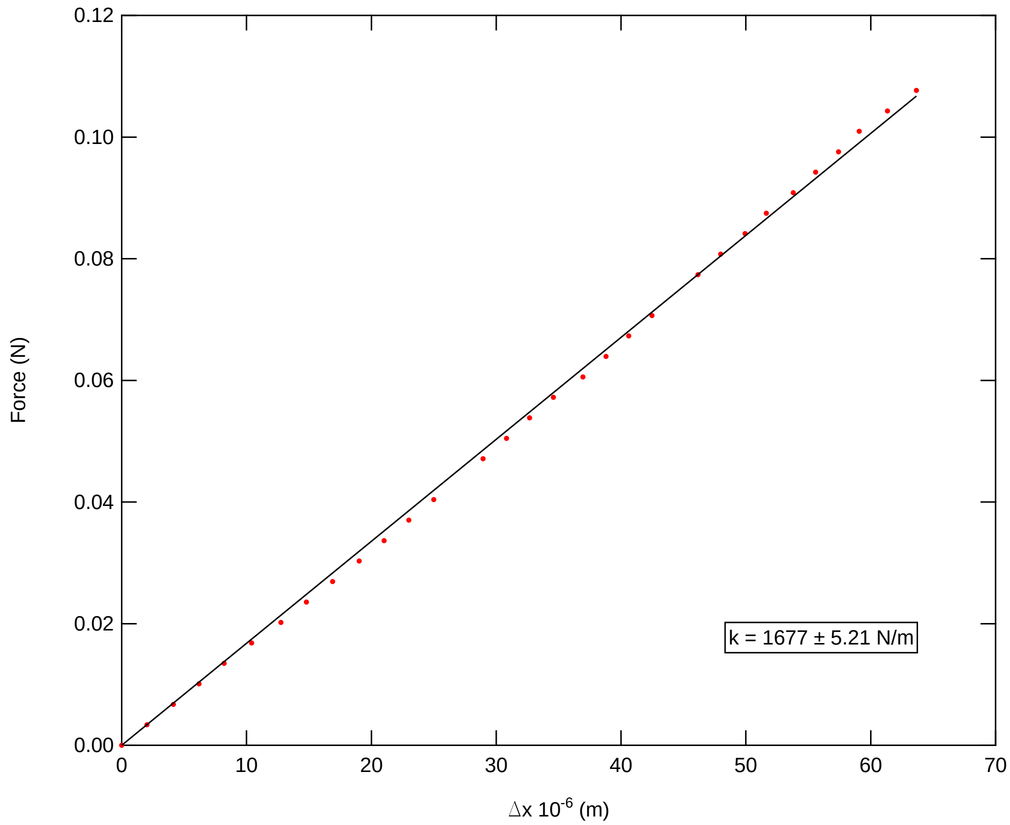

Figure 3.10: Graph of force as a function of spring displacement for the fused quartz dilatometer. The spring constant is the linear gradient of the results.

Thermal Time Constants

A measure of the time constraints for heating and cooling of the apparatus is determined. Without explicitly solving the heat equation the time constraint is estimated through separating the elements into thermal resistors and thermal (heat) capacitors. By this approach, the time constraint is measured by thermal time constants τ. It is defined as the time needed to reduce the initial temperature by a factor of the natural exponent e. The thermal time constant comes from the solution to Newton's law of cooling (3.19) and is determined by calculating the thermal resistance W and heat capacity C. Sections of both holding base and quartz dilatometer are calculated separately. The largest thermal time constant calculated should be a good representation of the time constraints of the apparatus. Theses calculations use values averaged over the 4-77 K temperature range.

$$\Delta T(t) = \Delta T_0 e^{-t/\tau} \qquad\qquad \tau = WC \tag{3.19}$$

The thermal resistance W of an object is defined by the length L along which the heat travels, cross sectional area A to the length and the thermal conductivity λ of the material. It is given as:

$$W = \frac{L}{\lambda A} \tag{3.20}$$

The thermal (heat) capacity C is the product of the volumetric specific heat capacity c_v and mass. The mass is computed by taking the volume V and density ρ at room temperature. It is given as:

$$C = c_v \rho V \tag{3.21}$$

The average thermal conductivity $\bar{\lambda}$ and average specific heat capacity $\bar{c_v}$ between 4-77 K and density ρ at room temperature for copper and quartz are collected in Table 3.1.

	$\bar{\lambda}_{4,77K}$ ($\mathrm{WK^{-1}m^{-1}}$)	$\bar{c_v}_{4,77K}$ ($\mathrm{mJg^{-1}K^{-1}}$)	ρ_{RT} (g $\mathrm{cm^{-3}}$)
Copper	80 [19]	30 [20]	8.96
Quartz	0.2 [21]	70 [21]	2.20 [22]

Table 3.1: Average values for copper and quartz between 4-77 K and density at room temperature.

The holding base is separated into two sections; tines and base. Heat is assumed to transfer along the length of the cylindrical tines and along the length of the approximately rectangular base. The quartz dilatometer is separated into three parts; bottom, top and spring. In the bottom component is assumed to transfer perpendicular to the capacitor face whereas the top component assumes heat is transferred parallel to the capacitor face. For the springs, the heat transfer is assumed to run along the length. The dimensions and results are presented in the following table.

The thermal time constant results (Table 3.2) show that the top and spring section have the dominant thermal time constants. By comparison, the other components have very small values that are negligible. An interesting result from these calculations show minimal contribution from the tines in the holding base. This would indicate the quantity of tines is sufficient such that it does not act as the limiting time constant.

	Qty.	Mat'l	L (mm)	A (mm^2)	V (cm^3)	W (KW^{-1})	C (JK^{-1})	τ (s)
Tine	91	Cu	12	$\phi = 0.8$	0.55	3.28	0.148	0.5
Base	1	Cu	44	3×15.5	2.0	11.8	0.538	6.3
Bottom	1	SiO_2	3.2	25×15	1.2	42.7	0.185	7.9
Top	1	SiO_2	22	3×15	1.0	2.44×10^3	0.154	376
Spring	2	SiO_2	19	0.18×15	0.1	1.76×10^4	0.0154	271

Table 3.2: Thermal time constant results of separate portions of the holding base and quartz dilatometer. The largest time constant is taken to be a good representation of the overall thermal time constant

To support the calculations, a test of the thermal equilibration time is performed. The thermal equilibration time test measures the time it takes for the system to return to a steady state after a temperature change. For this test, a temperature controller brings the system from 77 K to 78 K while a resistive thermometer (Cernox) attached on the top section of the quartz dilatometer (seen in Fig. 3.4 Left) monitors the temperature of the top plate. When the voltage reaches a steady state, the system is deemed to be in the new thermal equilibrium. The results seen in Fig.fig:TCexp show the device reaches a new equilibrium after approximately 6.5 minutes. Although the thermal equilibration time and thermal time constant are not exactly the same measure, the values from each are on the same order of magnitude. Based on these measurements and calculations, the thermal time constraint on the quartz dilatometer is estimated to be on the order of 10 minutes.

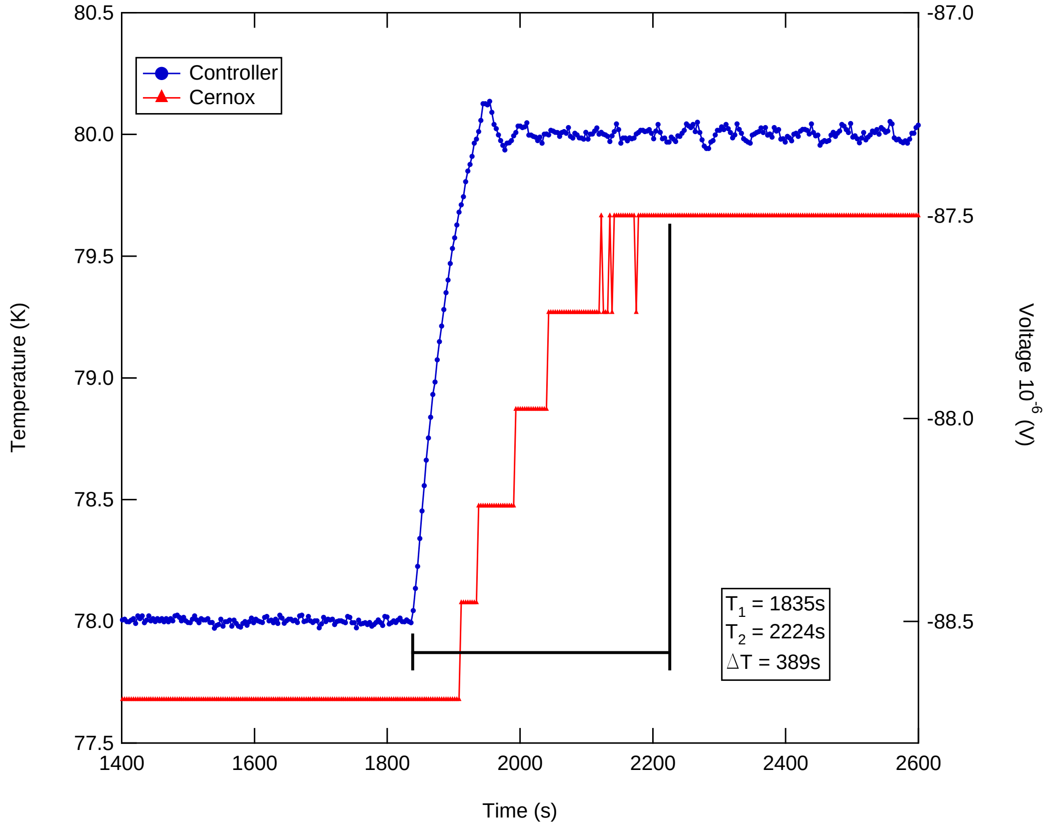

Figure 3.11: Thermal equilibration time test from 77-78 K on the quartz dilatometer. The temperature control (Blue) brings the system to a new temperature while a delayed effect is seen in the Cernox voltage (Red). The approximate thermal equilibration time is taken as the time difference between initial change and final change. The Cernox voltage is resolution is poor due to the incorrect settings on the measuring equipment.

Cell Effect Measurement

The cell effect of the quartz dilatometer is established. The theoretical cell effect is first calculated followed by measurement of the experimental cell effect.

The theoretical cell effect calculation assumes only thermal expansion perpendicular to the plate faces meaning the plate area remains constant as a function of temperature. Looking at the quartz dilatometer from the side, the (plate) separation D can be expressed as the sample length L_{sample} minus the distance the lower capacitor face is from the base of the sample L_{cell}.

$$D = L_{sample} - L_{cell} \tag{3.22}$$

Using the same approach to (3.3), thermal expansion coefficient of the sample expressed in terms of measured thermal expansion coefficient is:

$$\alpha_{sample} = \frac{1}{L_{0,sample}}\frac{dD}{dT} + \frac{1}{L_{0,sample}}\frac{dL_{cell}}{dT} \tag{3.23}$$

Recognizing L_{cell} is comprised of only quartz and that $L_{cell} \approx L_{sample}$, the cell effect term becomes:

$$\frac{1}{L_{0,Ag}}\frac{dL_{cell}}{dT} = \frac{L_{0,quartz}}{L_{0,Ag}}\alpha_{quartz} \approx \alpha_{quartz} \tag{3.24}$$

Therefore, the theoretical cell effect of the quartz dilatometer is approximately the thermal expansion coefficient of fused quartz (Fig. 3.5).

The experimental cell effect between 80-250 K is determined using silver as the benchmarking material. The silver values from Corrucini [13] are fit to the Einstein theory for solids [1] (Fig. 3.3 Inset) The theory predicts the specific heat (and by extension thermal expansion coefficient) follows (3.25). At sufficiently high temperatures, this is a good approximation for the specific heat [1]. The experimental cell effect is extracted from the difference between the fitted silver curve and the measured thermal expansion coefficient.

The results (Fig. 3.12) show quite a difference between the expected (theoretical) and measured (experimental) cell effect. A difference between the two results is also observed in [11] making this result less surprising. Observing the experimental cell effect, it could impact the interpretation of features on the order of magnitude of 10^{-6} in the thermal expansion coefficient.

$$C_v \propto Y\left(\frac{X}{T}\right)^2 \frac{e^{X/T}}{(e^{X/T}-1)^2} \tag{3.25}$$

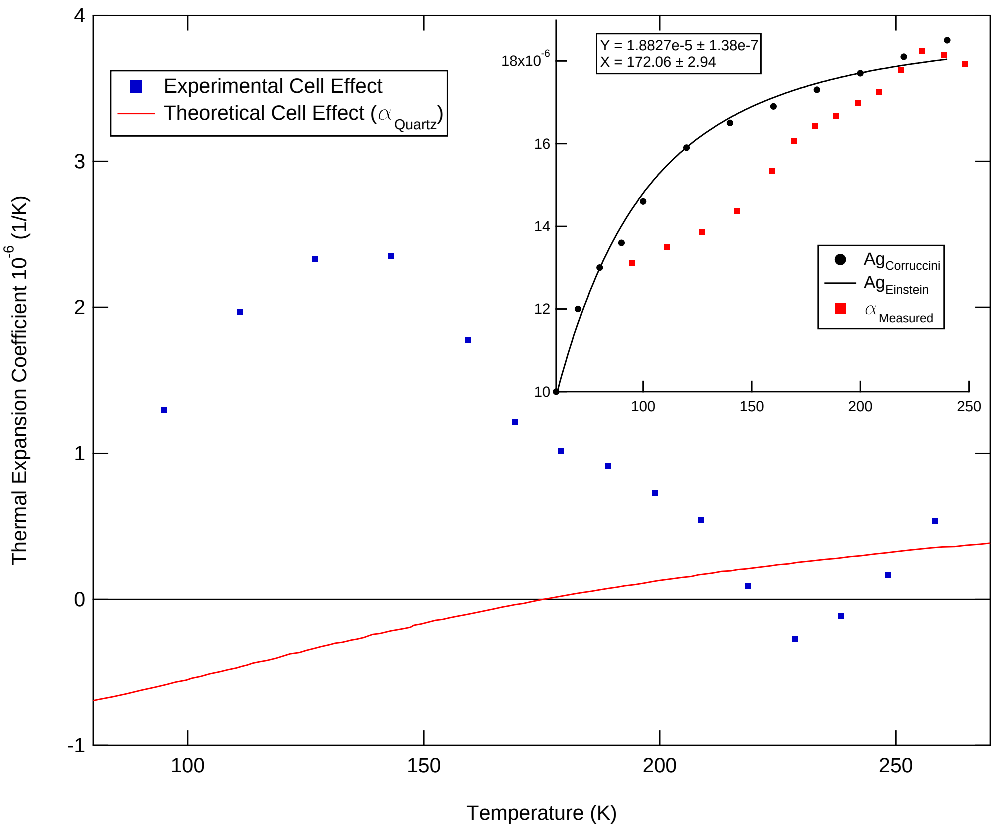

Figure 3.12: The experimental cell effect; a considerably larger and less behaved result than the theoretical calculation. **Inset:** A plot of the thermal expansion coefficient of silver [13] and the measured thermal expansion coefficient of silver

3.3.7 Conclusion

The fused quartz dilatometer was presented and benefits over the silver compact dilatometer were discussed. Assembly and mounting procedures were documented facilitating construction of more devices. Capacitor plate tilt and fringing effects contributions were discussed and calculated to contribute $< 5\%$ uncertainty; a marginal impact to the measurements. Several aspects of the quartz dilatometer were investigated; spring constant, thermal time constants and the cell effect. The spring constant was measured to be ≈ 1700 N/m and the thermal time constant was calculated to be on the order of 10 minutes. The measured cell effect of the quartz dilatometer between 100-250 K was observed to be non-negligible on the order of 10^{-6}.

There are several areas in which the quartz dilatometer can see improvement. The ideal ratio to which the sodium silicate glue is mixed can be further investigated particularly with durability to thermal cycles. Potential improvements to the holding base include using silver epoxy instead of lead based solder and optimizing the overall size. To properly use the tilted plate capacitor equation (3.16), a true measure of the tilt must be made. Currently, the plate tilt parameter a is assumed to be on the order of 10 μm. To reduce fringing effects further, guard rings similar to the design by Neumeier *et al.* [11] are recommended to be incorporated. With regards to improvements to the testing and calibration measurements, experimental results can be collected across a much larger range. In particular, the cell effect must be measured across the complete (temperature) range of operation. Additionally, effort to determine and reduce other contributions to the cell effect are highly recommended. Knowledge of the thermal time constant at low temperatures will become increasingly important as the conductivities of the materials used become considerably smaller.

3.4 Copper Dilatometer

This section discusses the development of the copper dilatometer. As with the fused quartz dilatometer, benefits of this design over the silver design are discussed. A detailed guide of the assembly of the device is presented. The copper design is in many ways similar to the silver compact dilatometer and need not be discussed in great detail. These aspects include mounting, plate tilt effects and fringe effects. This device is still in the testing phase as neither the spring constant nor cell effect at the intended operating temperature has been quantified.

3.4.1 Introduction

The copper dilatometer was made for the purpose of measurements in the low temperature domain $T < 1$ K where the thermal expansion coefficient of copper is small. This design takes elements from both the silver and quartz dilatometer designs. It is designed to function very similar to the silver dilatometer design but uses two separate springs similar to the quartz dilatometer design. Naturally, the design aimed to keep the diversity of materials is kept to a minimum. A cut-away diagram and photograph of the copper dilatometer is shown in Fig. 3.13.

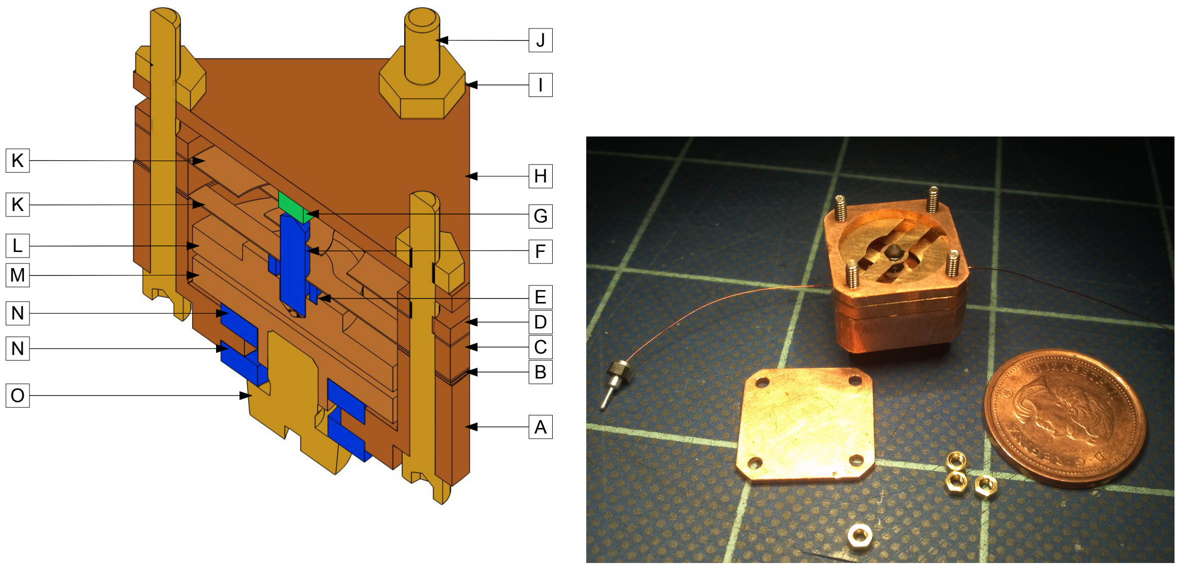

Figure 3.13: **Left:** A diagram of the copper dilatometer. The bottom shell (A) contains the bottom capacitor plate (M) fastened by an M3 brass screw (O). The bottom plate is electrically isolated from the rest of the device by two sapphire washers (N). The top capacitor plate (L) is electrically isolated from the device by sapphire ring (E) and rod (F). The top plate is fixed to two beryllium-copper springs (K) which are separated by a spring spacer (C). The plates are naturally separated by a shim (B) inserted underneath the bottom spring. All components are fastened together by 0-80 brass screws (J) and a compressor ring (D) that has threaded 0-80 holes. The sample (G) is pressed up against the sapphire rod and is held in position by the top shell (H) positioned by 0-80 brass nuts (I). When assembled, the dilatometer measures 15-20 mm long depending on the sample size. The outer cross-section of the shell is a 15 mm square, an inner circular bore contains the other components shown. All inner components are circular and concentric with the inner bore of the shell. The area of the circular capacitor plates is approximately $115mm^2$. **Right:** The assembled copper dilatometer with the top removed. The springs are seen aligned perpendicular to one another reducing the potential for non-linear movement.

The versatile design is capable of handling a large variety of sample comparable to size handled by the silver compact dilatometer. Operating in a similar manner to the silver compact dilatometer, many of the same principles can be directly translated to this design. However, this design emphasizes on keeping the capacitor plates as stationary as possible. Should the need arise for greater plate separation for materials with larger thermal expansion coefficients, insertion of additional shims would facilitate the need.

A notable difference from the silver design is the absence of large threaded components. There was concern regarding these components in the silver design where it was believed the 'slop' of the threads on the stainless steel positioners and silver shell and would adversely affect the position of the sample. Although the stainless steel nuts served to remove such play in the threading, the difference in thermal expansion coefficient of the could cause an unpredictable shift in the position of the sample. The problem cannot be solved by making the positioner silver as the risk of thread galling would be prevalent. Furthermore, as silver is a relatively soft metal, there would be high risk of stripping the threads.

This design uses fine threaded brass screws to ensure the copper components remain together. This is possible using the fact that the thermal expansion coefficient of brass is in general greater than copper (Fig. 3.14). Therefore, as the device is cooled, the brass components shrink more than copper. This approach is particularly beneficial as the design can be made such that the brass components do not contribute to the cell effect.

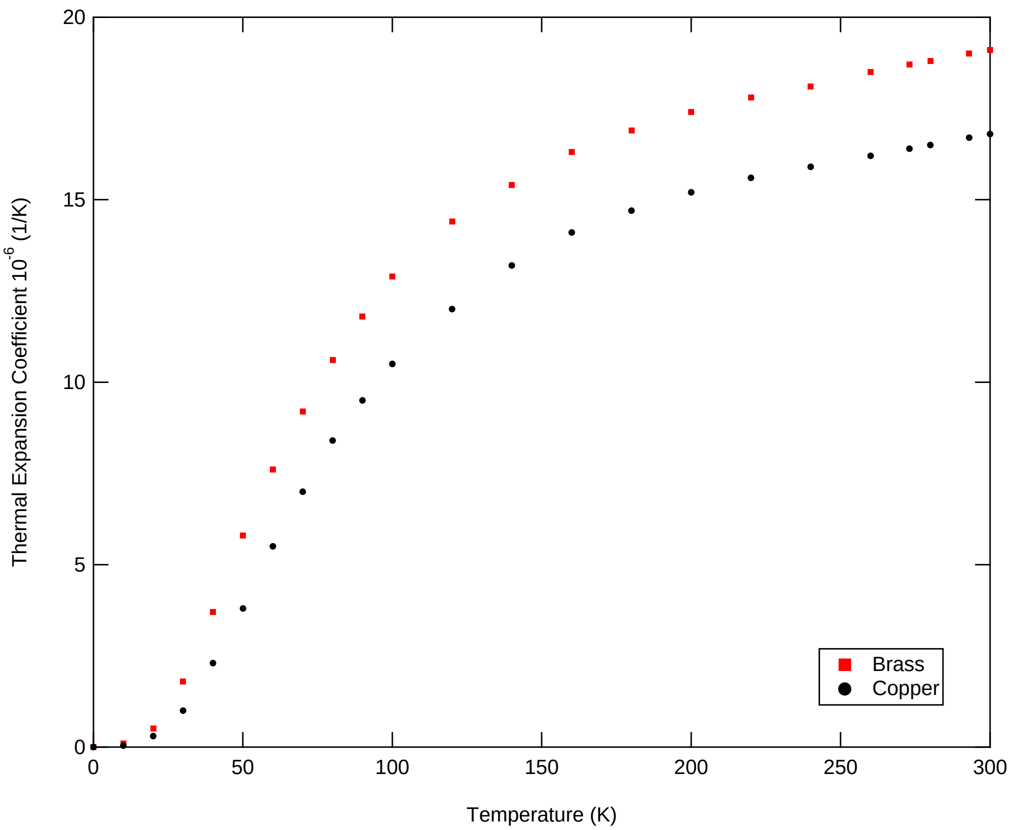

Figure 3.14: The thermal expansion coefficient values of brass and copper as per Corrucini [13]. The thermal expansion coefficient for brass remain larger than copper in general making brass an ideal material to fasten copper components.

Another particular change in this design over the silver design is the use of Stycast 2850 epoxy is kept to a minimum. This epoxy is only present in the assembly of the moving plate and used very minimally. This design holds the fixed plate by a brass M3 screw. The concern was that the epoxy, comprised of many different compounds, if used in larger quantities could be adversely effect the position of the capacitor plates.

The spring mechanism in this design copies the double spring approach of the quartz design. Two individual springs are positioned apart by a copper spacer but are attached together through a sapphire rod. In the same manner as the quartz design motion would then be restricted to a single direction.

The spring constant of the copper design is predicted to be lower than that found in the silver design. This is because lowering the spring constant in the silver design relied heavily on the ability of the machinist to make the thinnest 'cup' spring. The copper design is not limited by this as the springs are cut from stock beryllium copper sheet thinner than what is easily machinable.

The rest of this section will focus on the assembly process and testing and calibration. No special mounting considerations are necessary as the device. The copper design has no particular difference to the tilted plate and fringe effects considerations were covered in Dunn's MSc thesis [7]. To summarize the effects, the tilted plate considerations for this dilatometer follow 3.3.4 while the fringe effects are neglected as the outer shell of the dilatometer is grounded and close to the plates. The spring constant is measured and the theoretical cell effect is calculated. The cell effect for intended operating temperatures is has not been measured.

3.4.2 Assembly

As with the quartz dilatometer, the assembly places emphasis on retaining parallel plates. This is achieved by assembling the dilatometer with the two plates directly on top of one another. Once assembled, the plates are separated by inserting shims into the device. This will become more clear once the assembly is described. All the components are fabricated as per the schematics found in Appendix E.

The fixed bottom plate is assembled to the bottom shell with sapphire washers and electrical lead. A strip of Kapton is placed around the fixed plate to serve as a guide for positioning the moving capacitor plate. The electrical lead for the top plate is attached using silver epoxy. Once dry, the sapphire post and ring are epoxied into place using Stycast 2820FT. This assembly is now placed on top the bottom plate ensuring the lead wire is seated into the specifically made groove on the bottom shell.

Next, the 0-80 brass screws are inserted which will act as a guide pins for the rest of the components. The first spring is placed on top the bottom shell and is epoxied using Stycast. The spring spacer is next to be placed on top followed by the second spring in the correct configuration. Once the second spring is epoxied with Stycast, the components are clamped together using the compression ring. The Stycast is now cured as per curing instructions found in Appendix F.

Once the epoxy is cured, the assembly is disassembled to insert the shims below the first spring and to remove the Kapton. Once the dilatometer is reassembled and compression ring fastened, it should not need to be re-opened unless additional shims are to be inserted.

3.4.3 Testing and Calibration

Once again, aspects of the dilatometer are to be characterized. As mentioned earlier however, the copper dilatometer is in the testing phase requiring measurement of the experimental cell effect at operating temperatures. The spring constant of the dilatometer was tested but few data points were taken. Thermal time constants were not calculated and were deemed unnecessary as the device is assumed to have great thermal conductivity as it is nearly completely copper. The theoretical cell effect is calculated and discussed.

The Spring Constant

The spring constant was measured by loading weights onto a post that depresses the springs. As weights are loaded, the spring is further deflected observable by the increase in capacitance. Once again, assuming the parallel plate capacitor equation is obeyed, the spring constant it taken as the linear gradient of the force as a function of spring displacement measured from the difference in plate separation (Fig. 3.15). The spring constant was found to be 7263.9±372 N/m.

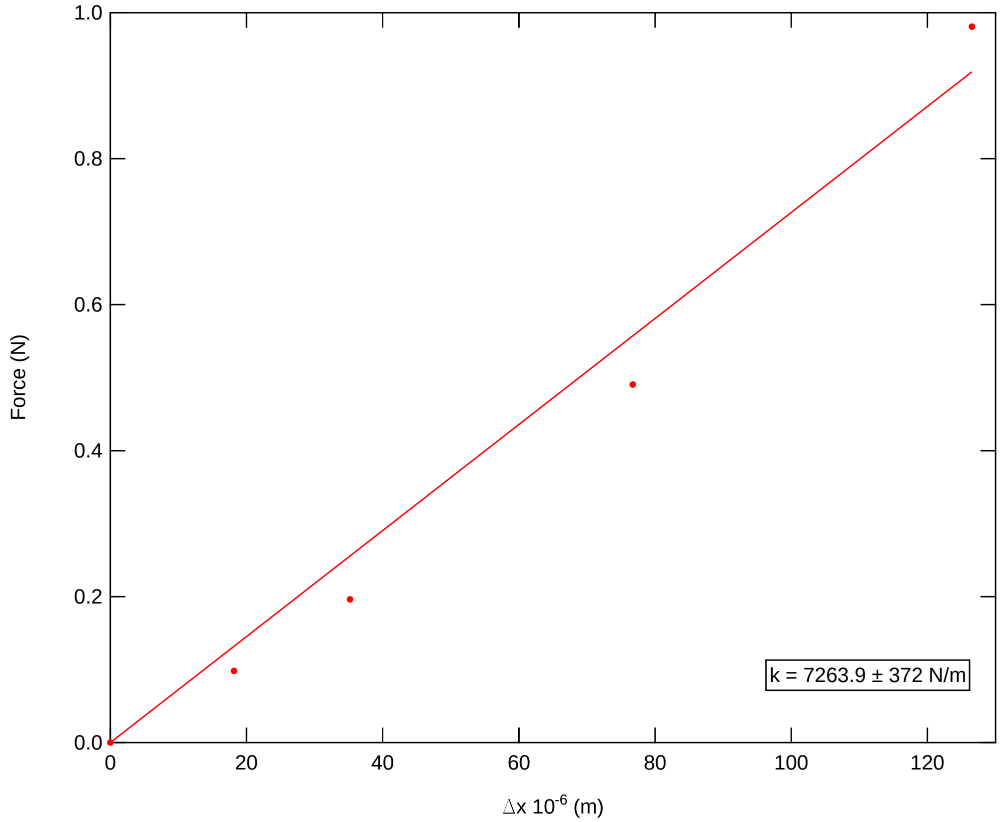

Figure 3.15: Graph of force as a function of spring displacement for the copper dilatometer. The spring constant is the linear gradient of the results.

Cell Effect Measurement

The theoretical cell effect is calculated for the copper dilatometer. Using the same approach as the quartz dilatometer calculation, the plate separation D can be expressed as the difference between the distance the bottom capacitor face is from the top of the sample L_{outer} and the combined length of the silver sample L_{sample}, sapphire pin L_{pin} and top plate L_{plate}.

To make the proceeding derivation easier, the brass screws are assumed to be copper which, from a thermal expansion coefficient perspective are relatively equal. Differentiating with respect to temperature, dividing by the sample length and rearranging, the following is drawn:

$$\frac{1}{L_{0,sample}}\frac{dD}{dT} = \frac{1}{L_{0,sample}}\frac{dL_{outer}}{dT} - \alpha_{sample} - \frac{1}{L_{0,sample}}\frac{dL_{pin}}{dT} - \frac{1}{L_{0,sample}}\frac{dL_{plate}}{dT} \tag{3.26}$$

If the negligible thermal expansion coefficient argument were used here, all terms but α_{sample} are assumed to be zero. However, this argument assumes that the leading thermal expansion comes from the sample and are negligible by comparison. Without *a priori* knowledge of the thermal expansion coefficient of the sample, and the general order of magnitude of the cell effect, the cell effect cannot be assumed to be negligible. Therefore, the theoretical cell effect must be calculated to determine the order of magnitude. To simplify the cell effect calculation, the brass components are assumed to be copper which from a thermal expansion coefficient perspective, is an acceptable assumption. (3.26) is written as:

$$\frac{1}{L_{0,sample}}\frac{dD}{dT} = \left(\frac{L_{0,outer} - L_{0,plate}}{L_{0,sample}}\alpha_{Cu} - \frac{L_{0,pin}}{L_{0,sample}}\alpha_{sapphire}\right) - \alpha_{sample} \tag{3.27}$$

Unlike the quartz dilatometer, the sample length directly impacts the scaling factor to the cell's material thermal expansion coefficients are multiplied to. Separating $L_{0,outer}$ into the sample dependent portion, the initial plate separation D_0 and the remaining length, assuming $D_0 \ll L_{0,outer}$ and inserting known dimensions of the dilatometer the cell effect contribution becomes:

$$\left(\frac{L_{0,outer} - L_{0,plate}}{L_{0,sample}}\alpha_{Cu} - \frac{L_{0,pin}}{L_{0,sample}}\alpha_{sapphire}\right) = \left(\frac{4.25mm + L_{0,sample}}{L_{0,sample}}\alpha_{Cu} - \frac{5.5mm}{L_{0,sample}}\alpha_{sapphire}\right) \tag{3.28}$$

An unfortunate consequence, these scaling factors become large appreciably large with smaller samples. For example, a typical sample length of 1-2 mm would result in scaling factors of approximately $3 - 5$.

Regardless of the consequences of the theoretical cell effect, the experimental cell effect still must ultimately be measured.

3.4.4 Conclusion

The copper dilatometer design was presented and particular improvements over the other designs were discussed. The procedure to assemble the copper dilatometer was outlined.

The tilted plate equation was outlined in a previous section (3.3.4) and fringe effects were deemed to be negligible attributed to the close proximity of the outer shell which serves as a grounded guard ring. The spring constant was measured to be 7263.9±372 N/m. The thermal time constant not calculated by assumed to be short due to the large thermal conductivity of copper. The theoretical cell effect expression was derived where scaling factors can appreciably increase the cell effect contribution depending on the size of the sample. Further development of this device is needed to bring the copper dilatometer to the same level as the silver compact dilatometer and the fused quartz dilatometer.

Chapter 4

$\mathbf{LiHoF}_4$

The ferromagnetic material $LiHoF_4$ is studied using the silver compact dilatometer. Being a candidate material for the transverse field Ising model, a quantum phase transition is present in $LiHoF_4$ [23]. Critical points are extracted through measurement of the thermal expansion coefficient and magnetostriction at $T \approx 1.3 - 1.8$ K and $H \approx 0 - 4$ T. Having previously been studied in Dunn's MSc thesis [7], this study focuses on measurements near the classical critical point $T_c|_{H=0}$ where there was a possibility of re-entrant behaviour [7] and approaching the quantum critical point $\Gamma_c|_{T=0}$ where point density was lacking.

This chapter will briefly cover the background and recent measurements of $LiHoF_4$ up to Dunn's MSc results. Thermal expansion coefficient and magnetostriction measurements made since are presented, critical points are extracted and are added to the existing phase diagram. Further details regarding the study of $LiHoF_4$ are published in [24].

4.1 Introduction

So far in this thesis, phase transitions have been discussed from a general, classical perspective. The classical phase transition occurs at finite temperature and are driven by thermal fluctuations evident by the ability to observe them in temperature dependent properties like the thermal expansion coefficient. However, at absolute zero such thermal fluctuations do not exist as these classical systems freeze into a ground state absent of fluctuation [25]. In certain systems, particularly magnetic ones, non-thermally driven phase transitions called quantum phase transitions exist at zero temperature. These quantum systems have fluctuations driven by the Heisenberg uncertainty principle and have implications toward understanding the quantum nature of materials [25]. As all experiments are at some non-zero temperature, the quantum phase transition is described by the evolution of physical properties at finite temperatures approaching zero [25].

Materials with quantum phases are of particular interest as they are believed to be tied to other emergent phenomena. For example, a quantum phase transition is hidden below the superconducting region of high temperature cuprates [23, 24]. However, understanding a quantum phase transitions is better practised on a less complicated system such as the Ising ferromagnet $LiHoF_4$ in transverse magnetic fields.

4.2 Background and Recent Measurements

The magnetic spin behaviour of $LiHoF_4$ comes from the Ho^{3+} ions arranged in a face centred tetragona structure (Fig. 4.1). The Ho^{3+} ions have a $4f^{10}$ electronic structure which by Hund's rules form a 17 fold degenerate free ion spin state $^5I_8$ [24]. The Li^+ and F^- ions generate a large crystal field forming a non-Kramers doublet ground state with spins aligned or anti-aligned to the c-axis [24]. The first excited state is a singlet and is approximately 11 K above the ground state energy [24]. Therefore, at energies below the first excited state, the material has Ising anisotropy.

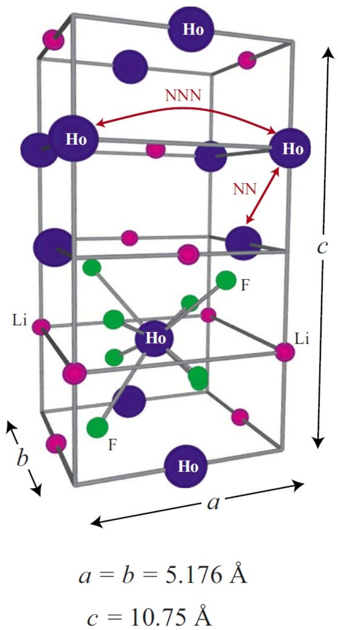

Figure 4.1: Crystal structure of $LiHoF_4$ with corresponding lattice parameters from Tabei *et al.* [26]. The low temperature magnetic structure has Ising spins on the Ho^{3+} sites pointing parallel or anti-parallel along the c-axis.

Application of a magnetic field transverse to the Ising axis couples two Ising states allowing quantum mechanical tunneling between the two states [24]. With sufficiently large magnetic field strengths, the increased tunneling rate can destroy the long range magnetic order of the Ising system [25]. This is indicative of a quantum phase transition as a macroscopic property is driven by non-thermal fluctuations. $LiHoF_4$ has a Curie Temperature $T_c = 1.53$ K indicative of ferromagnetic ordering a low temperatures [27]. The coupling was determined (by specific heat [28] and susceptibility measurements [29]) to be dominantly dipolar that is ferromagnetic with an antiferromagnetic super-exchange coupling smaller by approximately a factor of two.

The Hamiltonian for the Ising magnet in a transverse magnetic field is given as [26]:

$$H = -\frac{1}{2}\sum_{i>j}^{N} J_{ij}\sigma_i^z\sigma_j^z + \Gamma\sum_{i}^{N}\sigma_i^x \tag{4.1}$$

The first term is the Ising spin model for z oriented Pauli spin operators σ_i^z and effective interaction J_{ij}. The second term is contribution of the effective transverse field Γ and represents the mixing of the two Ising states [24]. For $T = 0$ K, a non-zero Γ permits quantum mechanical fluctuations and which when sufficiently large $\Gamma = \Gamma_c$, destroys the magnetic ordered phase; the quantum critical point.

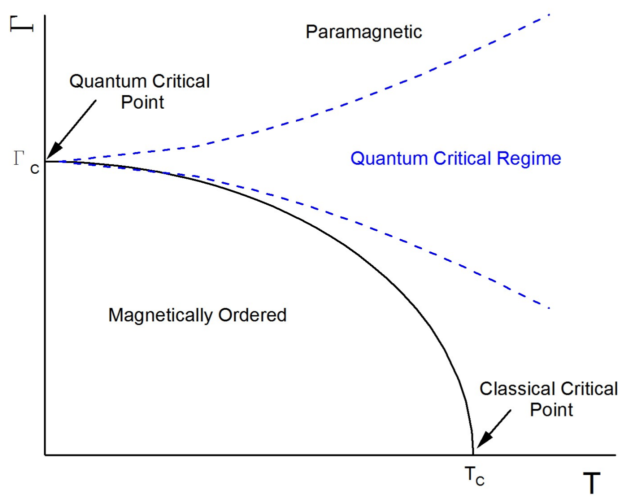

Figure 4.2: A schematic phase diagram of the transverse field Ising model in effective transverse field-temperature phase space. The solid line is the phase boundary separating paramagnetic and magnetically ordered phases.

The first measurement of phase boundary of $LiHoF_4$ performed by Bitko *et al.* [23] used measurements of magnetic susceptibility down to milliKelvin temperatures (Fig. 4.3). Using mean field theory and the transverse component of the Landé g-factor tensor and the spin-spin coupling strenth as adjustable parameters, a reasonable fit to the experimental results were obtained. However Chakraborty *et al.* [30] later showed that the adjustment of the Landé g-factor was inappropriate for $LiHoF_4$ [7].

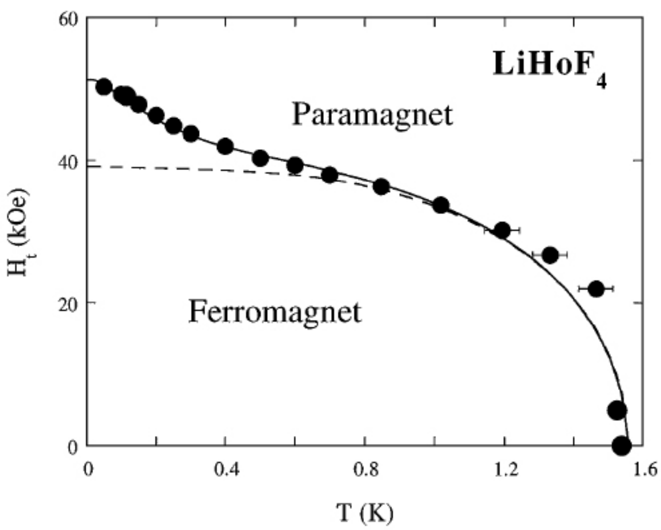

Figure 4.3: Transverse magnetic field-temperature phase diagram of $LiHoF_4$ by Bitko *et al.* [23]. Experimental results are the filled circles. The dashed line is a mean-field theory fit considering only electronic spin degrees of freedom while the solid line is a fit incorporating the nuclear hyperfine interaction. Both mean-field lines used the same fitting parameters; the transverse component of the Landé g-factor tensor and the effective longitudinal spin-spin coupling strength.

Considerable work has been done to improve the theoretical transverse magnetic field phase diagram for $LiHoF_4$ including using a full microscopic Hamiltonian containing crystal field effects, magnetic dipolar and exchange coupling and hyperfine coupling [24]. A full microscopic Hamiltonian approach using quantum Monte Carlo simulations was done by Chakraborty *et al.* [30]. Despite using a more accurate Hamiltonian with parameters fixed where possible, a discrepancy remained between the data close to the classical critical point. This was reported as reflecting the potential uncertainties in the crystal-field parameters for $LiHoF_4$ [30].

Work on $LiHoF_4$ by Rønnow *et al.* [31] using neutron scattering [32] found a similar discrepancy between experimental and theoretical results. The theoretical calculation used crystal-field parameters from spectroscopic measurements[33, 34, 35] on Ho-doped $LiYF_4$. Despite using different parameters, the computed phase line did not match the experimental results at low transverse field strengths. Based on this persistent discrepancy, the different crystal-field parameters are likely not the source of the issue [24].

Theoretical work by Tabei et al. [26] attempts to address the disagreement between theoretical and experimental phase boundary at low transverse fields [30, 31]. The approach was to introduce quantum fluctuations perturbatively into the classical Hamiltonian possible since the quantum fluctuations are small in this regime. The sources of discrepancy were isolated into computational and Hamiltonian inadequacies. It was concluded that the discrepency was not of computational origin nor was it from uncertainties in the crystal-field parameters leading to the belief that it was due to shortcomings in the model Hamiltonian (4.1)[24].

Although considerable effort has been made to improve the theoretical model of $LiHoF_4$, there was lack of effort to further develop and verify the experimental results. Experimental measurements on $LiHoF_4$ in measuring the phase boundary are presented in Dunn's MSc thesis [7]. The critical points are determined through thermal expansion coefficient and magnetostriction measurements via capacitive dilatometry. The results (Fig. 4.4) show good agreement with Bitko *et al.* while strongly disagreeing with theoretical calculations by Tabei *et al.* [26].

The results presented in this thesis work address concerns regarding the results presented in Dunn's MSc thesis (Fig.4.4). In the low transverse field regime, the estimated phase boundary becomes very steep and quite possibly re-entrant in behaviour. In this situation, re-entrance would manifest itself by a higher critical temperature at a non-zero applied transverse field. As a consequence, it is possible to follow an isothermal line that crosses the phase boundary twice. This re-entrant behaviour would be possible if the effective interaction were magnetic field dependent. Since that the effective interaction of $LiHoF_4$ is already suppressed by a non-dominant antiferromagnetic exchange coupling component, application of transverse field this term could further suppress the exchange coupling more than the ferromagnetic dipolar coupling. As a result, the effective interaction becomes increasingly ferromagnetic with application of transverse magnetic field permitting a higher critical temperature than the classical critical value. However, at higher transverse field strengths, quantum mechanical tunnelling begins to dominate competing with the ferromagnetic state thus lowering the critical temperature once more. A high point density study at low transverse field strengths work to address the possibility of re-entrant behaviour.

In addition to low transverse field measurements, magnetostriction measurements are also performed at temperatures approaching the critical field point.

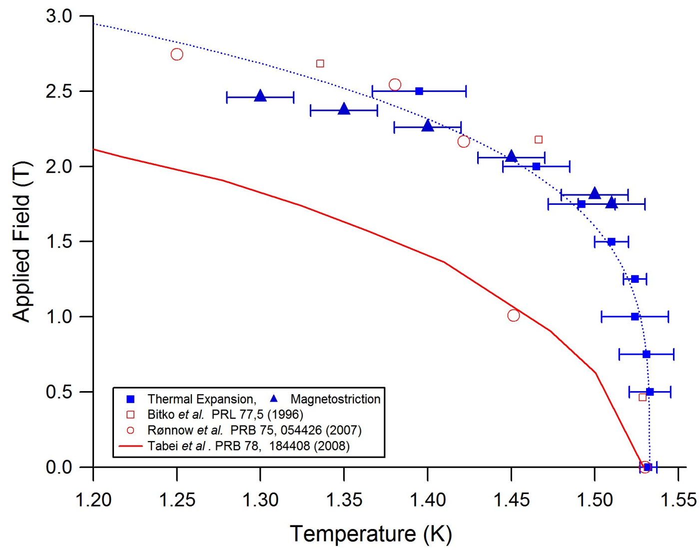

Figure 4.4: The phase diagram of $LiHoF_4$ of transverse field versus temperature from Dunn's MSc thesis [7]. The low point density in low transverse field regime coupled with the large uncertainty indicate the possibility of re-entrant behaviour. Results from Bitko *et al.*[23], Rønnow *et al.*[31] and Tabei *et al.*[26] are also shown.

4.3 Experimental Method

The sample used in these measurements and measurements found in Dunn's MSc thesis came from a commercially produced single crystal [36]. The sample measures approximately 1 mm thick, 5.5 mm long, and approximately 3.5 mm across the widest point. The direction of measure of the $LiHoF_4$ sample was determined to within $\pm 1°$ of the c-axis [001] using a commercial Laué diffraction apparatus. The ends of the crystal were polished to be orthogonal to the [001] direction within 2.5°.

The magnetostriction and coefficient of thermal expansion were measured along the [001] direction using the silver compact dilatometer (3.2). A pumped ^{4}He cryostat capable of reaching ≈ 1 K was used for the measurements. The temperature was controlled using a LakeShore 331 Temperature Controller and measured using a calibrated Cernox CX-1030 resistive thermometer located on the cold plate. For the coefficient of thermal expansion measurements, the temperature was swept at a rate of 7.5 mK/min between 1.2-1.8 K while capacitance was continuously measured. For the magnetostriction measurements, the magnetic field was swept at a rate of 0.2 T/min while capacitance was continuously measured. The capacitance was measured using an Andeen-Hagerling 2500A capacitance bridge.

Magnetostriction is the normalized physical size change of a material due to applied magnetic field and is analogous to the thermal expansion with temperature. It is given as:

$$\lambda(H) = \frac{\Delta(L(H))}{L_0} \tag{4.2}$$

Critical points are determined as the point where the first deviation from the paramagnetic behaviour is observable. This applies for both thermal expansion coefficient and magnetostriction results.

Cernox resistance thermometers have a small magnetoresistance which must be accounted for to obtain the correct critical (temperature) point. This correction is particularly important in the low transverse field regime where there are only small shifts in the critical point. Magnetoresistance corrections are factored into all critical temperature points and the correction values are obtained by interpolating data from Brandt *et al.* [37].

The correction to the critical points were determined by extrapolating data from Brandt *et al.* [37] from higher transverse fields to lower values used in the measurements. The paper provides resistance correction values (ΔR/R) as a function of temperature for specific field strengths. These values are related to a temperature change (ΔT/T) using a sensitivity term S_T. The equation is given as:

$$\frac{\Delta T}{T} = \frac{\Delta R}{R} S_T \qquad\qquad S_T = \frac{T}{R}\frac{dR}{dT} \tag{4.3}$$

The sensitivity term is obtained using the resistive thermometer calibration curve relating measured resistance to a specific temperature. ΔR/R values for field strengths used in the measurement were obtained by quadratic fitting values taken along the isothermal line of the critical temperature value obtained in the raw measurement.

4.4 Results and Discussion

The thermal expansion coefficient is measured at low transverse field ($H_t = 0 - 0.75$ T) (Fig. 4.5). As originally observed (Fig. 4.4), very small shifts in the critical point are expected in this regime. The critical points have not been magnetoresistance corrected and must be plotted on the phase diagram to make a true assessment of the possibility of re-entrance.

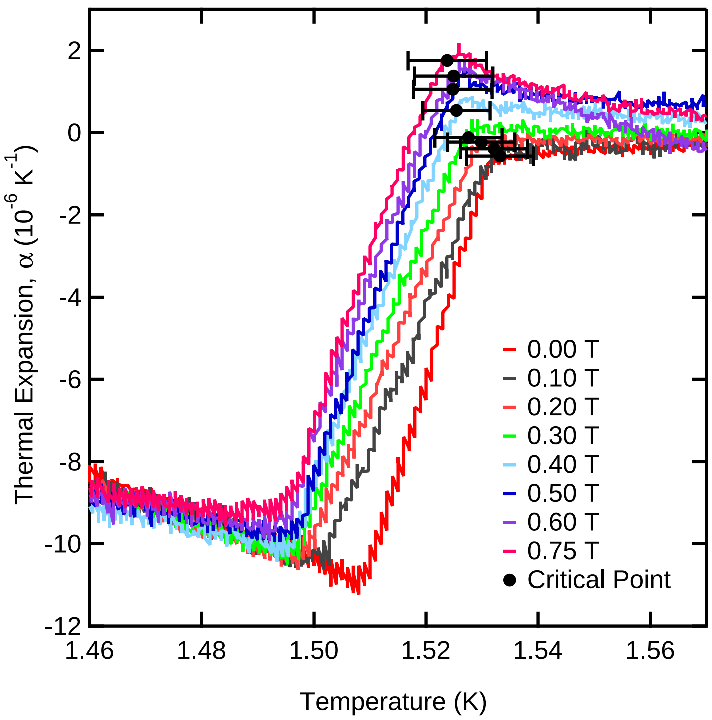

Figure 4.5: Plot of the thermal expansion coefficient results of $LiHoF_4$ at low transverse field strengths. The critical points shown have not been corrected for magnetoresistance contributions.

The magnetostriction is measured for temperatures ranging between 1.30-1.51 K (Fig. 4.6). Extracting the critical points from the magnetostriction curves using the two paramagnetic results (at 1.60 K and 1.80 K) is difficult as all the curves are very broad and relatively featureless. Extracting critical points directly from here would result in a large uncertainty. However, in the second derivative with respect to transverse field (Fig. 4.6 b)), a deviation from the paramagnetic state is more easily observed. That is, subjecting the same conditions for determining critical points to the second derivative of magnetostriction with respect to applied field, the critical points are extracted.

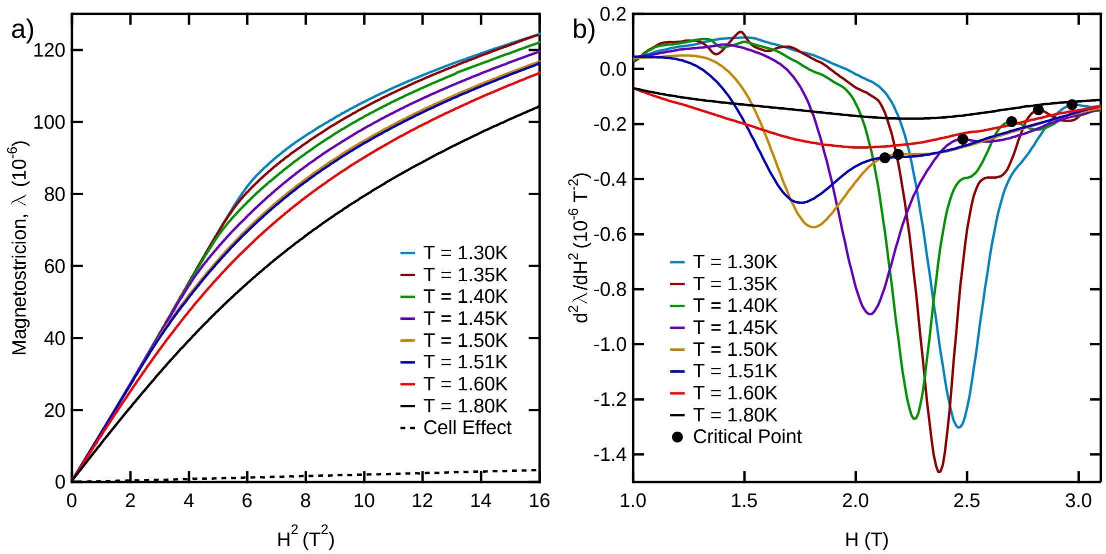

Figure 4.6: a) Magnetostriction measurments as a function of the square of the transverse field, H^2. b) Second derivative of magnetostriction with respect to magnetic field versus transverse magnetic field. The critical points determined using the same conditions as the thermal expansion coefficient.

All the newly acquired critical points were added to the transverse field-temperature phase diagram (Fig. 4.7). The added results of the low transverse field measurements indicate no evidence of re-entrant behaviour since the critical temperature values show a clear decrease with increasing transverse field vales.

This conclusion was only brought about by the magnetoresistance correction applied to the critical temperature values. The critical points extracted from the magnetostriction measurements increase the point density along the experimental phase boundary and follow the experimental phase boundary previously defined.

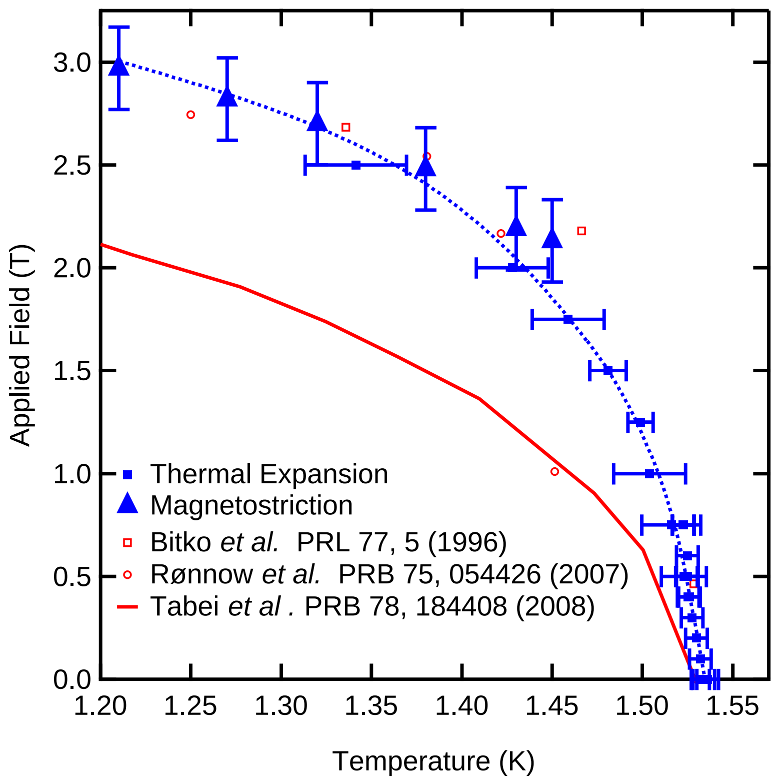

Figure 4.7: The transvers field-temperature phase diagram of $LiHoF_4$ with new critical points inserted. The low transverse field study confirms no re-entrant behaviour.

4.5 Conclusion

In conclusion, the point density of the experimental phase boundary of $LiHoF_4$ has been increased paying particular attention to the low transverse field regime. The greater point density in this regime along with magnetoresistance considerations [37] indicate no re-entrant behaviour in $LiHoF_4$. Currently, there is no theoretical model that accurately describes the experimental results. The question remains as to the origins of this discrepancy; whether it is a lack of understanding the nature of quantum fluctuations at finite temperatures or whether it pertains to details of the $LiHoF_4$ system [24]. A more recent material Fe_8 has similar physics to $LiHoF_4$ and also shows a similar disagreement to theoretical calculations near the classical critical point [38]. Further research into this material may reveal the underlying physics behind the discrepancy in $LiHoF_4$.

Chapter 5

$Tb_2Ti_2O_7$

The highly debated material $Tb_2Ti_2O_7$ is measured using the silver compact dilatometer along the [001] direction. This material has attracted considerable attention largely due to differing experimental results [39, 40, 41]. Evidence of phase transitions are determined through measurement of the thermal expansion coefficient for $T < 1$ K. Having previously been studied in Dunn's MSc thesis [7], this study focuses on improving the results through higher resolution measurements.

This chapter will briefly cover the background and recent measurements of $Tb_2Ti_2O_7$ up to Dunn's MSc results. Thermal expansion coefficient measurements made since then are presented. The results are fit into likely scenarios regarding the low temperature phase of $Tb_2Ti_2O_7$.

5.1 Introduction

The pyrochlore oxides are of great interest in condensed matter due to their rich and diverse magnetic behaviour. Having the stoichiometric form $A_2^{3+}B_2^{4+}O_7$, a magnetic rare-earth ion A and transition metal B form two interpenetrating corner sharing tetrahedra lattices (Fig. 5.1) [42]. The magnetic behaviour observed in the pyrochlore oxides are caused by geometric frustration. In magnetic systems, geometric frustration describes a situation where the geometry or lattice causes the magnetic spins to behave in unique ways. As an example, consider the ground state of a 2D triangular lattice Ising system with antiferromagnetic (AFM) coupling. Within a triangle, two spins will align correctly but the last spin will not satisfy the antiferromagnetic condition with respect to one of the spins. As a consequence, two configurations with equivalent energy are equally valid creating a situation where the ground state is degenerate. The presence of geometric frustration in more complex lattices lead to many exotic outcomes. A possible outcome on the pyrochlore lattice is the spin liquid state; the case where the spin system fails to form order[42].

A comprehensive outline of many pyrochlore oxides is reviewed by Gardner *et al.* [42] describing many the exotic spin configuration in greater detail. Of the many pyrochlore oxides, terbium titanate ($Tb_2Ti_2O_7$) has become particularly popular due to its anomalous behaviour at low temperatures $T < 1$ K. It is believed that $Tb_2Ti_2O_7$ exists on the cusp of the boundary between antiferromagnetic and spin ice phases and can be influenced by slight differences such as exchanges beyond nearest neighbour [43]. As such, the material holds a rich, diverse low temperature behaviour.

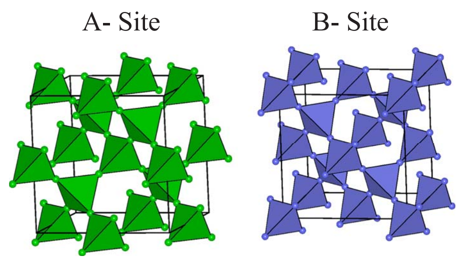

Figure 5.1: Picture of the pyrochlore structure from Gardner *et al.* [42]. Two interpenetrating corner sharing tetrahedra one containing the magnetic rare-earth and the other the transition metal form the lattice of the pyrochlore oxide. Geometric frustration gives rise to exotic magnetic behaviour.

5.2 Background and Recent Measurements

The magnetic behaviour of $Tb_2Ti_2O_7$ come from the Tb^{3+} ions with a $7F^6$ electronic structure arranged on a pyrochlore lattice [42]. From neutron scattering and dc susceptibility measurements, the ground state and first excited state were determined to be doublets followed by two singlets at much higher (2.5 and 3.5 THz) energy by Gingras *et al.* [44]. Crystalline electric field calculation suggested the Tb^{3+} have a $5\mu_B$ moment and a strong anisotropy in the $\langle 111 \rangle$-axis [44] implying near-Ising spins aligned along the local $\langle 111 \rangle$ directions. The exchange was determined to be antiferromagnetic from the negative Curie-Weiss temperature on the of order 10 K determined by dc magnetic susceptibility [44].

Muon spin relaxation measurements revealed no long range ordering (LRO) down to 70 mK [45]. The absence of LRO and the AFM exchange lead to the conclusion that $Tb_2Ti_2O_7$ was a spin liquid at low temperatures.

Contrary to this conclusion, specific heat measurements by Hamaguchi *et al.* [41] and Takatsu *et al.* [39] reported a peak around 400 mK evident of a phase transition. However, alternative specific heat measurements by Youanc *et al.* [40] showed results with the absence of any feature at 400 mK. This differing result could have come from sample dependence as Chapuis' PhD [46] thesis showed specific heat results that differed with sample growth parameters (Fig. 5.2 Left). Most recently, Taniguchi *et al.*[47] showed a strong dependence on sample stuffing (Fig. 5.2 Right) being able to suppress and shift of a 500 mK peak in the specific heat. They proceed to a propose a sample stuffing-temperature phase diagram (Fig. 5.2 Right Inset) in the low temperature region. The phase diagram indicates the development of either an LRO state or spin liquid state at low temperatures depending on the stuffing factor x. This predicted phase diagram would explain the vast difference in specific heat results.

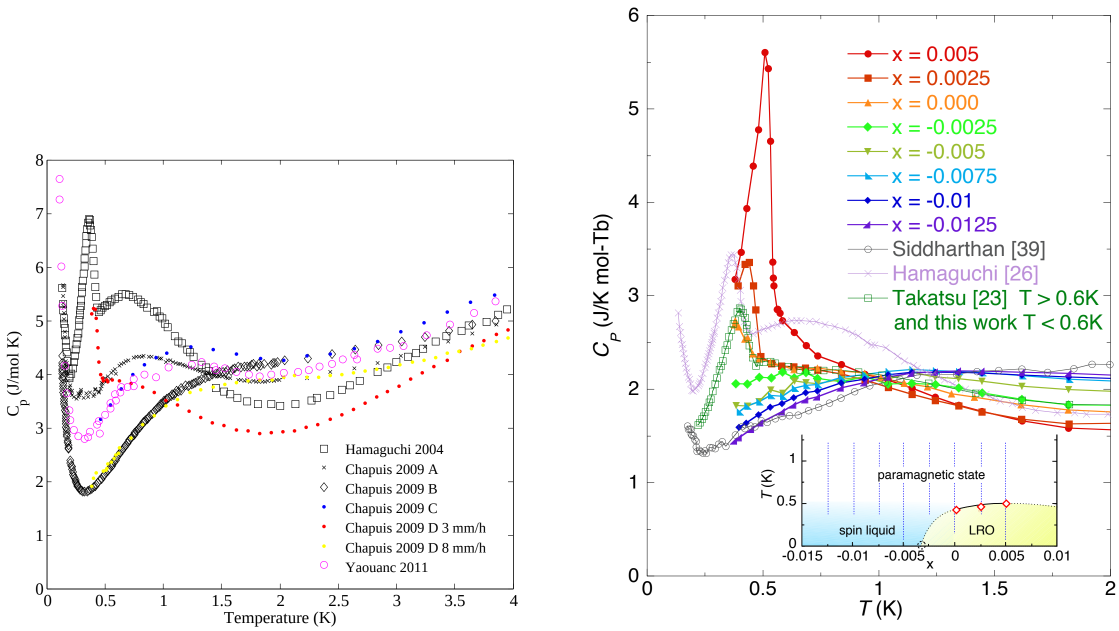

Figure 5.2: **Left:** Specific heat measurements of $Tb_2Ti_2O_7$ on single crystal samples by several different groups courtesy of L. Yaraskavich. The results show both absence and presence of a peak feature around 400 mK. A dependence on growth parameters is attributed for the differing results [48]. **Right:** Specific heat measurements of $Tb_{2+x}Ti_{2-x}O_{7+y}$ by T. Taniguchi, H. Kadowaki *et al.* [47] showing a supression and shift of a peak at 500 mK based on fine adjustments of the composition. **Inset:** Temperature versus stuffing phase diagram proposed by the group shows the formation of a LRO state or a spin liquid state based on observing a peaked feature.

X-ray scattering measurements down to 300 mK by Ruff *et al.* [49] showed a continuous broadening of Bragg peaks consistent with a cubic to tetragonal phase transition at low temperatures. The transition was not observed down to the lowest measured temperature yet an anomalous expansion of lattice parameter is observed below 20 K (Fig. 5.3). It was believed that this was coincident with the development of a spin liquid ground state.

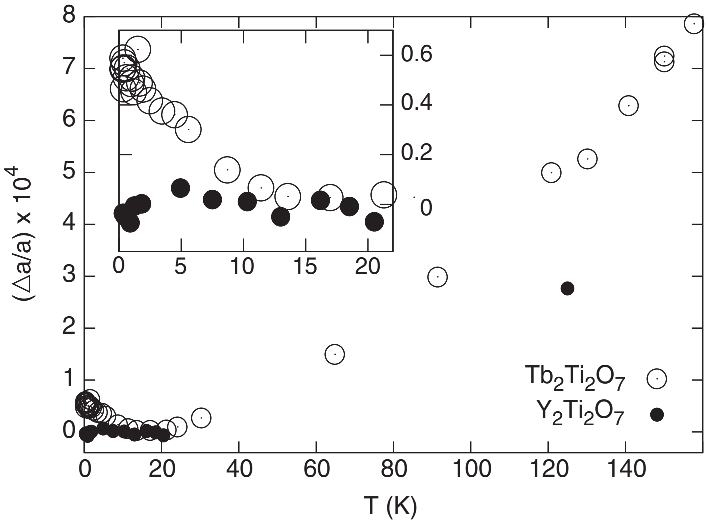

Figure 5.3: x-ray measurements of the lattice parameter versus temperature. An anomalous expansion persists down to the lowest measured temperature of 300mK [49]

Very recently, ac susceptibility measurements by Yin *et al.* [50] find evidence of a magnetic phase below 140 mK (Fig. 5.4). This peak in susceptibility may be consistent with the persistent increase of the specific heat at very low temperatures $T < 200$ mK. However, both Hamaguchi *et al.* [41] and Yaouanc *et al.*[40] attribute their $T < 200$ mK increase to the nuclear contribution to the specific heat. Confirmation of the $T < 200$ mK behaviour to be nuclear of other origins would be sufficient motivation to warrant further measurements.

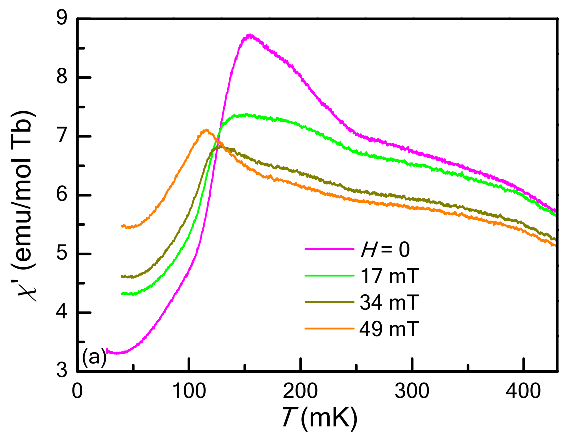

Figure 5.4: AC susceptbility measurement by Yin *et al.*[50]. The results reveal a peak at 140 mK which could indicate another phase in $Tb_2Ti_2O_7$ at lower temperatures.

Thermal expasion coefficient measurements of $Tb_2Ti_2O_7$ presented in Dunn's MSc thesis [7] found a peak at 100 mK. Tying this result into the $T < 200$ mK situation outlined above would provide further answers to the possibility of a low temperature phase. However, the quality of result must be first improved before any stronger claim can be made. In particular, the large uncertainty of the results must be addressed.

5.3 Experimental Method

The bulk sample was grown by B. Gaulin of McMaster University, Physics and Astronomy. The sample was grown by floating zone technique using Tb_2O_3 and TiO_2 as primary compounds, 2-4atm of O_2 overpressure and fed at a rate of 5-8mm/hr. Further details regarding the growth of the sample is outlined in [51]. The sample measured was cut from the bulk sample and measured 0.42 mm along the [001] axis with cross section of approximately 1.92 mm by 1.84 mm.

The thermal expansion coefficient was measured along the [001] direction using the silver dilatometer (3.2). An Oxford ^{3}He/^{4}He dilution refrigerator (Kelvinox MX400) was used for the measurements. Details regarding the refrigerator is found in Alkhesho's MSc thesis [52].

The dilatometer was attached to the mixing chamber cold plate using an oxygen free high conductivity (OFHC) copper mount. A twisted annealed silver wire extending from the cold plate to the dilatometer created a better thermal link between the sample and the mixing chamber. Thermally anchored coaxial lines were installed and used for the measurements (Appendix A).

Data was obtained using a quasi-static (QS) temperature method. In this method, temperature is held at a set value until the system reaches a steady state before data is taken. This process is repeated across the range of temperatures at desired values. The capacitance was measured using an Andeen-Hagerling 2500A capacitance bridge. The experiments were collected into two sets; DataSet 1 and DataSet 2

'DataSet 1' used 1 hour steps averaging over the last 10 minutes for $T < 120$ mK, 30 minute steps averaging over the last 5 minutes for temperatures onward to 150 mK and 6 minute steps averaging across the last 1 minute for $T > 150$ mK. 'DataSet 2' used adjusted time steps to reduce the experiment time but did not violate the steady state condition outlined above. All data was taken with increasing temperature values.

5.4 Results and Discussion

Thermal expansion coefficient results in this theses are plotted along with Dunn's results [7] (Fig. 5.5). These results are first be compared to Dunn's results followed by comparison to one another. From there, the results will be separated into the two notable features; the large peak at $T \approx$ 100-130 mK and the smaller feature at $T \approx 500$ mK. The features are finally compared to published results. An alternative scenario is presented that includes the conclusions drawn from the thermal expansion coefficient measurements.

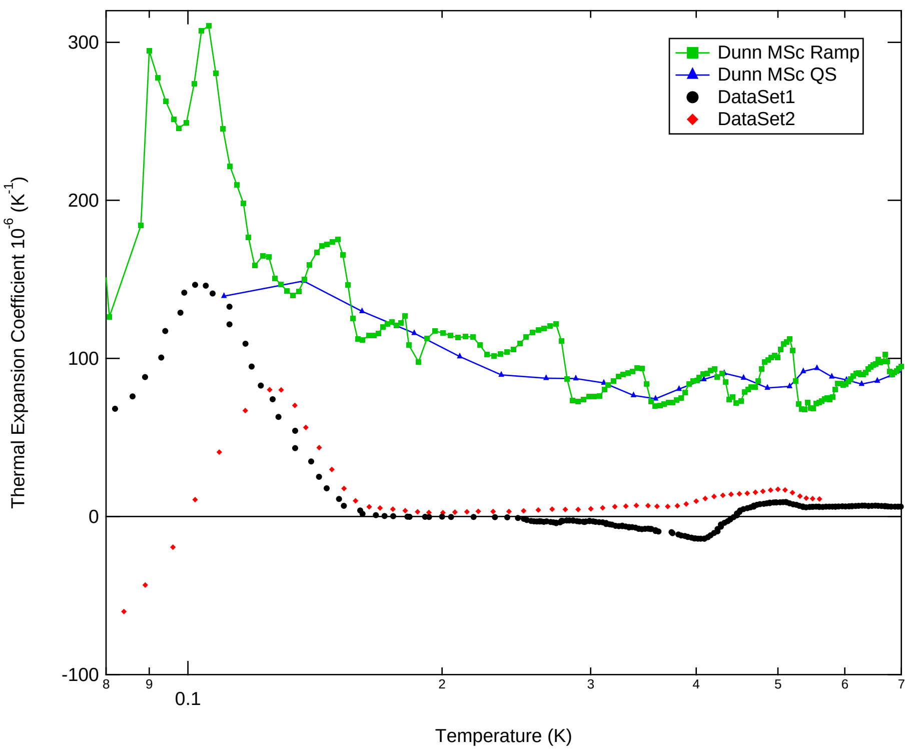

Figure 5.5: Thermal expansion measurements of $Tb_2Ti_2O_7$ compared to previous measured results. A similar 100 mK feature is observed in both results but with reduced magnitude. A new 500 mK feature is observed not previously seen due to lack of resolution.

Comparison to Dunn's MSc results

A considerable differences between the results presented in this thesis and Dunn's MSc results are observed (Fig. 5.5). Most notable is the difference between the overall magnitude if the results. The uncertainty of Dunn's MSc results are also discussed as well as the lack of a $T \approx 500$ mK feature. The differences in the result are primarily attributed to a difference in the experimental method.

A previous perturbation of the silver compact dilatometer design involved Kapton film and Stycast for electrical isolation. The results presented in Dunn's MSc used this design. Use of these materials was said to have caused issues with reproducibility attributed to their chaotic nature [7]. The use of such disordered materials could cause variances in the measured thermal expansion coefficient leading to appreciable uncertainty. Since then, these materials were replaced by sapphire in the design outlined in as per (3.2). Regardless, the differece in dilatometer design would not account for the considerable difference in magnitude between Dunn's MSc results and the ones presented in this thesis.

The replacement of the measurement lines in combination with a switch to QS temperature control have considerably improved the result resolution. The measurement lines used in the Dunn's MSc measurements were twisted pair and severely impacted the capacitance resolution (as shown in Appendix A). The change from a ramped temperature to a QS operating procedure also improved the quality of the measurement. The different temperature control results from Dunn's MSc thesis show the large jumps in thermal expansion coefficient vanish when a QS temperature procedure was adopted.

The lack of a $T \approx 500$ mK feature in Dunn's results can be argued from two perspectives. On one hand, the uncertainty of Dunn's results are sufficiently large that a feature as small as this could be hidden. On the other hand, a plausible scenario arises from a sample dependency. Although cut from the same bulk material, the sample used for Dunn's results was different from the one used for this work. If the sample compositions were different, even by slight amounts, the $T \approx 500$ mK could be suppressed. Such a conclusion was drawn from the sample dependencies seen by Chapuis' PhD results [46] and Takatsu *et al.* [39] (Fig. 5.2).

Qualitatively, the presented work corroborates the observation of a low temperature $T \approx 100$ mK feature. Furthermore, two scenarios are presented explaining the possible reasons behind the high temperature $T \approx 500$ mK feature. Quantitatively, none of the reasons provided above lead to an explanation for the large difference in the magnitude between Dunn's results and this work. The large difference remains undetermined and requires further investigation.

Comparison of DataSet 1 and 2

Comparing the results presented in this thesis against one another show several discrepancies. The difference in experimental method is discussed followed by discussion of notable features at $T \approx 100$ mK and $T \approx 500$ mK.

Investigation into the raw data rule out poor thermal equilibration as the cause for the discrepancy between the two sets. DataSet 2 is a composition of long and short duration QS measurements which were found to be in good agreement with one another. With regards to DataSet 1, the step durations used were within the long and short durations used for DataSet 2. Therefore, the use of different QS temperature lengths did not explain the discrepancy.

From a qualitative standpoint, DataSet 1 and 2 both show a low temperature $T \approx$ 100-130 mK feature. Quantitatively however, no explanation is provided to address the discrepancy of the location and magnitude nor the apparent large magnitude of the peak. Additional experiments are necessary to determine the true location and magnitude of the peak. Particular attention should be paid to the lower temperature regime as the thermal equilibration times are observed to become very long.

A very similar high temperature $T \approx 500$ mK feature is observed in both DataSet 1 and 2. However at $T \approx 400$ mK, a sizeable dip in the thermal expansion coefficient is observed only in DataSet 1. Repeated measurements of around this temperature range could not reproduce the dip. As a consequence, the dip in DataSet 1 was believed to be an anomaly present in only that set of data.

The low temperature $T \approx 100$-130 mK feature

The low temperature feature is compared to the specific heat of two groups (Fig. 5.2 Left). Hamaguchi *et al.* [41] and Yaouanc *et al.* [40] attribute the specific heat upturn to the onset of a nuclear contribution. This contribution was said to come from the hyperfine splitting of the Tb levels resulting in a Schottky profile [41]. Their nuclear contribution terms calculated were in good agreement to their own specific heat data (Fig. 5.6 inset). However, when compared to the thermal expansion coefficient results (Fig. 5.6), neither contribution provide a good match as the upturn in thermal expansion coefficient is too steep.

The feature is compared to the low temperature peak observed by Yin *et al.* [50] (Fig. 5.4). The profiles of the peaks are observed to not resemble one another. The susceptibility shows a relatively broad peak beginning at $T \approx 250$ mK and peaking at $T \approx 120$ mK while the thermal expansion coefficient reports a peak beginning at $T \approx 160$ mK.

Qualitatively, the thermal expansion coefficient results do not match a Schottky nuclear contribution to the specific heat nor to the profile observed in susceptibility measurements. It was expected that a nuclear contribution to the thermal expansion coefficient be present based on the study of $PrOs_4Sb_{12}$ by Oeschler *et al.* [53]. The study of the thermal expansion coefficient of $PrOs_4Sb_{12}$ revealed a non-negligible nuclear contribution to the thermal expansion coefficient. By extension, a non-negligible nuclear contribution in the thermal expansion coefficient of $Tb_2Ti_2O_7$ also expected.

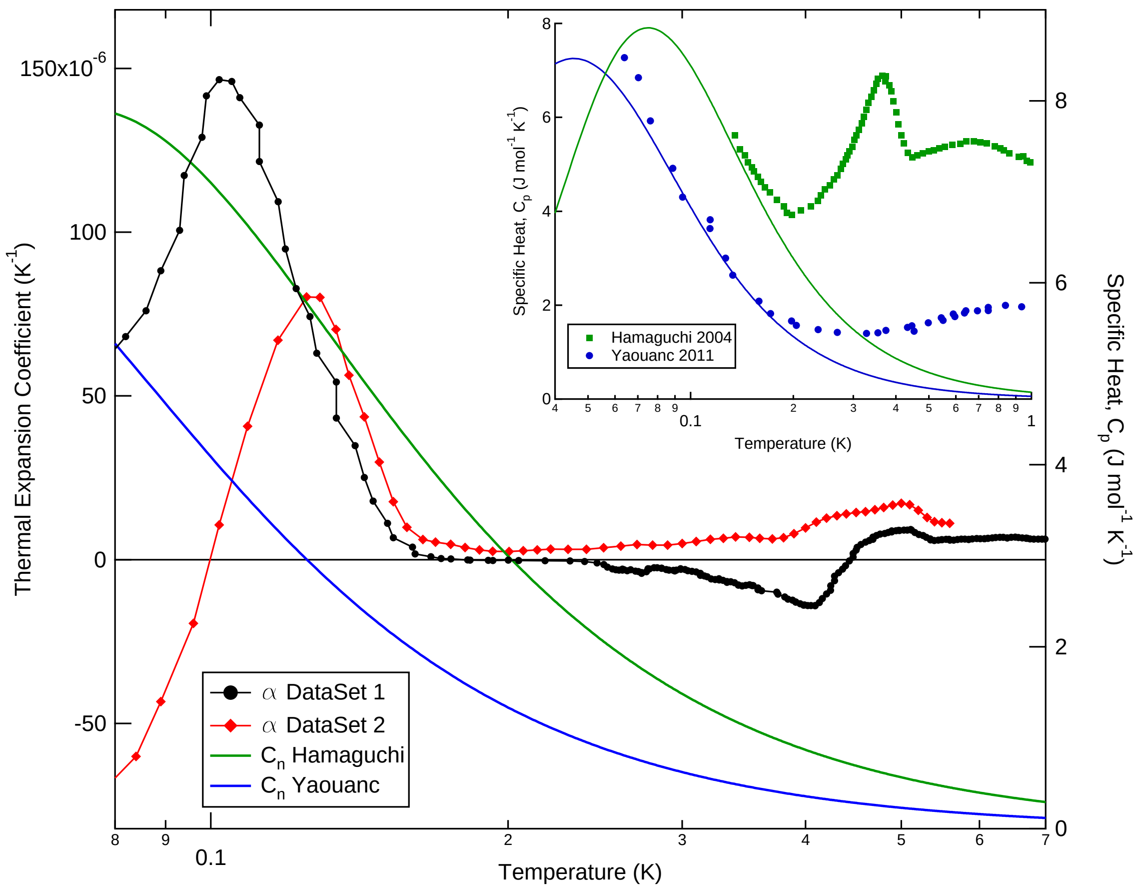

Figure 5.6: Comparison of the thermal expansion results to the nuclear contribution to specific heat described by Yaouanc *et al.* [40] and Hamaguchi *et al.* [41]. Either peak appears to be too narrow to be caused by nuclear contributions **Inset:** Plot of specific heat along with their corresponding nuclear terms.

The high temperature $T \approx 500$ mK feature

The high temperature feature of DataSet 2 is compared to the specific heat of Hamaguchi *et al.* and x-ray data by Ruff *et al.*. Qualitatively, the specific heat and thermal expansion coefficient loosely share similar features. Both features observe a more sudden upturn in value followed by a more gradual decrease in value. However, qualitatively, the two features are separated by $\Delta T \approx 100$ mK. The shift in peak between the two results can possibly be explained by the research of Taniguchi, Kadowaki *et al.* [47] (Fig. 5.2 Right).

Their results show a shift in the peak position from adjustment of the stuffing factor x.

The results show a peak shifting from $T \approx 375$ mK to $T \approx 500$ mK; a temperature of $\Delta T \approx 125$ mK. Although a direct composition comparison between the sample used Hamaguchi *et al.* and this work's sample is not made, a possible reason to the observed shift in peak location is attributed to this.

A thermal expansion coefficient is computed from the x-ray diffraction data by Ruff *et al.* [49] and is compared to this work. The x-ray data was differentiated with central differences. Although the point density of the x-ray data is lacking, the results show now evidence of a peak at $T \approx 500$ mK.

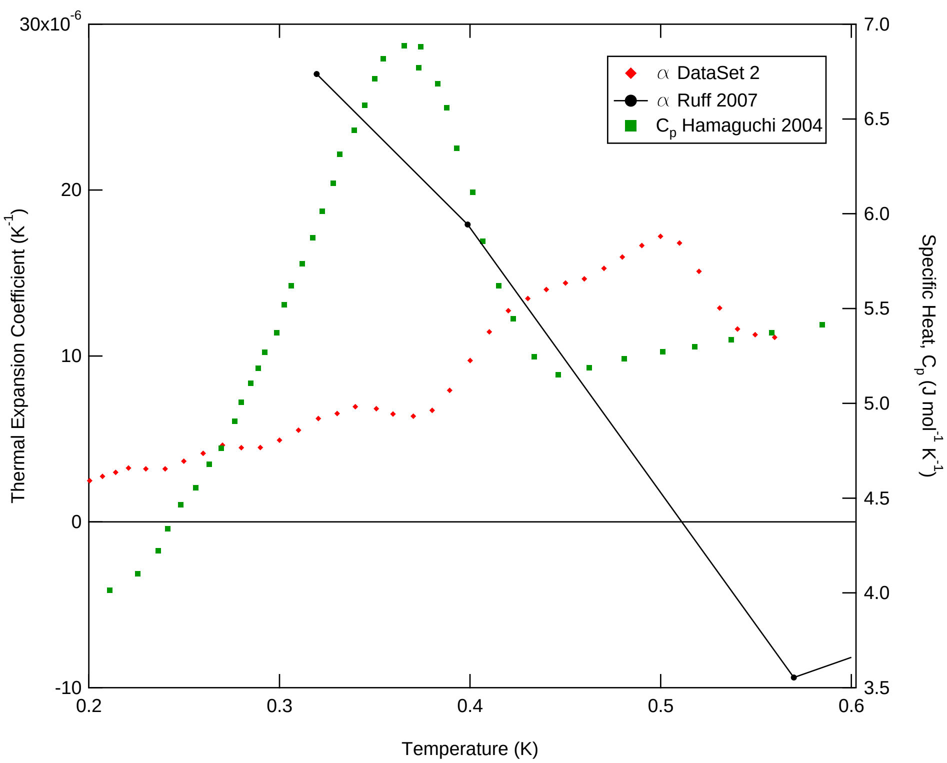

Figure 5.7:

5.5 Conclusion

The thermal expansion coefficient results presented in work show two notable features observed for this sample of $Tb_2Ti_2O_7$. The low temperature $T \approx$ 100-130 mK feature is too steep to match the profile of a nuclear Schottky contribution in specific heat nor to the peak observed in susceptibility measurements. It is expected that a nuclear contribution to be observed in the thermal expansion coefficient yet the profile of the low temperature feature does not match the specific heat profile. Further investigation into the low temperature feature is necessary to reconcile this discrepancy. The high temperature $T \approx 500$ mK vaguely resembles the specific heat results by Hamaguchi *et al.* [41]. A shift in peak location between the two results is observed but not entirely unexpected based on results by Taniguchi, Kadowaki *et al.* [47].

Susceptibility results presented by Yin *et al.* [50] can offer two different scenario depending on the results are interpreted. In one scenario, the peak in susceptibility can be interpreted as results for a sample whose stuffing factor x is very close to the spin liquid dominated ground state region (as per Fig. 5.2 Right Inset). In the other scenario, the susceptibility results could indicate the sample exhibits spin liquid behaviour but enters an entirely new phase at much lower temperature.

By extension, two possible outcomes to the thermal expansion coefficient results are put forth. If the first scenario is true, the sample studied in this work would be said to form LRO due to the observation of a $T \approx 500$ mK peak. The low temperature feature, with further research, could be reasoned as a nuclear contribution to the thermal expansion coefficient.

If the second scenario were true, the thermal expansion coefficient results would be the LRO equivalent to the susceptibility results. That is, the $T \approx 500$ mK peak would once again indicate the formation of LRO but enters the prospective new phase at lower temperatures. The consequence of this scenario would be a lower temperature phase weakly dependent on sample stuffing. This proposition is completely speculative and is based solely on interpretation of the measurement results of $Tb_2Ti_2O_7$.

Chapter 6

$Ba_3NbFe_3Si_2O_{14}$

The complex material $Ba_3NbFe_3Si_2O_{14}$ is measured using the fused quartz dilatometer along several crystallographic axes. This material has been found to have a magnetoelectric (ME) multiferroic phase below $T_N \approx 26$ K. The origin of this phase is not completely known but is believed to be of similar origin to other ME multiferroic materials.

In this chapter, ME multiferroic materials are described and differences between preceding ME multiferroic materials are discussed. The emergence of the ME multiferroic phase is discussed from a phenomenological macroscopic perspective based on other ME multiferroic materials. The thermal expansion and thermal expansion coefficient above T_N is measured in search for a displacive structural phase transition. The thermal expansion coefficient results are compared to specific heat measurements and thermal expansion results are compared to x-ray lattice measurements.

6.1 Introduction

Multiferroism describes a phase where more than one of ferromagnetism, ferroelectricity or ferroelasticity simultaneously exists [54]. Ferroic ordering can be described using the order parameter from Landau Theory. The order parameter is a measure of how ordered a state is. A completely disordered state has an order parameter of zero while an ordered state a non-zero order parameter. It is then possible to distinguish ferroic ordered phases from non-ordered phases by the order parameter. For example, a magnetic system can be described by the order parameter magnetization. A non-zero magnetization would indicate the magnetic system is in the ferromagnetic phase while zero magnetization (in general) would indicate the system to be in a paramagnetic phase. In ferroic ordered systems, there is a specific externally applied source that can reorient the order parameter. Applying this to the example above, the magnetization can be reoriented from the application of an external magnetic field. This ability is crucial in controlling the ferroic phase of materials and have led to development of devices such as hard disc drives.

In multiferroic materials, the ability to alter the order parameter of each ferroic order can be achieved by any of the external controls [55]. For example a ferromagnetic-ferroelectric multiferroic's magnetic order can be altered through application of external electric field and likewise electric polarization through external magnetic field. The incorporation of multiferroic materials into current technology could lead to storage media capable of retaining information in forms beyond just magnetic storage. Other possibilities for these materials could be multifunctional hybrid sensors or switches.

This study focuses specifically on magnetoelectric (ME) multiferroic materials; ones which simultaneously contain magnetic and electric ordering. A brief history of ME multiferroic materials is presented discussions the series of developments which brought about the current status of ME multiferroic materials.

Boracites

The first ME multiferroic discovered was nickel iodine boracite ($Ni_3B_7O_{13}I$) showing ferroelectricity and weak ferromagnetism below 64 K [54, 56]. Below the critical temperature, the material showed dielectric hysteresis and magnetic hysteresis the presence of both indicative of a multiferroic. The material was expected to be ferroelectric based on other paramagnetic boracites but also expected to be ferromagnetic at sufficiently low temperatures from 3*d* linked metal-halogen-metal chains. Referred to this as the 'Rochelle Salt' of multiferroics, nickel iodine boracite shows proof of concept but the complex structure prevented extracting the contributing factors to multiferroticity within the material[54].

Perovskites

The perovskite structure is described as $A^{2+}B^{4+}X_3^{2-}$ where the element X is typically face centered oxygen. Perovskite materials in general were found to be rich in ferroic ordering including some that exhibited ME multiferroic phases.

Conventional ferroelectric perovskites were found to obtain non-centrosymmetry by an off-center displacement of the B site cation [54]. Ferroelectric perovskites however undergo a d-type Jahn-Teller distortion consequence of the presence of *d* orbital magnetic spins on the B site cation. The preference of the Jahn-Teller distortion, a symmetric distortion, was attributed to having a lower driving force over the off-center displacement [54]. Based on these outcomes, it was predicted that a ME phase could not exist in perovskite materials. Since a magnetic perovskite requires partially filled *d* orbitals, it would indicate a strong inclination to undergo a Jahn-Teller distortion instead of the symmetry breaking shift necessary for electric polarization. This was indeed the case seen by $LaMnO_3$ [57] and $YTiO_3$ [58] having d^3 and d^1 electron configurations on the B site cation (Mn^{3+} and Ti^{3+}) respectively that showed no evidence of electric ordering.

However, hexagonal structured manganite perovskites such as (hexagonal) $YMnO_3$, were found to favour the non-centrosymmetric shift over the Jahn-Teller distortion despite having d orbital occupation. Indeed in hexagonal $YMnO_3$, a shift from $P6_3/mmc$ to a $P6_3cm$ structure by Raman and infrared spectra measurements [59]. This result was said to be from the crystal field producing and ordering of d states that leaves the d_{z^2} mostly empty. This emptiness would then satisfy the empty d orbital requirement of the non-centrosymmetric shift permitting ferroelectricity along the c-axis [60]. As for the magnetic order, an antiferromagnetic ordering is present in manganites by super-exchange between adjacent Mn^{3+} ions [60]. By all accounts, $YMnO_3$ was determined to be an antiferromagnetic ordered ME multiferroic material [61].

Langasites

The langasite type compounds follow the complex structure of $A_3BC_3D_2O_{14}$. Similar to the perovskite type materials, the various langasite materials span a vast assortment of ferroic properties. In particular, $La_3Ga_5SiO_{14}$ is known for its piezoelectric and nonlinear opitical properties related to the non-centrosymmetric nature [62]. In a similar way to perovskite materials, langasites were believed to be good candidates for the next ME multiferroic material.

The langasite structure is quite complex due to the many different cations present in the composition. The structure belongs to the trigonal non-centrosymmetric P321 space group [63]. The crystal structure can be broken down into two alternating cationic sublattices (Fig. 6.1 Left) [62]. The first layer (z = 0) is formed by a decahedral A and octahedral B site while the second layer (z = 1/2) is comprised of tetrahedral C and D sites.

The material $Ba_3NbFe_3Si_2O_{14}$ is one of the several C = Fe langasites studied which are found to exhibit ME multiferroticity. Of the cations present, the Fe^{3+} is the only magnetic contributor forming a network of isolated triangular units in the ab plane (Fig. 6.1 Right) [64]. Néel temperatures of known iron langasites range between 24-36K; $Ba_3NbFe_3Si_2O_{14}$ in particular has $T_N \approx 26$ K. Along the c (labelled z) direction, $NbFe_3O_{12}$ chains are formed from FeO_4 tetrahedra and NbO_6 polyhedra which are a similar arrangement to the rare earth cation and Mn in hexagonal perovskites [63]. Based the structure being of similar resemblance to manganites, the mechanism which promoted the multiferroic phase in langasites was believed to be similar to the manganites [63]. That is, a non-centrosymmetric shift in the structure is postulated to be the driving mechanism that promotes the formation of the multiferroic phase in langasites. A study of the thermal expansion coefficient of $Ba_3NbFe_3Si_2O_{14}$ is done to reveal any evidence of a structural transition to support the hypothesis.

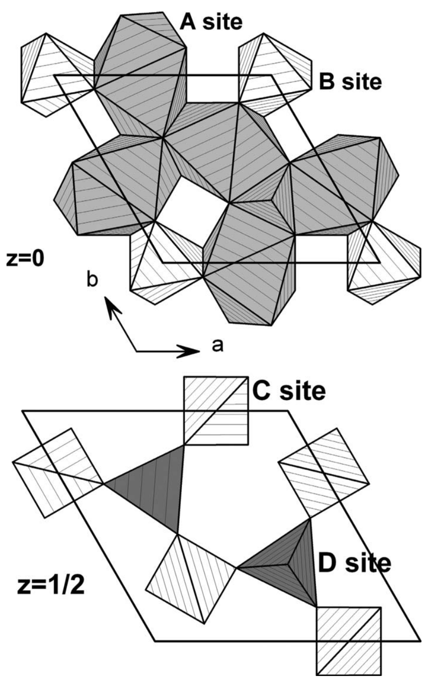

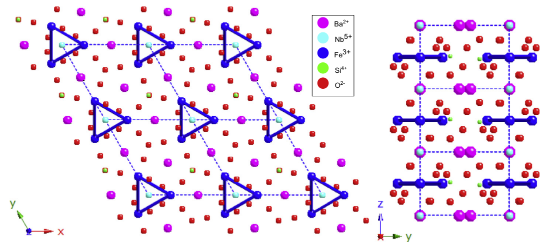

Figure 6.1: **Left:** The layered structure of langasite type materials contain a complex arrangement of cations [62]. **Right:** The crystal structure of $Ba_3NbFe_3Si_2O_{14}$ shows isolated an isolated triangular sublattice upon which the Fe^{3+} ions sit [64].

6.2 Background and Recent Measurements

Magnetization measurements (Fig. 6.2) of $Ba_3NbFe_3Si_2O_{14}$ by Marty *et al.* [64] between 2-300 K with magnetic fields up to 10T applied perpendicular and parallel to the c-axis reveal a cusp at $T_N \approx 27$ K in the associated susceptibility indicated a transition to magnetic order. Fitting the magnetic susceptibility (above 100K) to the Curie-Weiss law ($\chi = C/(T-\theta)$), they found a Curie temperature of $\theta = -174 \pm 4$ K and Curie constant $C = 5.92\mu_B$ of the Fe^{3+} ion.

Neutron diffraction measurements on powder samples revealed the emergence of magnetic Bragg peaks below T_N. The magnetic moments were suggested to point along the ab plane with each moment 120° degrees from each other. The arrangement of moments from plane to plane are suggested to form a helix with period of approximately 7 lattice parameter. The helical structure raises questions regarding the dielectric properties of the material.

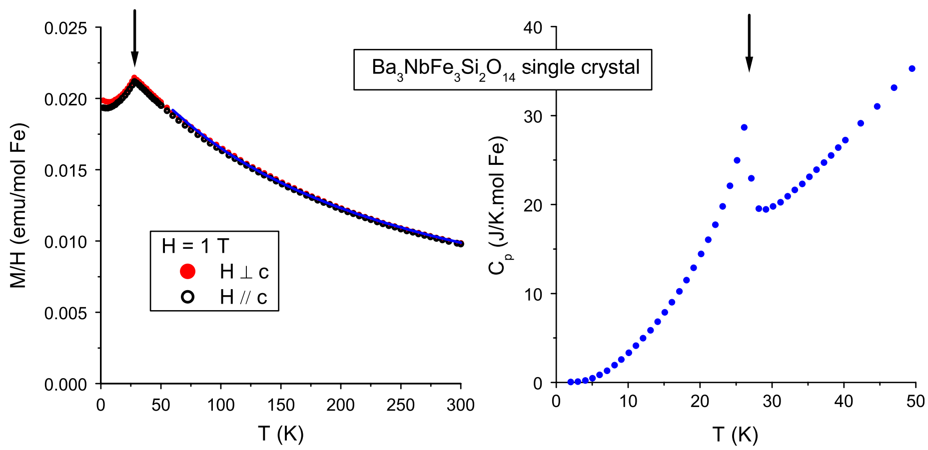

Figure 6.2: DC susceptibility and specific heat measurements by Marty *et al.* [64] reveal a magnetic ordering at $T_N \approx 27$ K.

Further studies have mapped specific heat and thermal conductivity from 2-200 K confirming a λ peak at 26 K (Fig. 6.3). ^{93}Nb NMR experiments on single crystal samples show a broad spectrum below T_N suggestive of many different Nb sites experiencing different internal magnetic fields. Dielectric constant and electric polarization with electric field along the c direction measurements show a broad drop beginning at 30 K and polarization increase at 24 K. Furthermore, polarization-electric field hysteresis measurements at 40 K and 10 K reveal the development of a hysteresis loop showing spontaneous polarization development below T_N

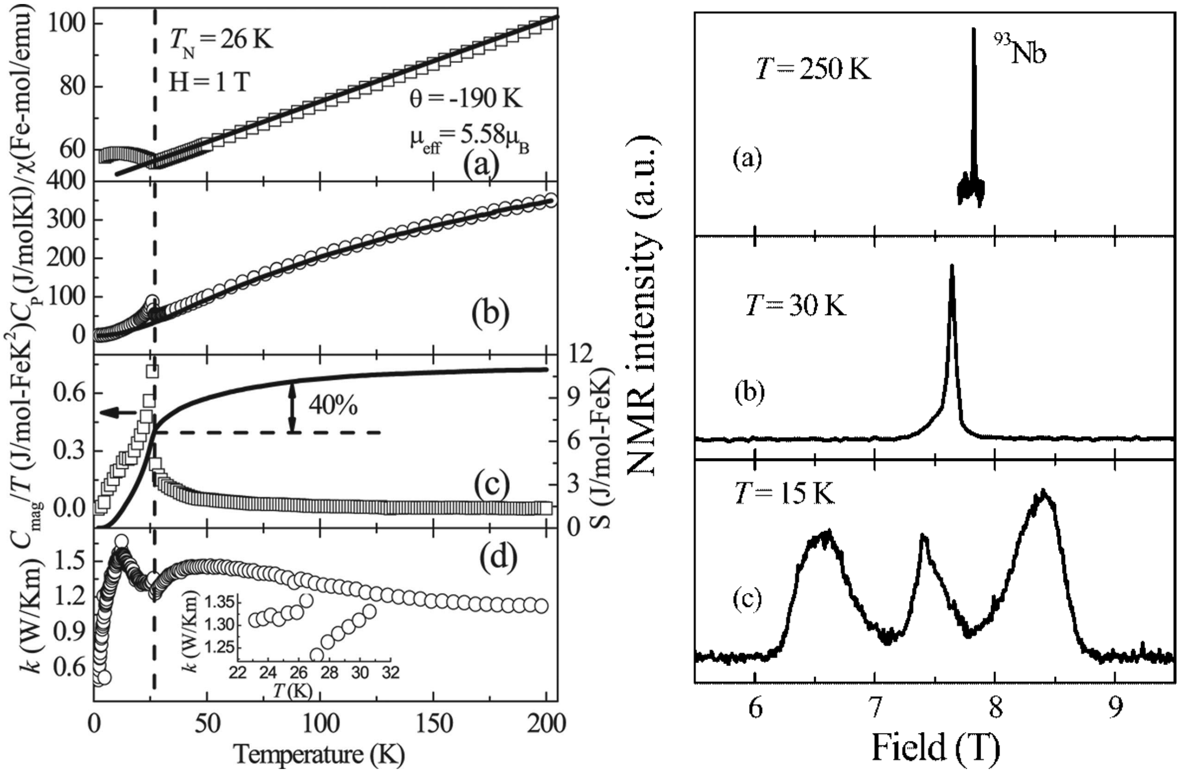

Figure 6.3: **Left:** DC susceptibility, specific heat and thermal conductivity measurements up to 200 K by Zhou *et al.* [63]. **Right:** NMR measurements by Zhou *et al.* [63] on ^{93}Nb at 250 K (a), 30K(b) and 15 K (c) show the development of a broad spectrum believed to be due to different internal magnetic fields on the NB sites.

In hexagonal manganites, the ME multiferroic phase was due to the displacement of the cation along the c-axis. In a similar fashion, it was believed that a possible bulking or tilting of the NbO_6 octahedra along the c-axis could be the reason for the entrance into the multiferroic phase [63]. X-ray diffraction powder measurements down to 10 K show no structural change from room temperature (Fig. 6.4 Right). However the temperature point density, particularly above 75 K may not be sufficiently high enough to observe a structural transition which may occur relatively abruptly in temperature. The profile of an unobserved displacive structural phase transition would have to be sharper than a width of 10 K and be smaller in size than the difference between points. The structural phase transition lattice shift would need to be approximately on the order of 0.001Å or smaller.

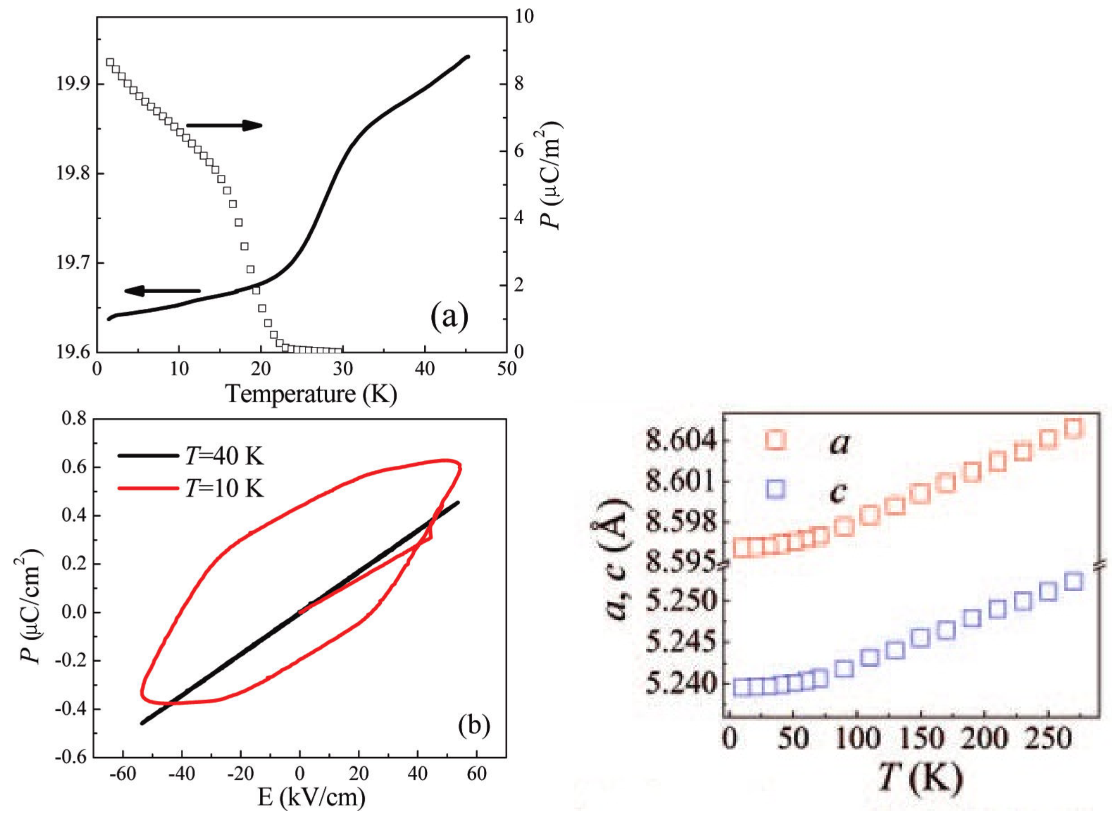

Figure 6.4: **Left:** Dielectric constant (solid line) and electric polarization (open squares) results by Zhou *et al.* [63] show a broad drop at 30 K associated with the transition into the ME phase. Electric polarization - electric field phase diagram show a hysteresis loop forming at 10 K but absent at 40 K. **Right:** X-ray measurements by Zhou *et al.* [63]. The low point density may overlook a potential structural transition

6.3 Experimental Method

The sample was grown by H.D. Zhou and C. R. Wiebe of Florida State University, Department of Physics. The sample was grown by travel-solvent floating-zone technique using $BaCO_3$, Nb_2O_5, Fe_2O_3 and SiO_2 as compounds. Further details of the grown of the sample is covered in [63]. The sample used for the following thermal expansion coefficient measurements measured 1.95 mm along the c-axis, 1.06 mm along the a-axis and 1.37 mm along the off-axis.

Due to the large temperature range, experiments were performed using two different cryogenic liquids: liquid ^{4}He and liquid N_2. Measurements between 20-100 K used liquid ^{4}He while measurements above 80 K used liquid N_2. A crossover temperature range of 20 K between the two cryogenic liquids allow for the combining of results between the two.

Initial measurements were performed using the silver dilatometer at liquid ^{4}He temperatures. A large negative thermal expansion coefficient along the a-axis was observed. It was believed that the large cell effect of the silver dilatometer overshadowed the thermal expansion coefficient of the material. The quartz dilatometer was used to address this potential problem. Additionally, it was recognized that the thermal expansion coefficient of silver across the full temperature changes substantially (Fig. 3.5) leading to a cell effect which could change substantially across the temperature range. All measurements after the first measurements used the fused quartz dilatometer.

Both ramped and QS temperature control modes were used during the measurement of the material. At first DT methods were used to perform quick scans at a rate of 0.1 K/min across large temperature ranges but were later found to be in good agreement with QS results. QS temperature steps varied from 30 minutes to 2 hours.

The same pumped ^{4}He cryostat used for $LiHoF_4$ (section 4.3) was used to make all the measurements on $Ba_3NbFe_3Si_2O_{14}$. When liquid ^{4}He was used, the cryostat was operated under regular routines. However, for liquid N_2 temperatures, the 1K pot was closed from the main bath, evacuated and then closed.

6.4 Results and Discussion

Results of of each axis are discussed individually. The thermal expansion coefficient result on each axis is compared to the specific heat results by Zhou *et al.* [63]. Thermal expansion results are plotted with X-ray data from the same group which is converted into a thermal expansion. X-ray data is converted to thermal expansion by extracting values from the plot (Fig. 6.4 Right), taking the difference of value from T = 20 K and dividing by the crystallographic lattice parameter value at room temperature from Table 1 in [63]. They are $c_0 = 5.2523(3)$Å and $a_0 = 8.6049(2)$Å [63]. An error of 5% was taken based on uncertainty from extracting values from a very small image.

The profile of a displacive structural phase transition is taken from the study of the perovskite $SrTiO_3$ by Willemsen *et al.* [65]. The thermal expansion coefficient results (Fig. 6.5) show a steep increase from a relatively constant thermal expansion coefficient. The thermal expansion coefficient results of $Ba_3NbFe_3Si_2O_{14}$ are qualitatively compared the displacive structural phase transition in $SrTiO_3$.

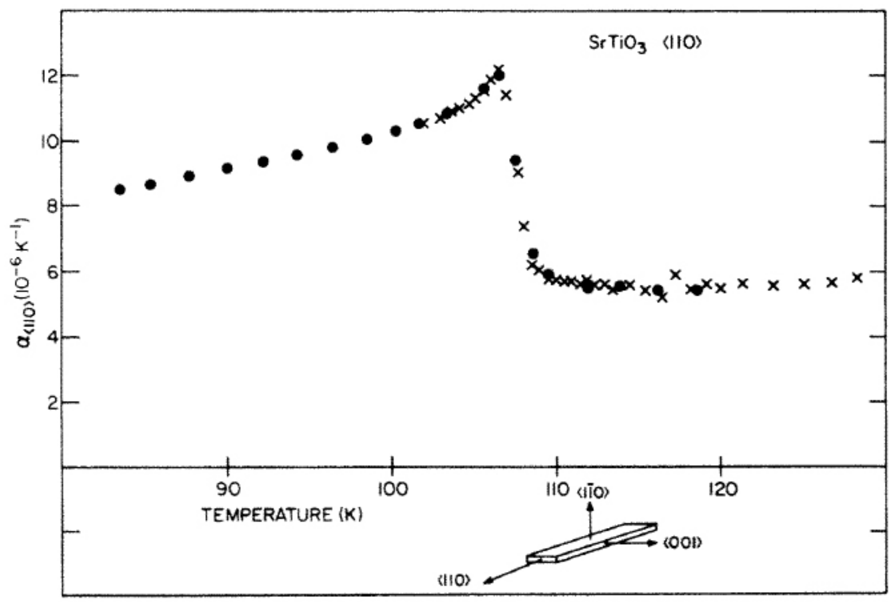

Figure 6.5: Displacive structural phase transision of $SrTiO_3$ from Willemsen *et al.* [65]. The profile is used to compare to the measured results of $Ba_3NbFe_3Si_2O_{14}$. The dots and crosses represent different runs on the same crystal.

C-Axis Results

The ME multiferroic phase transition was first measured to ensure a reasonable signal was obtained. Thermal expansion coefficient results from the silver dilatometer and fused quartz dilatometer at low temperature show good agreement with each other (Fig. 6.6 Inset) having a peak at $T = 26.8$ K. However, a smaller secondary peak is resolved in the fused quartz dilatometer thermal expansion coefficient results. This smaller peak coincides with the peak observed in the specific heat results measuring $T_N = 25.9$ K. The larger peak is compared to the displacive structural phase transition of $SrTiO_3$ (Fig. 6.7). The steepness of the two features are identical leading to the possibility that the larger peak is a displacive structural phase transition.

A considerable difference in profile between thermal expansion coefficient and specific heat past above the low temperature feature is observed. However, if the primary contributions to the specific heat (at this temperature) are taken to be lattice and magnetic contribution, recalling the discussion (end of section 2.3) of the Grüneisen parameter with multiple contributing terms, each specific heat term would have a corresponding thermal expansion coefficient with their own Grüneisen parameter. Therefore, the difference in profile can be explained by different Grüneisen parameter values for each contribution.

Thermal expansion coefficient values in the overlap region show a gap $\approx 2 \times 10^{-6}$ in size. The overall profiles between the two appear to match. This region must be remeasured to reconcile the bizarre gap between the two sets of results. As a consequence of this gap, the thermal expansion results (Fig. 6.10) do not transition very well. The lowest thermal expansion point for the liquid N_2 result is matched with the corresponding value on the liquid ^{4}He side. This in general is not an acceptable approach and require the gap to be reconciled to have proper closure on the subject.

An anomalous feature at $T \approx 230$ K is observed in the measurement of the thermal expansion coefficient. Similar features were observed previously in the silver compact dilatometer during the joint study with J. Akeyr (see section 3.2). These features were originally attributed to glass-like transitions in epoxies but such epoxies have not been used since. However, it is a possibility some residual epoxy was left on the sample from previous experiments. If however this feature is material driven, it has not previously been measured through other methods. Further investigation with particular detail to the cleanliness of the sample and device should address this discrepancy.

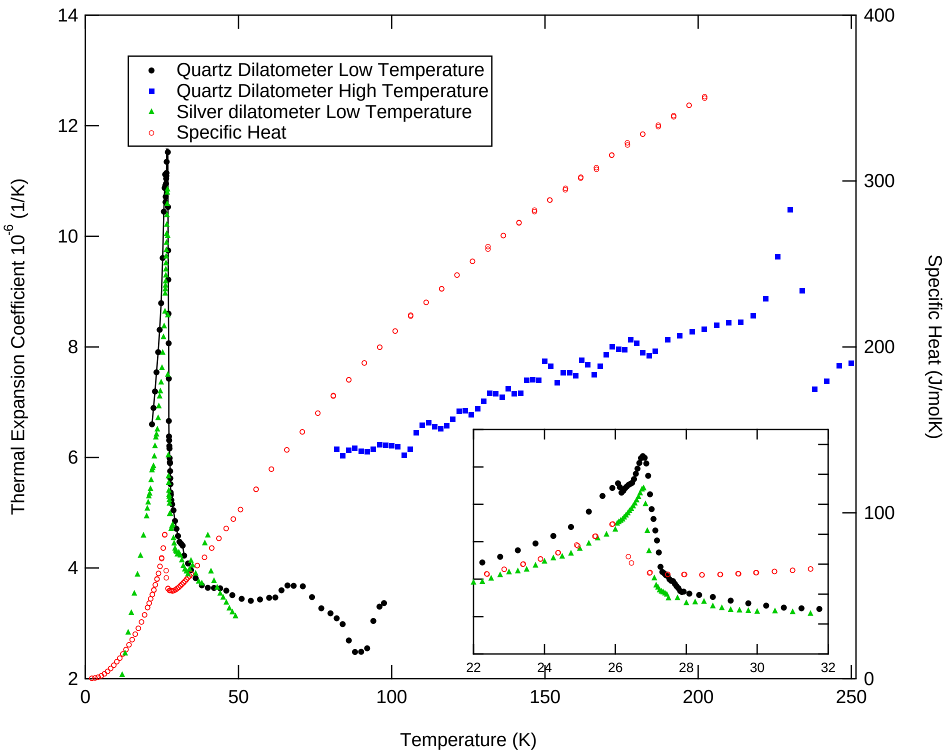

Figure 6.6: Thermal expansion coefficient results along the c-axis find $T_N \approx 26.8$ K. **Inset:** Focused plot on the magnetic phase transition at low temperatures

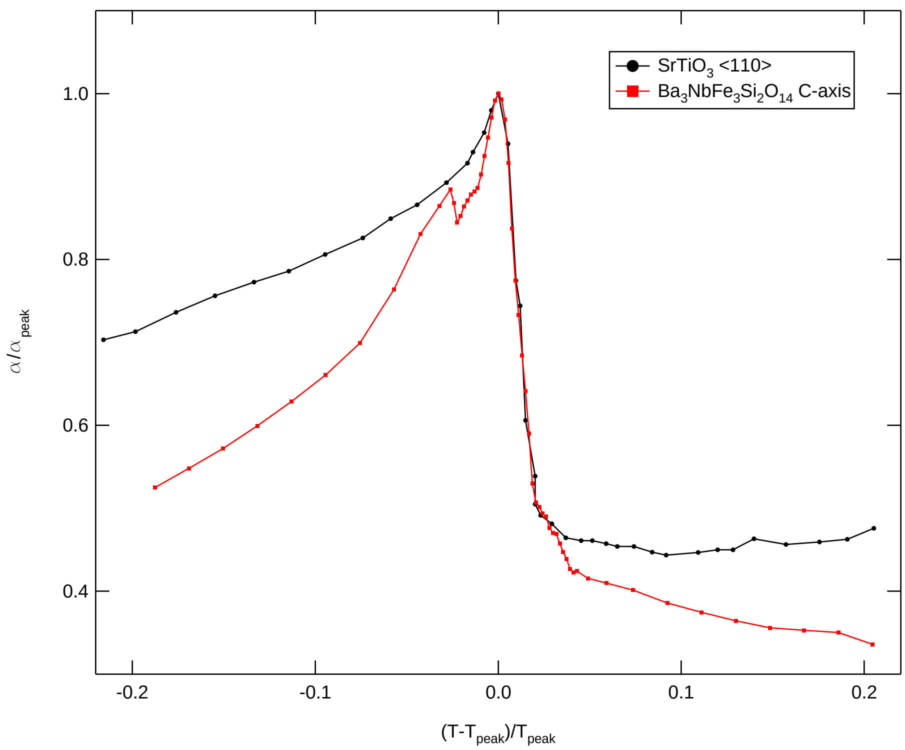

Figure 6.7: Normalized thermal expansion coefficient results plotted against normalized temperature of $SrTiO_3$ and $Ba_3NbFe_3Si_2O_{14}$ shows good agreement between the two peaks. The results indicate that the large peak observed in $Ba_3NbFe_3Si_2O_{14}$ is a displacive structural phase transition

The thermal expansion and x-ray data (Fig. 6.8) agree with each other for $T < 80$ K but appear to diverge quickly at greater temperatures. If the cell effect contribution from high temperature were factored in, it would only contribute a maximum of approximately 2×10^{-6} to the slope of the thermal expansion. A much larger contribution would be required to account for this discrepancy. The thermal expansion results show a hump at low temperatures coincident with the features observed in the thermal expansion coefficient. If the larger peak in the thermal expansion coefficient satisfies the requirement of being sharper than 10 K and smaller than the difference between x-ray data points.

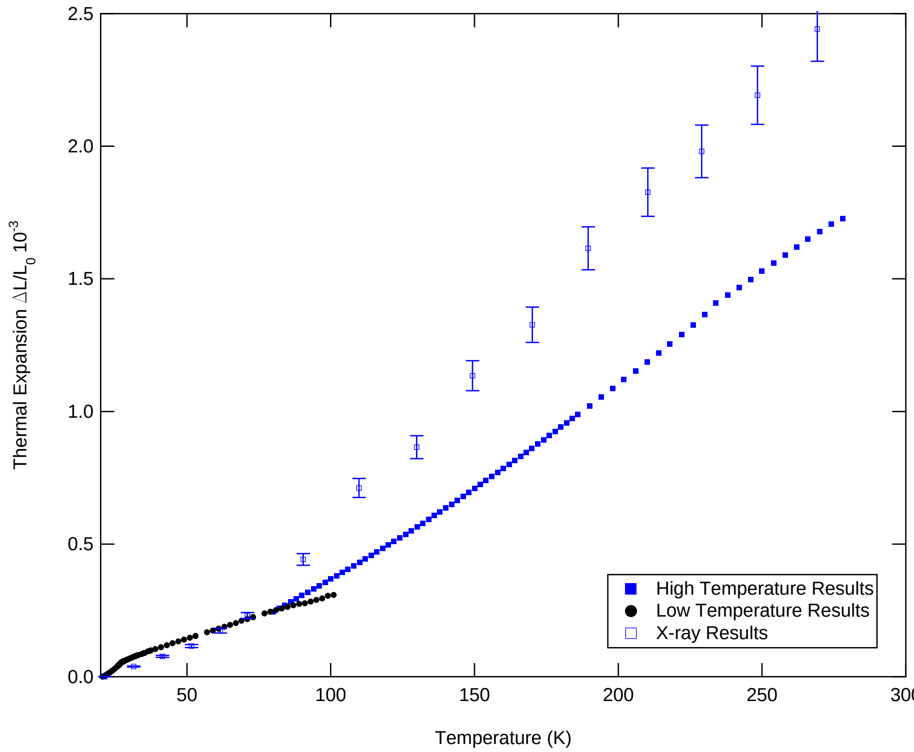

Figure 6.8: Thermal expansion results compared to the calculated x-ray thermal expansion values show good agreement at low temperature but diverging results at higher temperatures

To summarize the c-axis, the thermal expansion coefficient measurements of the fused quartz dilatometer find $T_N \approx 25.9$ K coincident with the specific heat T_N, a peak at $T = 26.8$ K believed to be the displacive structural phase transition, and an anomalous feature at $T \approx 230$ K. The anomalous feature, believed to be systematic in nature requires additional study to determine its origin. The thermal expansion coefficient measurements in the crossover region from liquid ^{4}He to liquid N_2 temperatures are to be repeated to address the large gap between the two results.

A-Axis Results

Measurement along the a-axis using the silver compact dilatometer (Fig. 6.9) revealed a considerably large negative thermal expansion coefficient that showed no sign of becoming positive. The large negative thermal expansion coefficient of the silver dilatometer is attributed to a large cell effect outlined in section 3.2. The absence of a T_N peak could have been from an dominating cell effect contribution overshadowing a possibly small peak in the *a*-axis. As a result, the fused quartz dilatometer was used to make further measurements.

Fused quartz dilatometer measurements show the thermal expansion coefficient remains net negative but are considerably smaller in magnitude measuring approximately 3×10^{-6}. If the experimental cell effect of the quartz dilatometer were assumed to remain at the same magnitude from higher temperatures, the measured results and cell effect would be on the same order of magnitude. If fluctuations in of the cell effect are also assumed to extend to lower temperatures, features of equal or smaller magnitude could still be obscured; a plausible explanation to the absence of a T_N peak.

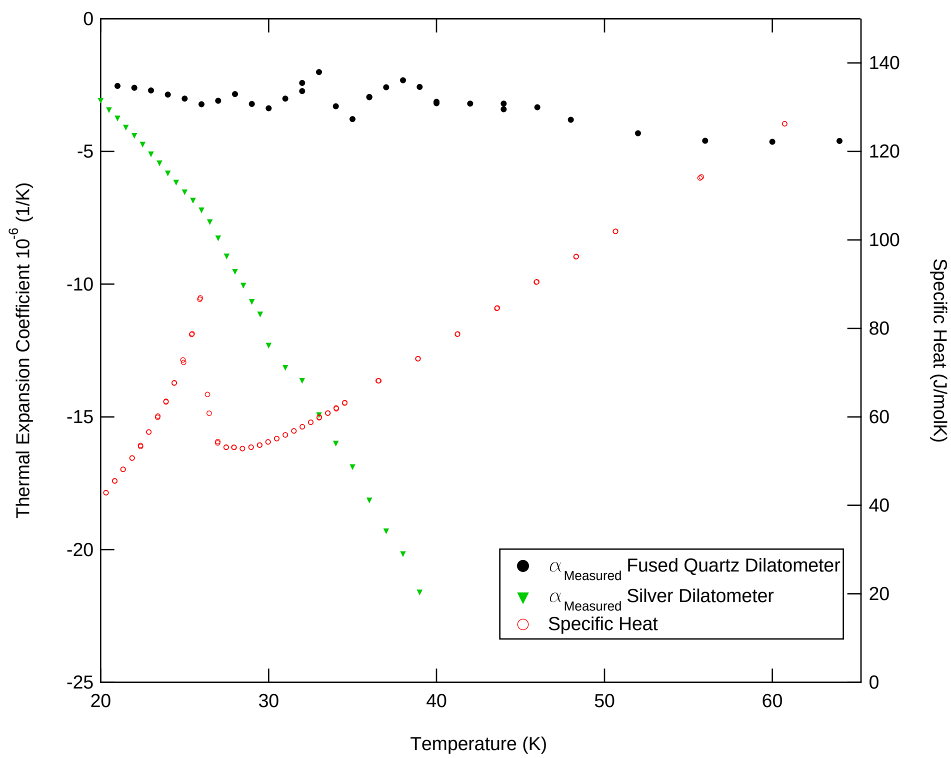

Figure 6.9: Thermal expansion coefficient results along the a-axis reveal values on the same order of magnitude as the cell effect resulting in an incapability of observing features. Previous silver thermal expansion coefficient results show a very negative thermal expansion coefficient.

As expected from the thermal expansion coefficient results, the measured thermal expansion shows a negative growth at increasing temperatures. When plotted against the x-ray derived thermal expansion (Fig. 6.10), even when considering a cell effect contribution of approximately (2×10^{-6}), the resulting slope still remains be insufficiently large to match the results. A cell effect magnitude of approximately 3.5×10^{-6} would be necessary to match the two results. However, if one assumes a generally featureless decreasing magnitude cell effect (based on the theoretical derivation), an increase in thermal expansion coefficient is not expected. A proper discussion and measure of the quantitative thermal expansion requires knowledge of the experimental cell effect at these temperatures.

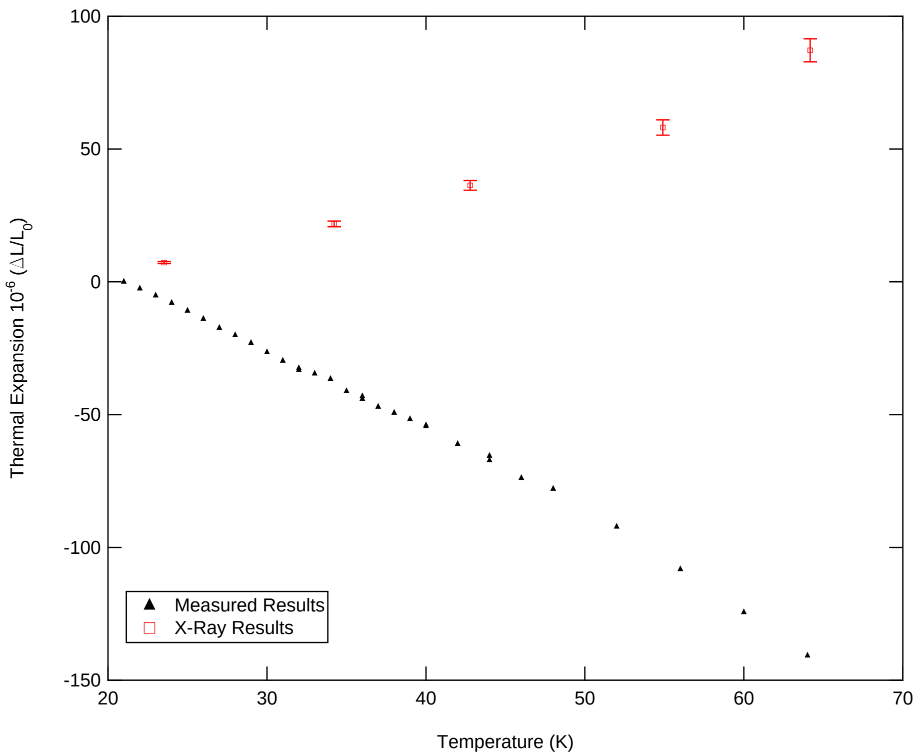

Figure 6.10: Thermal expansion results along the a-axis expectedly reflect the negatively measured thermal expansion coefficient. By extension, the thermal expansion results are similarly inconclusive to the presence of a structural shift in the lattice along the a-axis.

A-axis measurements at liquid N_2 temperatures and above are not measured. In some sense, better low temperature results are more important than higher temperature results.

Without an measure of the T_N peak, any potential feature observed could be argued as fluctuations in the cell effect. Therefore, the measurement of the thermal expansion coefficient along the a-axis do not provide conclusive evidence for evidence of a structural change.

Off-Axis Results

Low temperature thermal expansion coefficient measurements along the off-axis (Fig. 6.11 Inset) revealed a sharp minima at $T \approx 26.9$ K coincident with the displacive structural phase transition peak measured along the c-axis. Likewise, a smaller peak at slightly lower temperature is observed which, adopting the same logic as the c-axis results, would be the T_N peak. The results show a net negative thermal expansion coefficient. Unlike the a-axis results, the order of magnitude exceeds the experimental cell effect. The overall profile shows an increasingly negative thermal expansion coefficient until $T \approx 230$ K. This feature is likely the same one observed along the c-axis and was discussed previously.

A similar difference approximately 2×10^{-6} in thermal expansion coefficient in the overlap region is observed. Similar to the c-axis overlap region, the overall profile appears to be preserved.

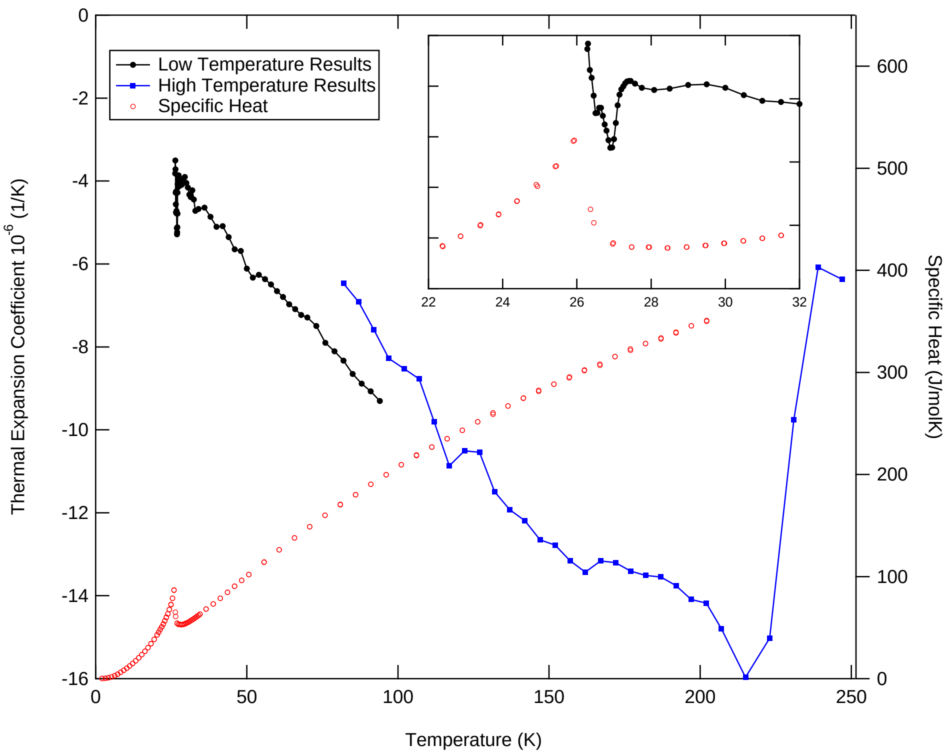

Figure 6.11: Thermal expansion coefficient results along the off-axis find $T_N \approx 26.9$ K. **Inset:** Focused plot on the magnetic phase transition at low temperatures

Thermal expansion measured along the off-axis (Fig. 6.12) are once again expectedly decreasing with increasing temperature. Although there is no off-axis thermal expansion x-ray data, using the same standards as the other axes, the same conclusion is drawn. That is, the displacive structural phase transition satisfies the condition of being sharper than 10 K and smaller than the difference between x-ray data points. It is once again noted that the kink at $T \approx 230$ K is the anomalous feature observed in the thermal expansion coefficient.

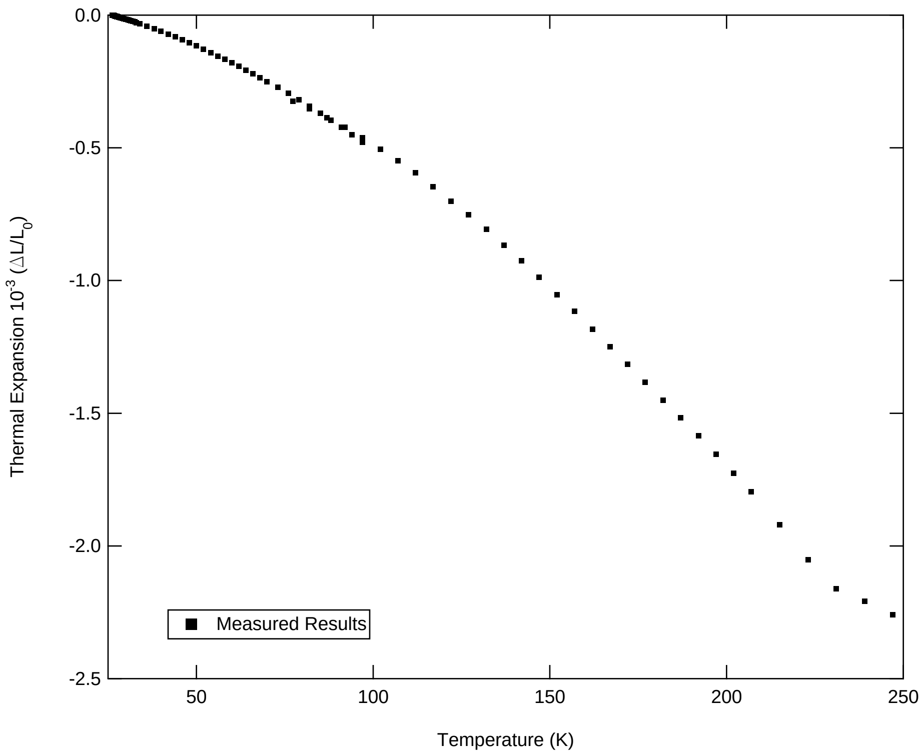

Figure 6.12: Thermal expansion results measured along off-axis. No evidence of any structural change sharper than 10 K and smaller than the difference between x-ray data points.

To summarize the off-axis results, the thermal expansion coefficient along the off-axis was found to be net negative and larger than the experimental cell effect. Unlike the a-axis, a low temperature feature is observed at the similar tempreatures to the features observed along the c-axis.

6.5 Conclusion

The thermal expansion coefficient along the c, a and off-axis are measured. With regards to the c and off-axis, the crossover region shows an approximately 2×10^{-6} gap magnitude but preserves the overall profile. This difference must be addressed to create perfectly continuous results from liquid ^{4}He temperatures to above liquid N_2 temperatures. The high temperature anomaly at $T \approx 230$ K, believed to be systematic in nature, requires further investigation to understand its origin.

Both c and off-axis thermal expansion measurements observe a peak at $T = 26.8$ K which, compared to the profile of the displacive structural phase transition of $SrTiO_3$ is strong evidence for a displacive structural phase transition present in $Ba_3NbFe_3Si_2O_{14}$. A smaller, lower temperature peak at $T_N = 25.9$ K is observed which coincides with the magnetic transition shown in specific heat.

With regards to the a-axis, the measured thermal expansion coefficient order of magnitude is on the same order as the fused quartz cell effect. Measurement of the cell effect at this temperature range is required to form conclusions for the a-axis. The a-axis thermal expansion coefficient is believed to be so small that it exceeds the limits of even the quartz dilatometer.

The corresponding feature of the displacive structural phase transition in thermal expansion measurements along the c and off-axis satisfy the requirement of being sharper than 10 K and smaller than the difference between x-ray data points. Thermal expansion measurement along the a-axis are inconclusive as the values are on the same order of magnitude as the cell effect.

Chapter 7

Conclusions

This thesis is believed to cover a vast number of topics. In this concluding chapter, the each chapter will be summarized individually focusing on developments made in each topic. Each section will try to offer an avenue of future study.

Theoretical Background

This chapter justified from a theoretical standpoint the ability to observe phase transitions through the thermal expansion coefficient. To first order, property known as the Grüneisen parameter provides a temperature independent scaling between specific heat contributions and corresponding thermal expansion coefficient contributions. A better understanding behind the governing principles for each Grüneisen parameter is needed to improve comparison between specific heat and thermal expansion coefficient results.

Capacitive Dilatometry

This chapter covered many details regarding the experimental technique used to measure the thermal expansion coefficient. The larger portion of the chapter focused on developing new dilatometer devices that addressed concerns of large cell effect. A fused quartz dilatometer was developed and documented considering many aspects of the design. A copper dilatometer was also developed for $T < 1$ K experiments. The rigorous measurement of the cell effect for the dilatometer devices presented in this chapter are required to facilitate quantitative results of the thermal expansion coefficient. The characterization of the cell effect is also needed required determine the attainable resolution. This resolution can be further improved by studying various factors that may impact the device.

$LiHoF_4$

This chapter addressed the possibility of re-entrant behaviour of the material near the classical critical point. A high density of low transverse field critical points were obtained and with appropriate magnetoresistance correction showed that $LiHoF_4$ did not have re-entrant behaviour. The discrepancy between theoretical and experimental results near the classical critical point has yet to be resolved. The material Fe_8 shows a similar disagreement and further study of this material may reveal additional information regarding the discrepancy of these transverse field quantum Ising model materials.

$Tb_2Ti_2O_7$

This chapter presented thermal expansion coefficient measurements in the low temperature $T < 1$ K regime. Two scenarios are presented based on the intepretation of the results along with other published results. Two features are observed in the thermal expansion coefficient; one at $T \approx 100$ mK and the other at $T \approx 500$ mK. Determining the origin of these features could provide evidence toward determining the correct scenario that describes the material. This would involve the application of a secondary parameter such as magnetic field or sample doping. Observing how the features behave under these changes would serve to provide more information to the origins of these features.

$Ba_3NbFe_3Si_2O_{14}$

This chapter studied the thermal expansion coefficient along the crystallographic axes in search for evidence of a structural phase transition. Results along the c and off-axis found evidence of a displacive structural phase transition at $T \approx 26.8 - 26.9$ K. The a-axis results were inconclusive due to the considerably smaller thermal expansion coefficient. The current state of the measurement results require further experimenting before other avenues be considered. A repeat study of the alleged displacive structural phase transition can be performed to verify rhe result. Additionally, a high temperature anomalous feature at $T \approx 230$ K, believed to be systematic requires needs to be addressed.

Appendices

Appendix A

Installing Coaxial Lines in Cryogenic Systems

A crucial component in low temperature measurement is the installation of electrical lines. In the case of capacitive dilatometry, the lines used are coaxial cables. Previous use of twisted pair cables resulted in large fluctuations of the capacitance (Fig. A.1)

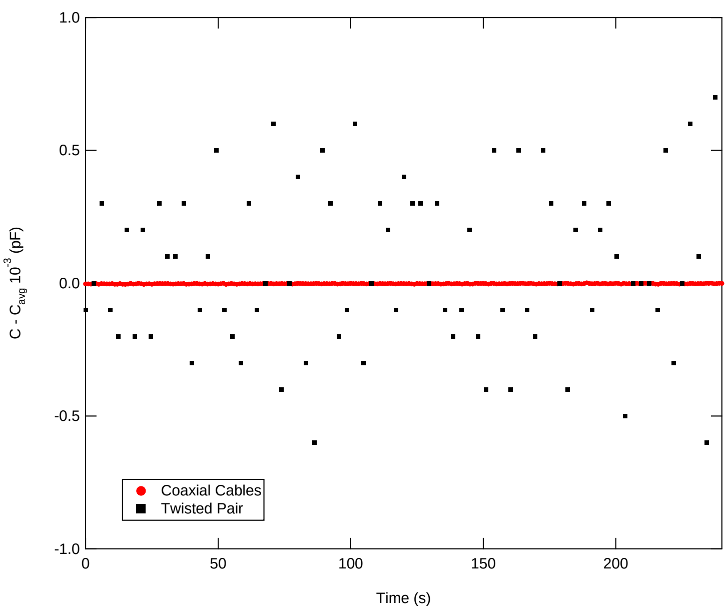

Figure A.1:

Cable considerations are important they serve as sources of heat that must be minimized to ensure ideal operating conditions. Before installing measurement lines, two things must be considered: thermal anchoring and cable specifications.

Thermal Anchoring

Without thermal anchoring of the lines to cold plates on the refrigerator, the probe end would feel the full brunt of the heating as there would be no way to readily dissipate the heat coming from the room temperature end. To prevent this, the coaxial cables are thermally anchored using copper brackets to the cold plates. This ensures that no excess heat is transferred down to the colder parts of the fridge. The first anchor point is at the top of the fridge at a temperature of 4.2K; the liquid ^{4}He bath. This thermal anchor should remove the greater majority of the heat from the lines but by itself is not sufficient. The next thermal anchor occurs at 1 K where the aptly named 1 K pot is located. After the 1 K pot, the final thermal anchor is on the mixing chamber plate operating at temperatures below 100 mK. Each of these anchor points should ensure minimal excess heat from hotter plates provided the cable specifications do not permit a large heat transference.

Cable Specifications

The quantity of heat transfer is ultimately dependent on the dimensions and material of the coaxial line. The heat transfer through solids is governed by the cross section A, length l, temperature dependent thermal conductivity $\lambda(T)$ and temperatures T_1 and T_2. The formula is:

$$\dot{Q} = \frac{A}{l}\int_{T_1}^{T_2} \lambda(T)dT \tag{A.1}$$

In practice using the formula is difficult as the thermal conductivity varies as a function of temperature. Fortunately, the mean thermal conductivy of common materials across common temperature differences is provided in the Heat Transfer chapter of Ref. [] and recreated in Table. A.1. The equation for heat transfer using the mean thermal conductivity is:

$$\dot{Q} = \frac{A}{l}\Delta T\bar{\lambda}_{T_2,T_1} \tag{A.2}$$

Where

$$\bar{\lambda}_{T_2,T_1} = \frac{1}{T_1 - T_2}\int_{T_1}^{T_2} \lambda(T)dT \tag{A.3}$$

	$\bar{\lambda}_{300K,77K}$	$\bar{\lambda}_{300K,4K}$	$\bar{\lambda}_{77K,4K}$	$\bar{\lambda}_{4K,1K}$	$\bar{\lambda}_{1K,0.1K}$
Nylon	0.31	0.27	0.17	0.006	0.001
Pyrex glass	0.82	0.68	0.25	0.06	0.006
Machineable glass-ceramic	2	1.6	1.3	0.03	0.004
Graphite (AGOT)	-	-	-	0.0025	0.0002
18/8 stainless steel	12.3	10.3	4.5	0.2	0.06
Constantan (60 Cu, 40 Ni)	20	18	14	0.4	0.05
Brass (70 Cu, 30 Ni)	81	67	26	1.7	0.35
Copper (P deoxidized)	190	160	80	5	(1)
Copper (electrolytic)	410	570	980	200	(40)

Table A.1: Mean thermal conductivity in W/mK. Bracketed values are extrapolated

The coaxial cable used on the dilution fridge were SR (semi-rigid) cables from LakeShore Cryogenics. The technical specifications for the coaxial cable is below taken from the website.

Cable

Specifications

	Type C	Type SC	Type SS	Type SR
Dimensions				
Center conductor – AWG (diameter)	32 (0.2032 mm [0.008 in])	32 (0.2032 mm [0.008 in])	32 (0.2032 mm [0.008 in])	37 (0.1143 mm [0.004 in])
Dielectric/insulating material (diameter)	0.56 mm (0.022 in)	0.406 mm (0.016 in)	0.406 mm (0.016 in)	0.38 mm (0.015 in)
Shield (diameter)	0.025 mm (0.001 in) thickness	0.711 mm (0.028 in)	0.711 mm (0.028 in)	0.51 mm (0.02 in)
Drain wire (parallel to conductor)	32 AWG (0.203 mm [0.008 in])	NA	NA	NA
Jacket outer dimension	0.7874 mm × 1.016 mm (0.031 in × 0.039 in)	1.0 mm (0.04 in)	1.0 mm (0.04 in)	0.51 mm (0.02 in)
Material				
Center conductor	Silver-plated copper	Stranded copper[1]	304 stainless steel[2]	Carbon steel[3]
Dielectric/insulating material	Gore-Tex® expanded PTFE	Teflon® FEP	Teflon® FEP	Teflon® PTFE
Shield	Aluminized polyester[4]	Braided gold-plated copper[5]	304 braided stainless[6]	304 stainless steel[7]
Drain wire	Silver-plated copper	NA	NA	NA
Jacket material	FEP	Teflon® FEP	Teflon® FEP	NA
Jacket color	Blue	Gold	Gray	NA
Electrical Properties				
Resistance Ω/m (Ω/ft)				
Center conductor at 293 K (20 °C)	0.541 (0.165)	0.282 (0.086)	23.62 (7.2)	4.30 (1.31)
Shield at 296 K (23 °C)	NA	0.085 (0.026)	3.61 (1.1)	8.63 (2.63)
Drain wire at 296 K (23 °C)	0.541 (0.165)	NA	NA	NA
Center conductor max. DC voltage	150 V	600 V	600 V	700 V
Center conductor max. DC current	150 mA	200 mA	200 mA	200 mA
Temperature range	10 mK to 400 K	<1 K to 400 K	10 mK to 473 K	10 mK to 400 K
Characteristic impedance	50 Ω (±5 Ω)	35 Ω at 10 MHz	40 Ω at 10 MHz	50 Ω (±2 Ω)
Nominal capacitance at 5 kHz	79 pF/m (24 pF/ft)	154.2 pF/m (47 pF/ft)	173.9 pF/m (53 pF/ft)	95.14 pF/m (29 pF/ft)

[1] 65 strands of 50 AWG
[2] 64 strands of 50 AWG 304 SS wire
[3] Silver-plated copper-clad carbon steel (0.103 mm outer diameter carbon steel covered by 0.0057 mm thick copper cladding covered by 0.001 mm thick silver plating
[4] Aluminized polyester laminated tape, spirally applied at a 40–50% overlap, aluminum side in
[5] 12 × 3 matrix of 42 AWG wire
[6] 12 × 4 matrix of 44 AWG wire
[7] A seamless tubular metal jacket serves as the outer conductor/shield

Sample Calculations

Here are calculation for the coaxial lines installed in the dilution fridge. These calculations are used to gauge how long the coaxial lines need to be in each section to have a sufficiently low heat transfer. The heat transfer is deemed to be sufficiently low provided it is less than two copper electrical lines currently installed on the fridge. The reason behind comparing a single coax line to two copper lines is because two are required to make a twisted pair line. First the cable dimensions of both coax and copper lines are computed.

$$\begin{aligned}
\phi_{core} &= 0.1143 \text{ mm} \rightarrow A_{core} &&= \pi(\tfrac{\phi_{core}}{2})^2 &&= 1.026 \times 10^{-8} m^2 \\
\phi_{dielectric} &= 0.380 \text{ mm} \rightarrow A_{dielectric} &&= \pi((\tfrac{\phi_{dielectric}}{2})^2 - (\tfrac{\phi_{core}}{2})^2) &&= 1.031 \times 10^{-7} m^2 \\
\phi_{shield} &= 0.510 \text{ mm} \rightarrow A_{shield} &&= \pi((\tfrac{\phi_{shield}}{2})^2 - (\tfrac{\phi_{dielectric}}{2})^2) &&= 9.087 \times 10^{-8} m^2 \\
\phi_{copper} &= 0.050 \text{ mm} \rightarrow A_{copper} &&= 2\pi(\tfrac{\phi_{copper}}{2})^2 &&= 3.927 \times 10^{-9} m^2
\end{aligned}$$

Next, the heat transfer for the copper lines are computed. The copper lines are coiled around support rods measuring approximately 5 to 6.5 mm in diameter running down the fridge. The lengths are estimated to be:

$$l_{300K,4K} \approx 2 \text{ m} \qquad l_{4K,1K} \approx 0.41 \text{ m} \qquad l_{1K,0.1K} \approx 0.343\text{m}$$

The heat transfer for each section can now be computed. Using electrolytic copper the heat transfer values are determined:

$$\begin{aligned}
\dot{Q}_{300K,4K} &= \tfrac{3.927\times10^{-9}}{2}(296)(570) &&= 3.313 \times 10^{-4} \text{ W} \\
\dot{Q}_{4K,1K} &= \tfrac{3.927\times10^{-9}}{0.41}(3)(200) &&= 5.747 \times 10^{-6} \text{ W} \\
\dot{Q}_{1K,0.1K} &= \tfrac{3.927\times10^{-9}}{0.343}(0.9)(40) &&= 4.121 \times 10^{-7} \text{ W}
\end{aligned}$$

Next the length normalized coaxial line calculation for the stainless steel portion. The Teflon dielectric is assumed to be close to nylon for thermal conductivity values and are much less than that of steel. Therefore, the dielectric component does not add a substantial amount of heat transfer to the coaxial lines. The total stainless steel area is $A = 1.011 \times 10^{-7} m^2$.

$$
\begin{aligned}
(\dot{Q}l)_{300K,4K} &= (1.011 \times 10^{-7})(296)(10.3) && = 3.083 \times 10^{-4}\ \text{Wm} \\
(\dot{Q}l)_{4K,1K} &= (1.011 \times 10^{-7})(3)(0.2) && = 6.068 \times 10^{-8}\ \text{Wm} \\
(\dot{Q}l)_{1K,0.1K} &= (1.011 \times 10^{-7})(0.06)(40) && = 5.461 \times 10^{-9}\ \text{Wm}
\end{aligned}
$$

From these numbers, minimum lengths for each section can be determined. For the 300 K to 4 K section, the length of coaxial cable must be greater than ≈ 1 m to have a comparable heat transfer to the copper lines. Between 4 K to 1 K and 1 K to 0.1 K, more than *approx* 0.01 m. Needless to say, any substantial amount of SR coaxial cable between 4 K to 0.1 K should add negligible heat transfer to the fridge.

Technical Details

In order to accomodate the SR coaxial cable, several different connectors are used. Within the fridge, LEPRA/CON ultra-miniature connectors are used because of their low profile and non-magnetic nature. TE Connectivity (formerly Tyco Electronics) is the wholeseller of these connectors. The most recent connectors were ordered from March Electronics; a distributor for TE Connectivity products. An outdated catalog of connectors sold by TE Connectivity can also be found in the 'Catalogs' folder in the dropbox.

On the other end, an SMA connector was used as these connectors are larger and more robust. The SMA connector used was 11SMA-50-UT20 from Microstock Inc.. This connector assembly allowed for a sub-sized coaxial cable to terminate as an SMA. The assembly instructions are shown below.

The very top of the fridge is sealed with a vacuum flange with hermetic SMA female-female bulkheads. These items are relatively common and many different styles can be readily purchased. The vacuum flange was specifically machined to accommodate 4 SMA bulkheads. The schematic for this component is also attached.

MICROSTOCK, INC.
P.O. BOX 91, WEST POINT, PA 19486-0091
(215) 699-0355 FAX: (215) 699-0286
E-Mail : URL : www.microstock-inc.com

Assembly instruction

N4 No. 1007

Tools and materials required:
Soldering iron 80 to 100 Watts/200...240°C
Solder Sn/Pb 60/10, 0.8 mm ⌀, activated rosin flux
Alcohol, brush, Stanley blade

Syringe W 115
Epoxy-Kit 74 Z-0-0-116 or Sigma Plastronics
Instruction sheet 9126 #1 Vary Flex Epoxy

Straight connector for semi-rigid cable UT-20, UT-20M

Cable entry: soldered

Connector: 11SMA-50-UT20

This connector is supplied in 6 parts

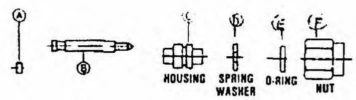

Cut cable end in a plane perpendicular to the cable axis. Trim outer jacket and dielectric .080" from end of cable per diagram. CAUTION: Do not damage inner conductor!

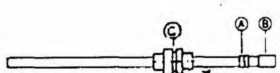

Slide housing C over cable with teflon side facing stripped cable end. Push tiny insulator A onto exposed inner conductor. Slide contact B onto inner conductor, push against insulator A, solder to conductor.
Do not apply excessive heat!

Push pin B (back end first) into teflon opening in housing C until contact shoulder is .000/.008" from reference plane as shon on page 2.
Solder housing C to cable. Do not apply excessive heat!
Check contact stack-up for compliance to MIL-C-39012 requirements. If Necessary, reflow solder and adjust stack-up.

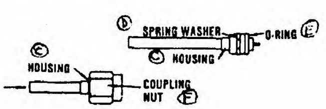

Inject #1 Vary Flex Epoxy into body cross drill hole until it just begins to extrude from opposite side. Carefully remove excess. Allow epoxy to cure 24HRS at room temperature. Then bake @ 150 F for 2 HRS. Install gasket E on body. Snap spring washer D into groove on body. Compress lockring with lockring pliers & push nut F in place on body.

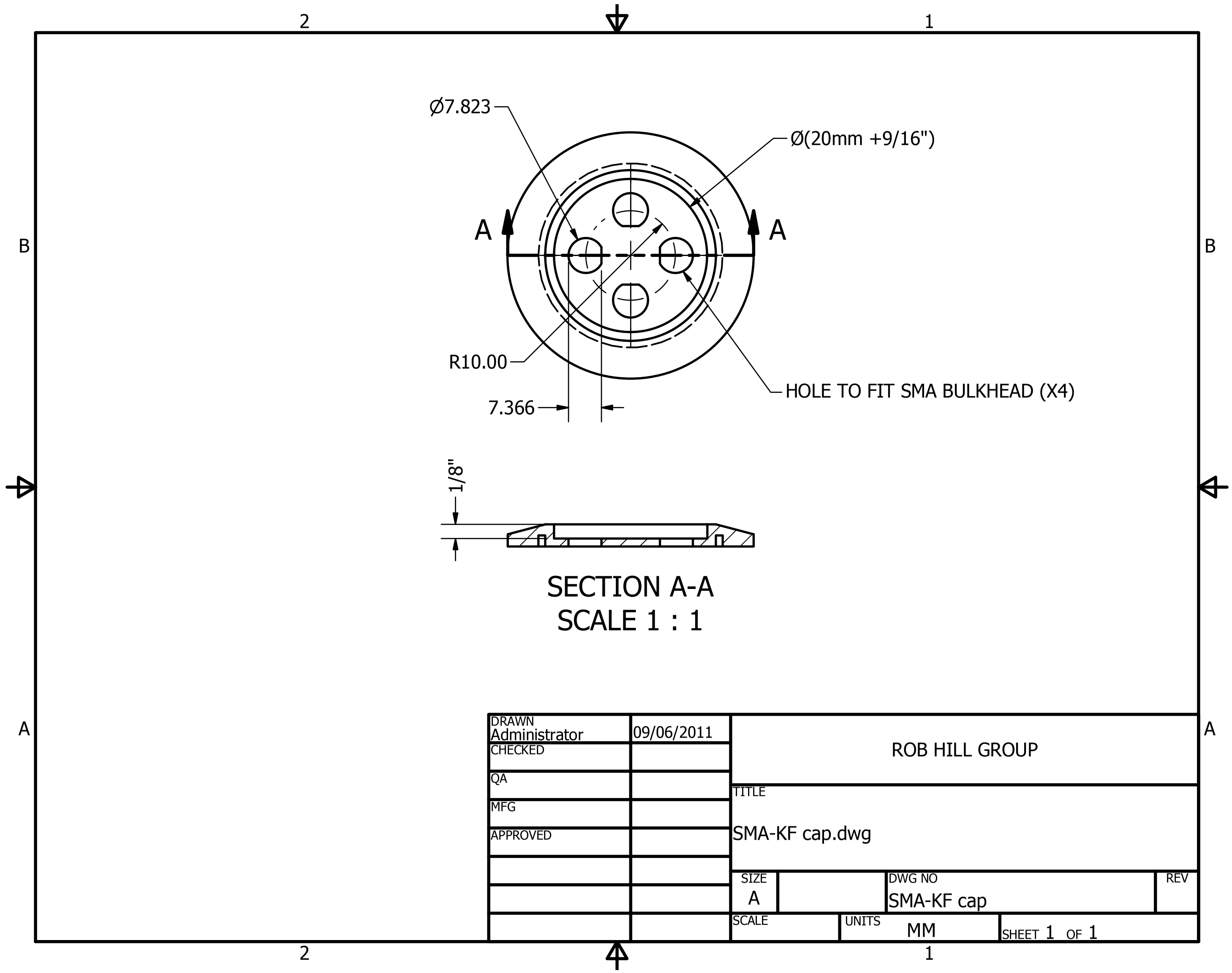

Ø7.823
Ø(20mm +9/16")
A
A
R10.00
7.366
HOLE TO FIT SMA BULKHEAD (X4)
1/8"
SECTION A-A
SCALE 1 : 1
DRAWN
Administrator
09/06/2011
CHECKED
QA
MFG
APPROVED
ROB HILL GROUP
TITLE
SMA-KF cap.dwg
SIZE
A
DWG NO
SMA-KF cap
REV
SCALE
UNITS
MM
SHEET 1 OF 1

Appendix B

The Multiplexer Unit

The capacitive multiplexing units were purchased from Universal Switching Corporation to allowing up to potentially eight capacitive devices to be measured during experiments. Through the use of inductor coils, each channel can be switched on or off. The purchased model is U74008-1PL and is rated for high isolation to reduce any electrical noise. The configuration and schematic diagram (Fig. B.1) was taken from the Resource Disc provided by the company.

Unfortunately, the multiplex units require 500mA current to excite the inductor coils while the AH-2550A capacitance bridge can only supply 125mA. This meant that a secondary circuit used as a switch to a larger power supply was needed. A secondary circuit using transistor switches drives a 25V 500mA linear power supply. The transistors serve as electrical switches to the multiplexer units while the signals from the capacitance bridge now control the transistors. The control comes from the Sample Switch Port on the back of the capacitance bridge. Operations and Maintenance manual outlines the use of this port in an appendix. Electronic scans of the appendix are included below.

The multiplexer box was designed in such a way to shield all the electrical components from one another. The schematics for the components of the multiplexer box are saved here.

In recent ultra precise capacitive measurements, it was found that the multiplexing unit as a whole provides a 1Hz oscillation in both the loss and capacitance measurement. The fluctuations vary in the last digit in capacitance (1E-6pF) and the fifth digit (1E-5nS) in loss. To be able to use said device for ultra low noise measurements, this issue must be resolved.

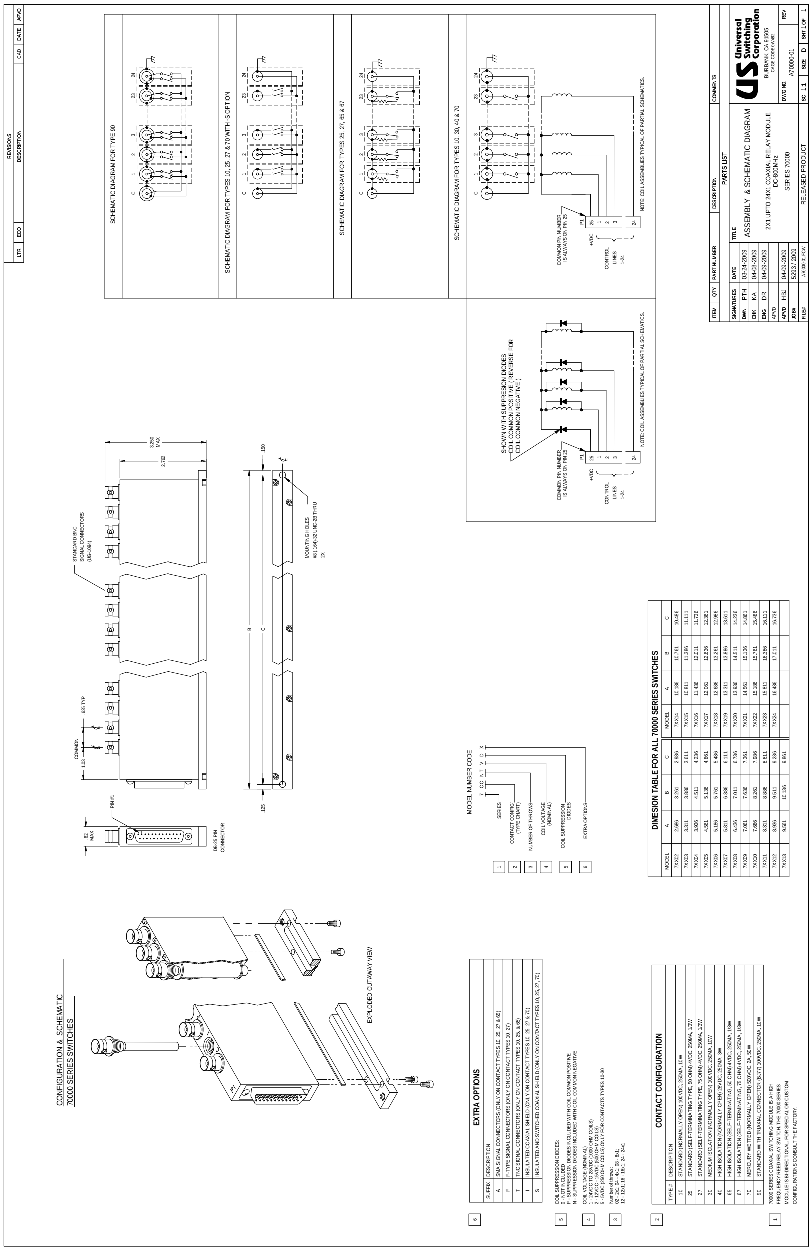

Figure B.1: The designation for the multiplexing component from USC

PARTS LIST			
ITEM	QTY	PART NUMBER	MATERIAL
1	1	FrontPanel	Aluminum
2	1	BackPanel	Aluminum
3	2	WidthBarRight	Aluminum
4	2	WidthBarLeft	Aluminum
5	2	HeightBar	Aluminum
6	2	MidHeightBarUSC	Aluminum
7	2	ShieldWall2	Aluminum

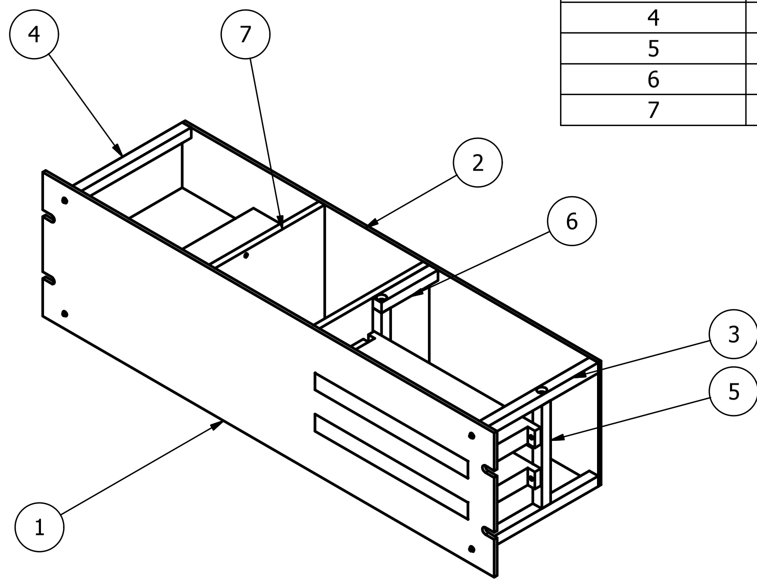

DRAWN BY
KEVIN LIU
EXTENSION
32166
CREATED
14/07/2011
MAT'L
QTY
PRIMARY UNITS
IMPERIAL

ROB HILL GROUP
LOW TEMPERATURE II

TITLE

SIZE A | FILE NAME Box.iam | REV

SCALE | SHEET 1 OF 6

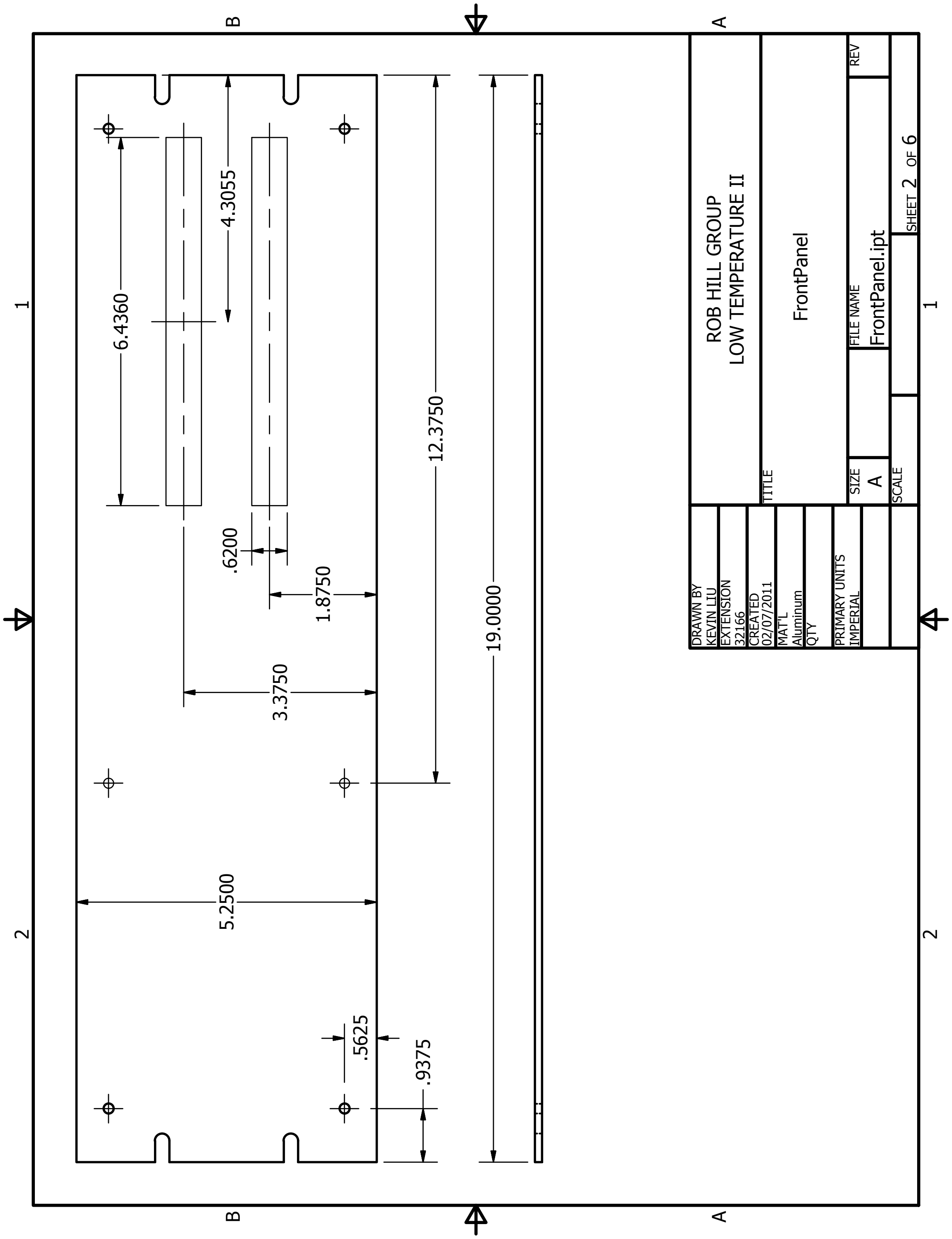
ROB HILL GROUP
LOW TEMPERATURE II
TITLE
FrontPanel
FILE NAME
FrontPanel.ipt
SIZE
A
SCALE
REV
SHEET 2 OF 6
DRAWN BY
KEVIN LIU
EXTENSION
32166
CREATED
02/07/2011
MAT'L
Aluminum
QTY
PRIMARY UNITS
IMPERIAL
6.4360
4.3055
12.3750
19.0000
.6200
1.8750
3.3750
5.2500
.5625
.9375

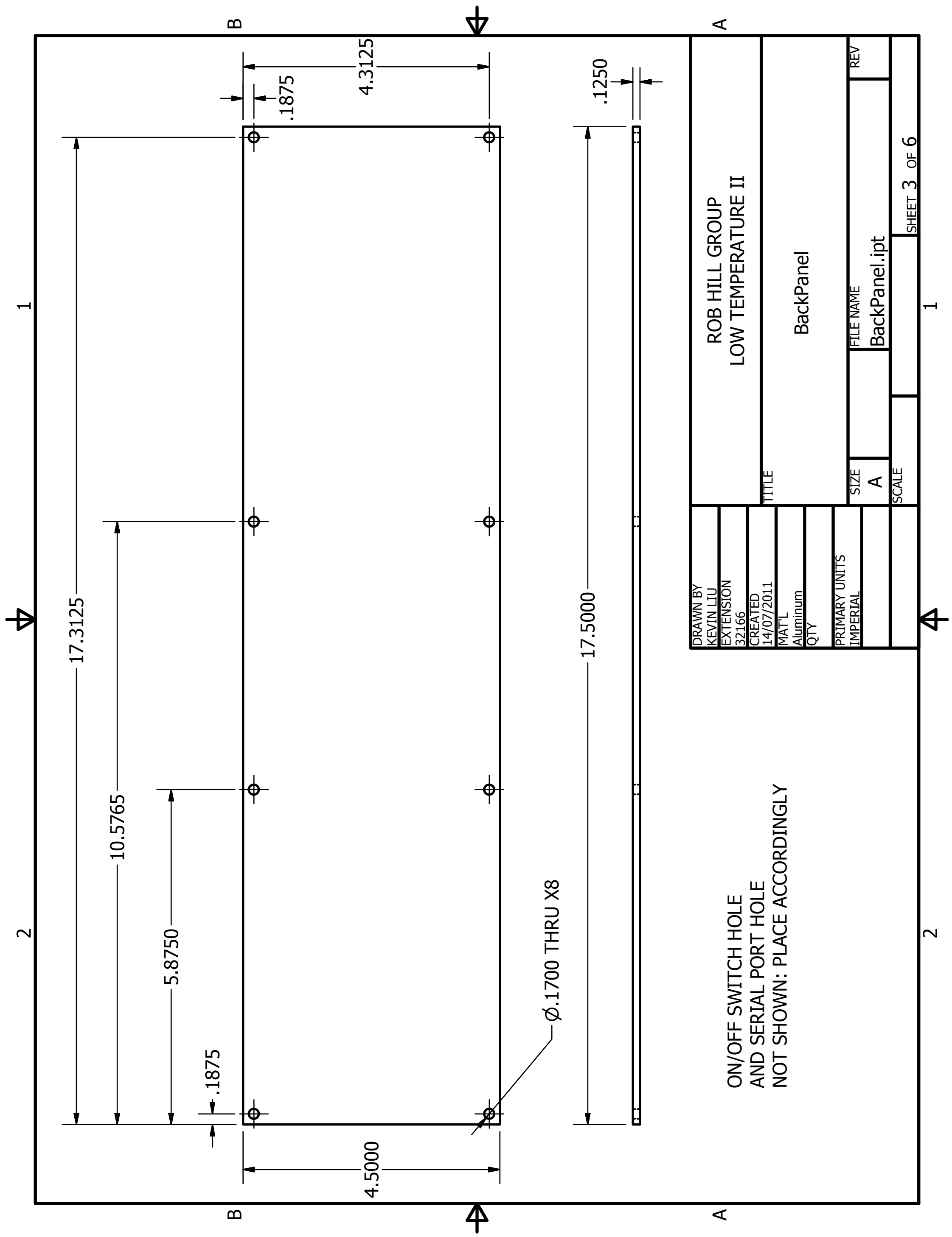

ROB HILL GROUP
LOW TEMPERATURE II
TITLE
BackPanel
SIZE
A
FILE NAME
BackPanel.ipt
SHEET 3 OF 6
REV
SCALE
DRAWN BY
KEVIN LIU
EXTENSION
32166
CREATED
14/07/2011
MAT'L
Aluminum
QTY
PRIMARY UNITS
IMPERIAL
ON/OFF SWITCH HOLE
AND SERIAL PORT HOLE
NOT SHOWN: PLACE ACCORDINGLY
Ø.1700 THRU X8
17.3125
10.5765
5.8750
.1875
4.5000
4.3125
.1875
.1250
17.5000
A
B
1
2

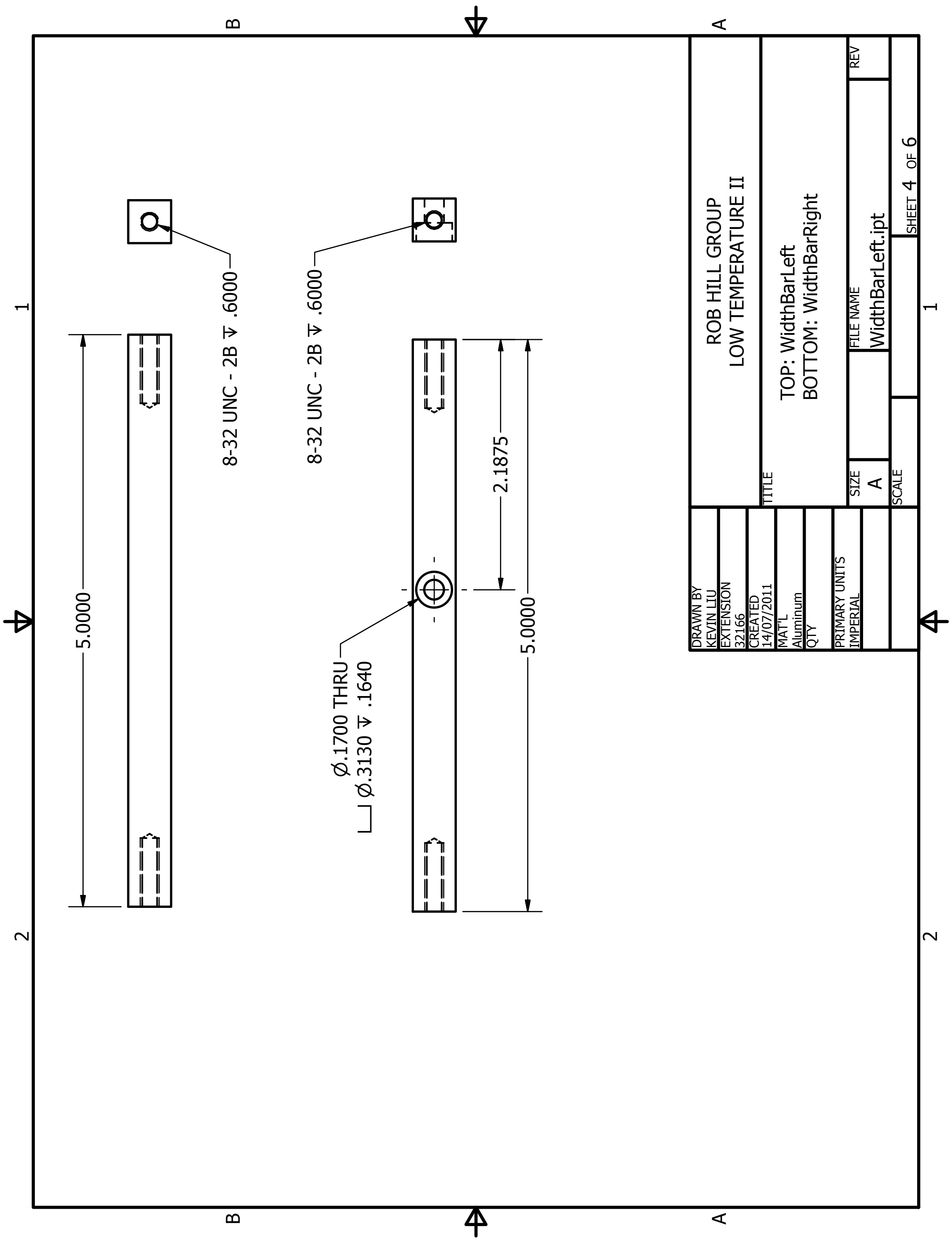
8-32 UNC - 2B ↧ .6000
8-32 UNC - 2B ↧ .6000
5.0000
2.1875
5.0000
⌀.1700 THRU
⌴ ⌀.3130 ↧ .1640
ROB HILL GROUP
LOW TEMPERATURE II
TITLE
TOP: WidthBarLeft
BOTTOM: WidthBarRight
DRAWN BY
KEVIN LIU
EXTENSION
32166
CREATED
14/07/2011
MAT'L
Aluminum
QTY
PRIMARY UNITS
IMPERIAL
SIZE
A
FILE NAME
WidthBarLeft.ipt
SCALE
SHEET 4 OF 6
REV

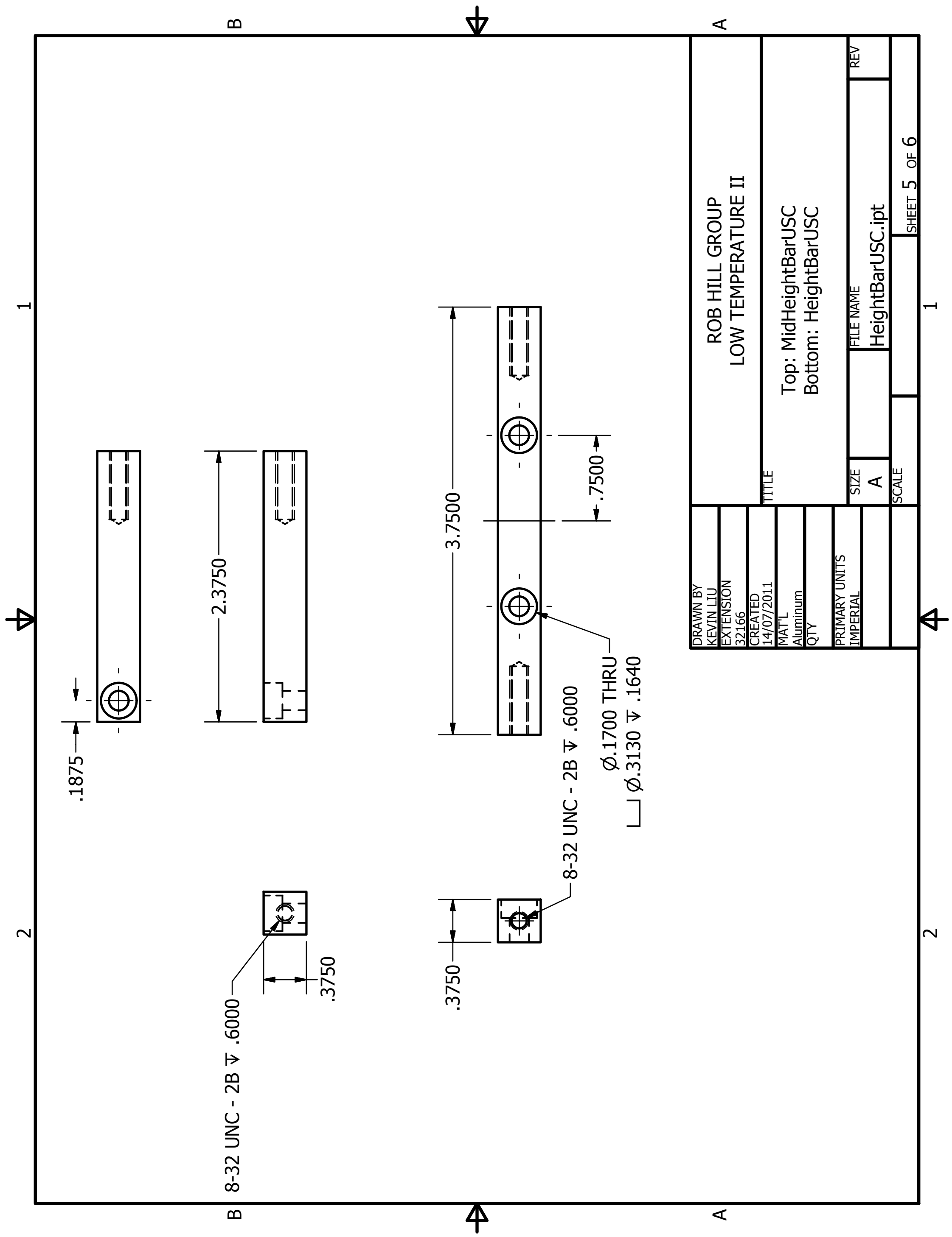

ROB HILL GROUP
LOW TEMPERATURE II
TITLE
Top: MidHeightBarUSC
Bottom: HeightBarUSC
REV
SHEET 5 OF 6
FILE NAME
HeightBarUSC.ipt
SIZE
A
SCALE
DRAWN BY
KEVIN LIU
EXTENSION
32166
CREATED
14/07/2011
MAT'L
Aluminum
QTY
PRIMARY UNITS
IMPERIAL
.1875
2.3750
3.7500
.7500
Ø.1700 THRU
⌴ Ø.3130 ↧ .1640
8-32 UNC - 2B ↧ .6000
.3750
.3750
8-32 UNC - 2B ↧ .6000
A
B
1
2

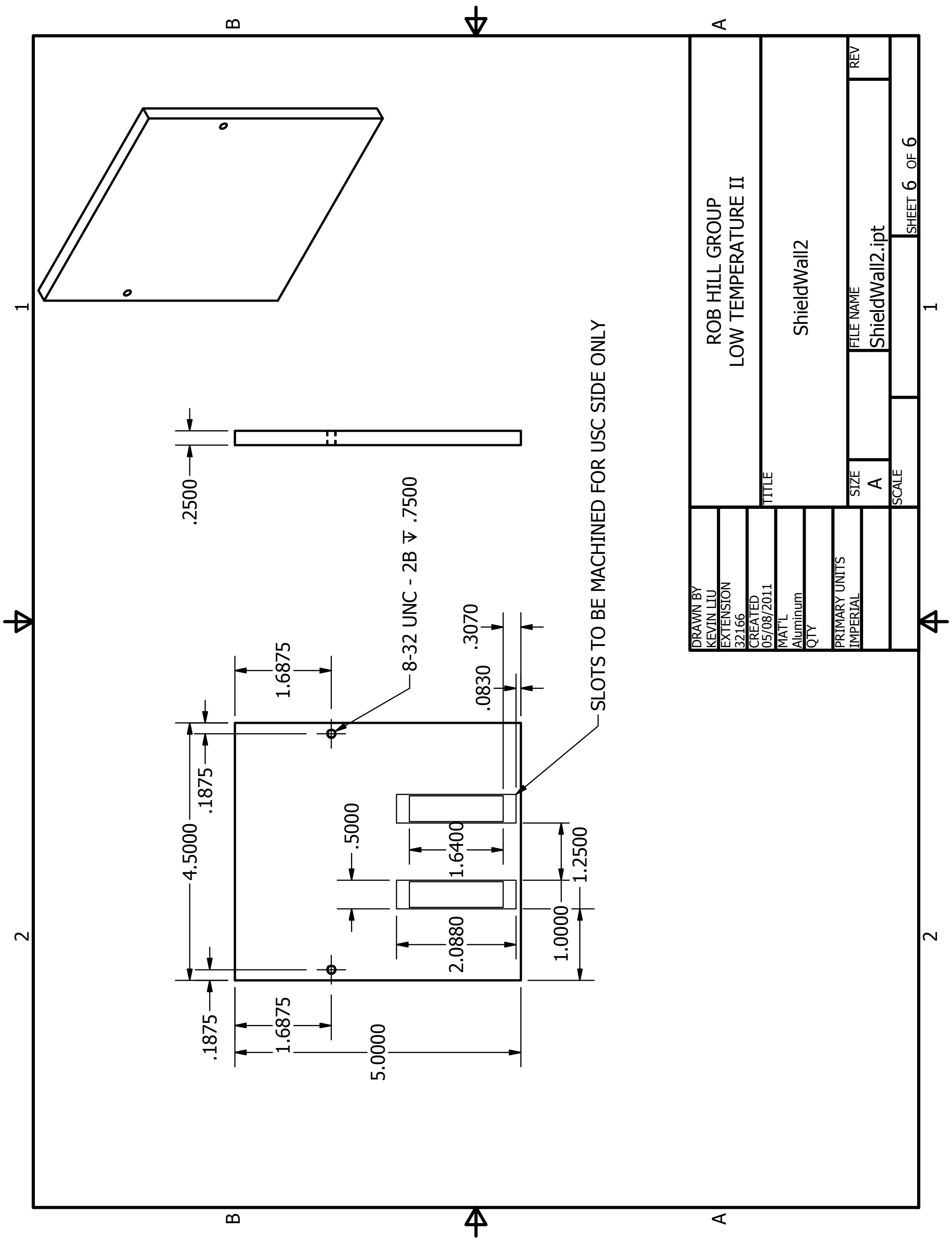
ROB HILL GROUP
LOW TEMPERATURE II
TITLE
ShieldWall2
DRAWN BY
KEVIN LIU
EXTENSION
32166
CREATED
05/08/2011
MAT'L
Aluminum
QTY
PRIMARY UNITS
IMPERIAL
SIZE
A
FILE NAME
ShieldWall2.ipt
REV
SHEET 6 OF 6
SCALE
SLOTS TO BE MACHINED FOR USC SIDE ONLY
8-32 UNC - 2B ↧ .7500
.2500
1.6875
.3070
.0830
.1875
4.5000
.5000
1.6400
1.2500
1.0000
2.0880
.1875
1.6875
5.0000
A
B
1
2

The AH2550A incorporates a connector on its rear panel that is intended to provide signals to control an external coaxial switch. Such a switch is useful for selecting among several unknown samples. An AH2550A command is provided to allow program control of such a switch.

At the time of publication of this manual, Andeen-Hagerling does not manufacture a sample switch. However, such a product is planned. If you are interested, watch for announcements.

In the meantime, the sample switch port can be used to control sample switches of your own design. It is also not difficult to build an interface to commercially available products if you have some electronics experience.

Basic Operation

The sample switch port is a parallel port with eight data lines and a strobe line. These lines use RS-232 drivers that produce ±12 volt signal levels. Five power lines are also present. These can provide up to 100 mA of current to external devices. The two 24 volt power supplies are unregulated. The other three supplies are well regulated.

The eight data lines are decoded so that only one line is true at a time. The lines are high-true which means that one line will always produce +12 volts and all the rest will produce -12 volts. These data lines can be connected directly to non-inverting relay driver circuits with no further decoding or other logic. This allows one of up to eight relays to be selectively closed.

Connector Description

The connector on the backpanel is a fifteen pin female "D" style. The pinout of this connector is given in Table D-1.

Selecting a Sample Switch Position

The data line that is true is selected with the following command:

SAMPLE *number*

The *number* parameter specifies the sample to be measured. It can have any value from 1 to 64, however, values of this parameter larger than eight will cause all sample switch data lines to be false. Values from one to eight will cause one of the eight sample switch data lines to be true. The number of the selected sample switch signal name is one less than the value of the *number* parameter. These values are listed in

C01

Table D-1 Sample switch connector pinouts

Pin No.	Signal Name	Signal Description	True for *number*
1	SD0	Sample Switch Data 0	1
2	SD2	Sample Switch Data 2	3
3	SD4	Sample Switch Data 4	5
4	SD6	Sample Switch Data 6	7
5	GND	Ground	
6	+5V	+5 Volt Power	
7	+24V	+24 Volt Power	
8	+12V	+12 Volt Power	
9	SD1	Sample Switch Data 1	2
10	SD3	Sample Switch Data 3	4
11	SD5	Sample Switch Data 5	6
12	SD7	Sample Switch Data 7	8
13	SC	Sample Switch Data Valid	
14	-12V	-12 Volt Power	
15	-24V	-24 Volt Power	

Table D-1. The default value of the sample switch *number* parameter stored in the BASIC 0 parameter file is 1.

The utility of the SAMPLE command may be greatly enhanced when used with the AH2550A's PROGRAM features. Obviously, the SAMPLE command is also useful when incorporated into programs run on remote controllers.

Signal Timing

The sample switch port has two timing issues. One is the timing of the strobe line relative to the data lines. The other is amount of time to wait after changing the sample switch setting before taking a measurement. This is called the settling time.

The Strobe Line Timing

If the sample switch data lines directly control relay driver circuits with no logic in between, then the Sample Switch Data Valid line will not be used. On the other hand, if the data from the sample switch data lines is to be externally latched, then the Sample Switch Data Valid line will be required to strobe the latch.

The Data Valid line is true when the sample switch data is stable and false when it may not be. The Data Valid line goes false (-12V) 250 microseconds before the data lines change. It goes true again (+12V) 250 microseconds after they change. If the data is to be strobed into a latch, this would normally be done by using the false-to-true transition of the Data Valid line.

Changing the Settling Time

A time delay can be specified that automatically occurs after each execution of the SAMPLE command. This provides a settling time for sample switch relays to stabilize after being switched. The syntax of the command that specifies this delay is:

SAMPLE HOLD *delay*

This *delay* parameter is entered in seconds to the nearest hundredth.

The SAMPLE command will not finish until the delay time has expired. This holds off any further operations.

The *delay* time is the same no matter what sample number has been selected. If some samples require a longer settling time than others, additional settling time can be provided by executing the HOLD command after executing the SAMPLE command for the slower samples.

If the SAMPLE command is executed with a long delay time, you must wait for this time to elapse or abort the SAMPLE command with a DEVICE CLEAR command.

The default value of the sample switch *delay* parameter stored in the BASIC 0 parameter file is 0.0 seconds.

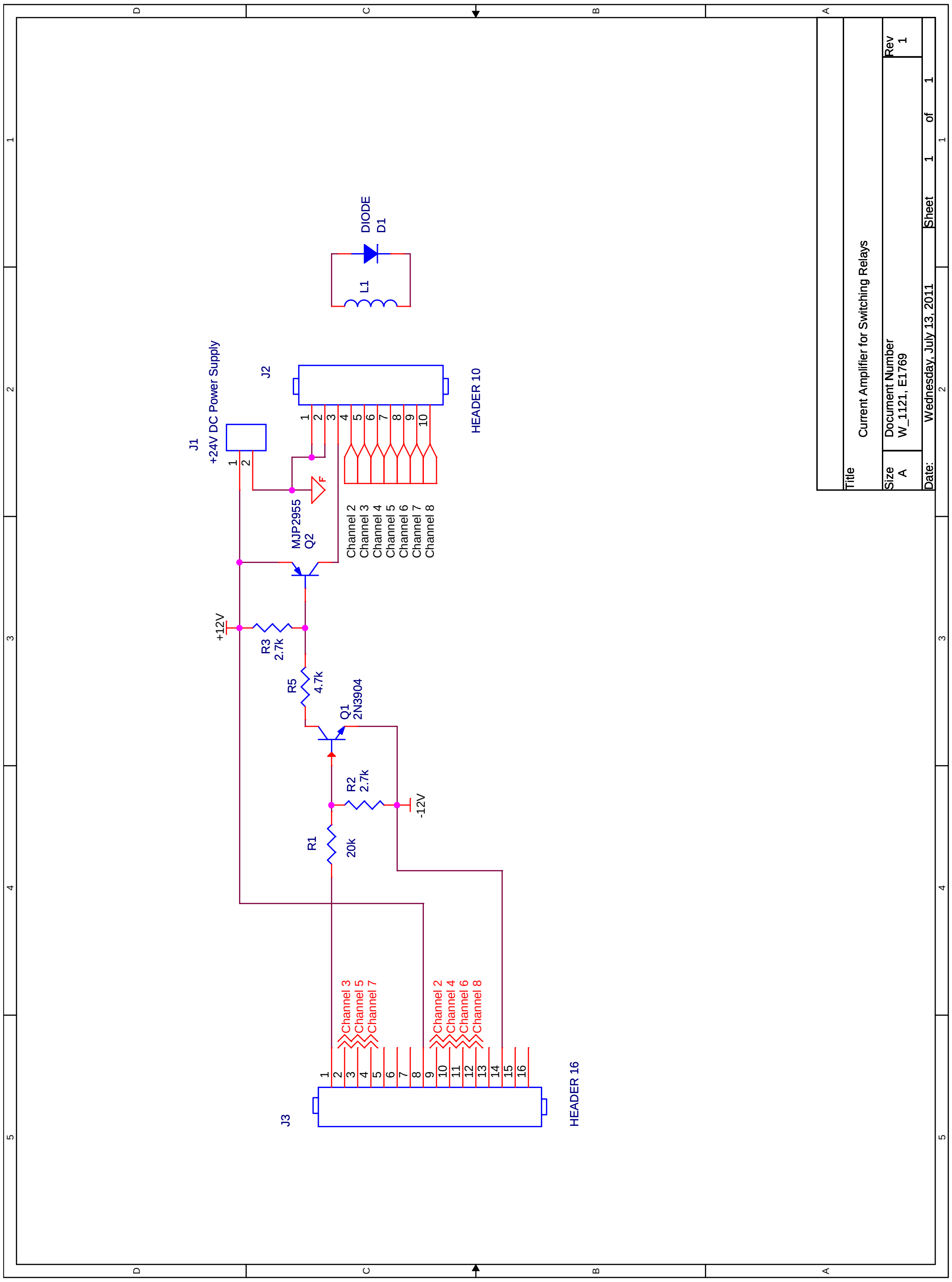
J1
+24V DC Power Supply
J2
HEADER 10
DIODE
D1
L1
MJP2955
Q2
+12V
R3
2.7k
R5
4.7k
Q1
2N3904
R2
2.7k
-12V
R1
20k
Channel 2
Channel 3
Channel 4
Channel 5
Channel 6
Channel 7
Channel 8
J3
HEADER 16
Title
Current Amplifier for Switching Relays
Size
A
Document Number
W_1121, E1769
Rev
1
Date:
Wednesday, July 13, 2011
Sheet
1
of
1

talk briefly about how the multiplexer works and how it communicates in labview. also mention the wait time and how it doesn't help (needs to be on labview side) ie it doesn't help 'fix' electrical noise as it is a pre measure delay. also include a noise analysis - measure with and without and see what the difference is.

Appendix C

Igor Wavemetrics Analysis Code

The analysis component of the experiment is done primarily through the Igor Wavemetrics. The website contains the complete support on how to use the program. More importantly, a complete manual is always available for necessary help. Within the program, it is possible to obtain help on various topics by use of the command line and command 'usehelptopic"<topic>"'. Igor is quite versatile in what can be done and to that end has a steep learning curve. This section will give a brief description on the user functions coded into the most recent analysis program.

Several permutations of this analysis program were originally in place but did not readily support multiple sets of experiments effectively. Previously, one would have to analyse each data set individually which would then have to be saved manually often leading to results that were mislabelled or lost due to the creation of many different files. Furthermore, information was often lost between each step making backtracking very tedious. The new analysis program keeps track of much more information as well as allowing multiple experiments to be loaded in. Furthermore, additional analysis functions written into the program allow for seamless plotting of multiple sets of data.

The most recent version is 'AnalysisVer100(.pxp)' and is located within the lab dropbox folder 'root\PHY130-Rsearch\IgorPrograms'. This experiment should be a clean version of the program with no specific data from any measurements. The development of this analysis program is still ongoing and will undoubtedly change and improve as time progresses. Functions within the item should be documented as functions are added or updated.

To begin, several important windows are first discussed. The **Procedure Window** (Ctrl+M) contains the coding for the user functions discussed below. On the bottom left of the window, a pulldown menu 'Procedures' gives the option 'Go to function...' allowing quick navigation to any of the functions. The **Command Window** (Ctrl+J) is where both user defined functions as well as built-in functions can be called. Lastly the **Data Browser** is a graphic hierarch layout of all the saved information loaded into the current program. There is no hotkey for this but can be opened through the 'Data' menu or 'Windows' menu.

.nfo, .log.dat, .avg.dat files

These three items are necessary before beginning to perform any analysis through the program. The content in each file must be tab delimited for proper loading into the analysis program. The names of these items must be identical minus the format identifiers. The typical name format for the files follow <year>-<month>-<day> _ <description> *e*. Here is an example of what the file names should look like:

2012-04-05_FQD_MF_C_20-33K.log.dat
2012-04-05_FQD_MF_C_20-33K.avg.dat
2012-04-05_FQD_MF_C_20-33K.nfo

The .nfo file is a key file necessary for the data files to be properly loaded into the analysis program. This file contains key pieces of information regarding the dilatometer and material. These are required for proper analysis as the user functions are reliant of them. This file should be generated during the data acquisition (LabView) portion of the experiment but can always be created if necessary. Here is a sample of what the .nfo file should look like:

Material	Channel	L0	Cmax	Aeff	Device
MF_A	1	1.062	10	270	Quartz
TTO	3	0.420	85	105	Silver

The material is a user defined name and must be the same for any material that is to be plotted with one another. For formatting purposes, do not use - in the name as it causes plotting issues later on. The channel refers to the multiplexer channel and is used mostly in the background for correctly moving data sets. For single non-multiplexer measurements, such as pumped probe measurements, this should be default to 1. The sample length L0 is the length of the sample in millimetres (mm). The Cmax is the value used to characterize the tilt either by Cmax (in the silver dilatometer) or tilt parameter (for the fused quartz dilatometer). The reason why this is serves two purposes is because the tilted plate equation for each dilatometer is different and thus have two different tilting parameters. The value for Cmax is in picofarads (pF) while the value for tilt is in micrometers (μm). The effective area (Aeff) is measured in milimeters squared (mm^2). The device specifies which tilted plate equation is used as well as the relation between capacitance change and length change.

The data acquired from LabView comes in two files; the raw data (.log.dat) and the average data (.avg.dat). Both these files are formatted very similarly having the same column names and order. The raw data stores **all** the data made during the experiment while the average data stores the values of the measurement window outlined on the LabView side of the experiment. Typically both of these files are filled in a similar manner with the exception of DT experiments where a single measurement window is typically used leading to a useless average file. Addressing this will be discussed later.

Column names within the files must be correctly labelled for analysis. Typically, these files should be correctly formatted already and should not need to be modified. However, if they are not, ensure that the first columns are titled (in order); Time, Temp, followed by Capacitance_<channel> and Loss_<channel>. Columns thereafter may be additional capacitance/loss channels followed by additional saved information such as magnetic field or additional thermometers.

Lastly, loading older data from previous versions can be tricky as the formatting can often be incorrect. Common errors from loading old files can be from:

- Non-tab delimitation
- Incorrect column names
- Files mislabelled/misplaced
- Missing information within .nfo file

Loading, Listing and Removing Data

With the proper files, data can now be loaded into the analysis program. Using the function 'GetData()', a browsing window will ask to locate the .nfo file you wish to load. When this .nfo file is selected, the corresponding raw data file (.log.dat) and average data file (.avg.dat) are loaded in. These data files should be in the same location as the .nfo file. If they are not, the program will ask if you want to manually locate the files. If the files are loaded in correctly, a new folder will be created within the root directory of the data browser in Igor titled by the date followed by a number. This allows multiple experiments from a single day to be loaded in without overwriting one another. If an identical .nfo file is loaded, the program will prompt a confirmation to overwrite. The folder created in the root of the data browser will be referred to an experiment folder as it contains all relevant information of a single experimental run. The function will continue to prompt for .nfo files after one is loaded but can be cancelled by simply hitting the cancel button.

Within the experiment folder, three folders should be present; ExperimentInfo, RawData and AvgData. These three contain the loaded information from the three files outlined above. Additionally, the ExperimentInfo folder contains extra information such as the originating path and file name of the experiment. This is quite beneficial should the need for backtracking arise. Fig. C.1 is an example of what the data browser should look like if data is successfully loaded.

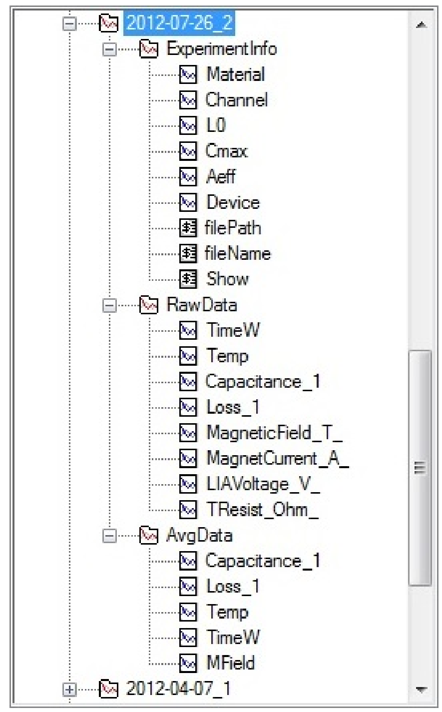

Figure C.1: Example of a typical Data Browser with loaded information in Igor

It is possible to list all folders within the data browser root directory using the function ‘list(<n>)’ where $n = 0, 1$. An input of 0 will give the short list of all experiment and their original .nfo file names while an input of 1 will give further details from within the .nfo file itself. Files which do not have an associated .nfo file are listed but marked with ‘Unknown file association’. Lastly, a number is given to each folder which is the associated index to that experiment. This index can change when moving or removing experiment folders but use of the ‘list’ function will give you the current index.

Removing experiment folders is simple as it can be deleted directly from the Data Browser. However, if plots or tables pertaining to the experiment is open, it will be unable to delete the folder. The function ‘ClearPlots(<index>, “<Material>”)’ is used to clear the plots generated by the user defined plotting functions. There are two plot functions; single and material. To clear single plots, specify the index followed by the material. To clear material plots, set the index to -1 and specify the material. The input <Material> must be in quotes as it is a string input. Clearing tables can be done using the function ‘Clear(1)’. Be aware that an input of -1 will do a full program clear excluding the user functions while an input of 0 will clear **all** plots.

Calculating and Plotting

Once an experiment is properly loaded, calculating the thermal expansion coefficient or magnetostriction from the AvgData is next. Using 'Calc(<index>,<mode>)' the thermal expansion coefficient (mode = 1) or magnetostriction (mode = 2) is computed using a first order differentiation approach. The plate separation, thermal expansion and thermal expansion coefficient differentiation are also calculated during this process. For each channel, a new folder is created within the experiment folder labelled following the format: <material> Chan <channel>.

In the event of a DT experiment, no usable information in AvgData is present. To fix this, the function 'avgdata(<index>,<window>)' is used to generate AvgData waves. The window input is the time window (in minutes) which the data is averaged.

Once this is done, plotting can now be done. The two plotting functions are 'PlotSingle(<index>,"<material>", <mode>)' and 'PlotMaterial("<material>")'. PlotSingle will bring up plots pertaining to the specific material in the specific experiment. The plots are: Capacitance and Temperature vs. Time, Capacitance and Separation vs. Temperature/MagField, Thermal expansion/Magnetostriction vs. Temperature and Alpha/Lambda vs. temperature.

The function 'PlotMaterial("<material>") will amalgamate all the results a material into several plots. The plots are: Separation vs. Temperature, Capactiance vs. Temperature and Thermal expansion coefficient vs. Temperature. These functions are sufficient in terms of analysing acquired data. Additional functions with documentation are outlined in the procedure window with the rest of the functions.

Appendix D

Fused Quartz Dilatometer Schematic Drawings

Presented in this section are all the schematics for the fused quartz dilatometer as well as the schematics for associated components such as the dilatometer base as well as shielding unit. Full assembly detail is outlined in section 3.3.

PARTS LIST			
ITEM	QTY	PART NUMBER	MATERIAL
1	1	BottomPlate	Fused Quartz
2	1	BottomWall	Fused Quartz
3	1	TopPlate	Fused Quartz
4	1	TopWall	Fused Quartz
5	2	QuartzSpring	Fused Quartz

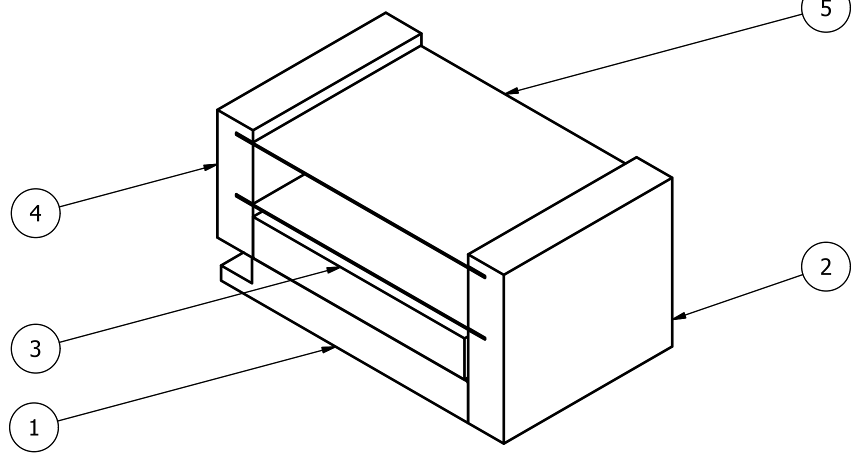

DRAWN BY KEVIN LIU	ROB HILL GROUP LOW TEMPERATURE II	
EXTENSION 32166		
CREATED 17/01/2012	TITLE	
MAT'L		
QTY		
PRIMARY UNITS METRIC	SIZE A	FILE NAME Dilatometersolo.iam REV
	SCALE	SHEET 1 OF 8

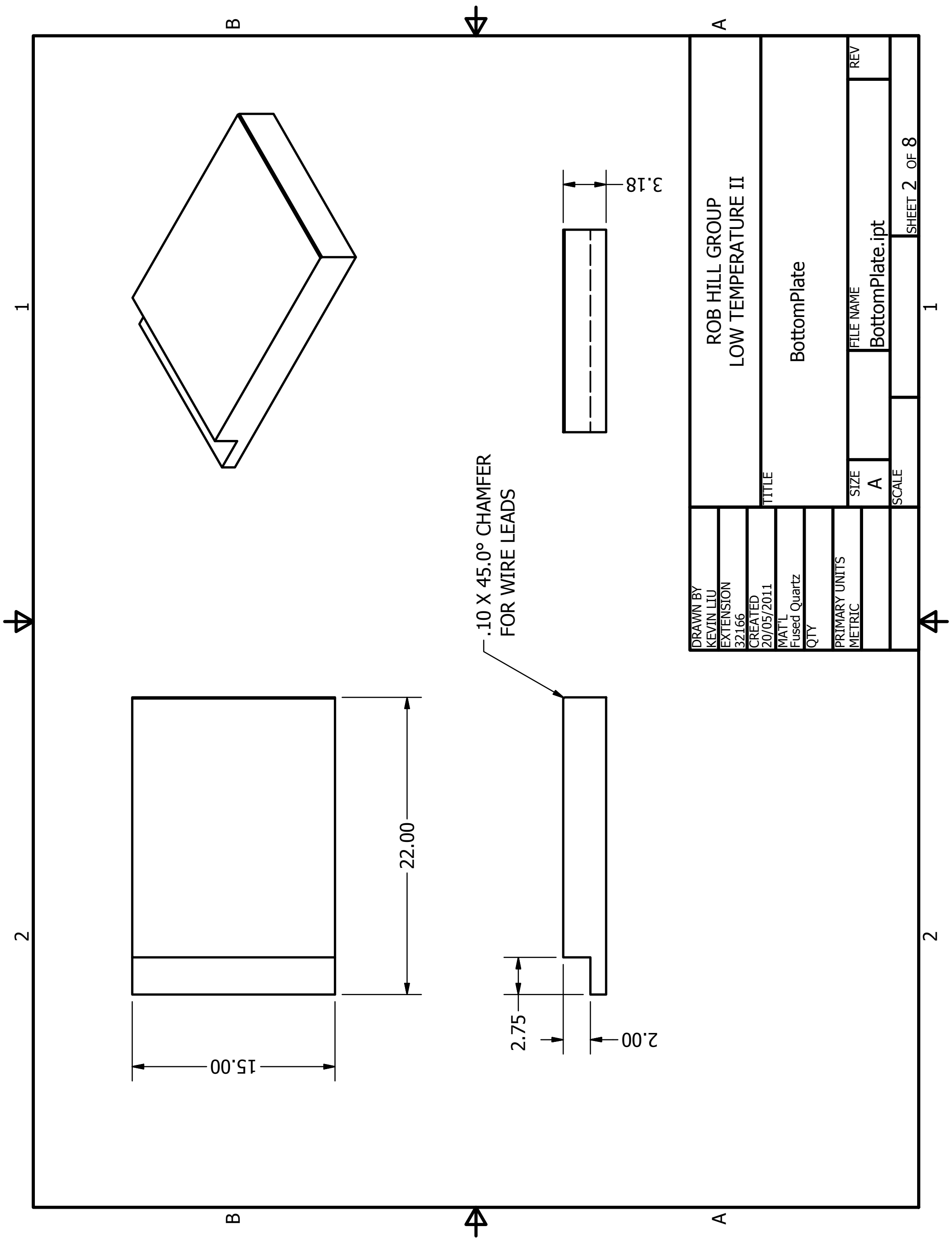
ROB HILL GROUP
LOW TEMPERATURE II
TITLE
BottomPlate
SIZE
A
FILE NAME
BottomPlate.ipt
REV
SCALE
SHEET 2 OF 8
DRAWN BY
KEVIN LIU
EXTENSION
32166
CREATED
20/05/2011
MAT'L
Fused Quartz
QTY
PRIMARY UNITS
METRIC
.10 X 45.0° CHAMFER
FOR WIRE LEADS
22.00
15.00
2.75
2.00
3.18
1
2
A
B

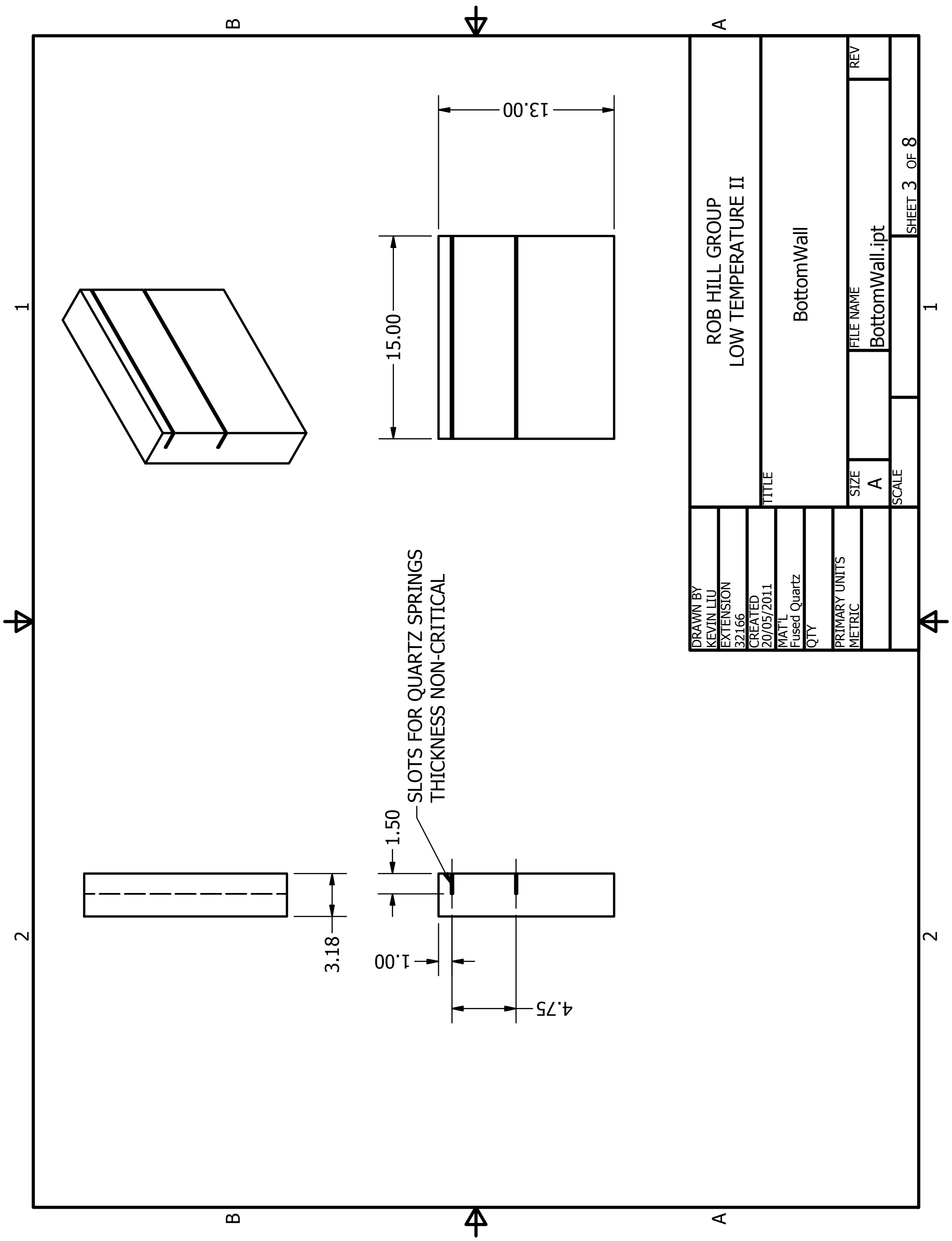
ROB HILL GROUP
LOW TEMPERATURE II
TITLE
BottomWall
SIZE
A
FILE NAME
BottomWall.ipt
REV
SCALE
SHEET 3 OF 8
DRAWN BY
KEVIN LIU
EXTENSION
32166
CREATED
20/05/2011
MAT'L
Fused Quartz
QTY
PRIMARY UNITS
METRIC
SLOTS FOR QUARTZ SPRINGS
THICKNESS NON-CRITICAL
13.00
15.00
1.50
3.18
1.00
4.75

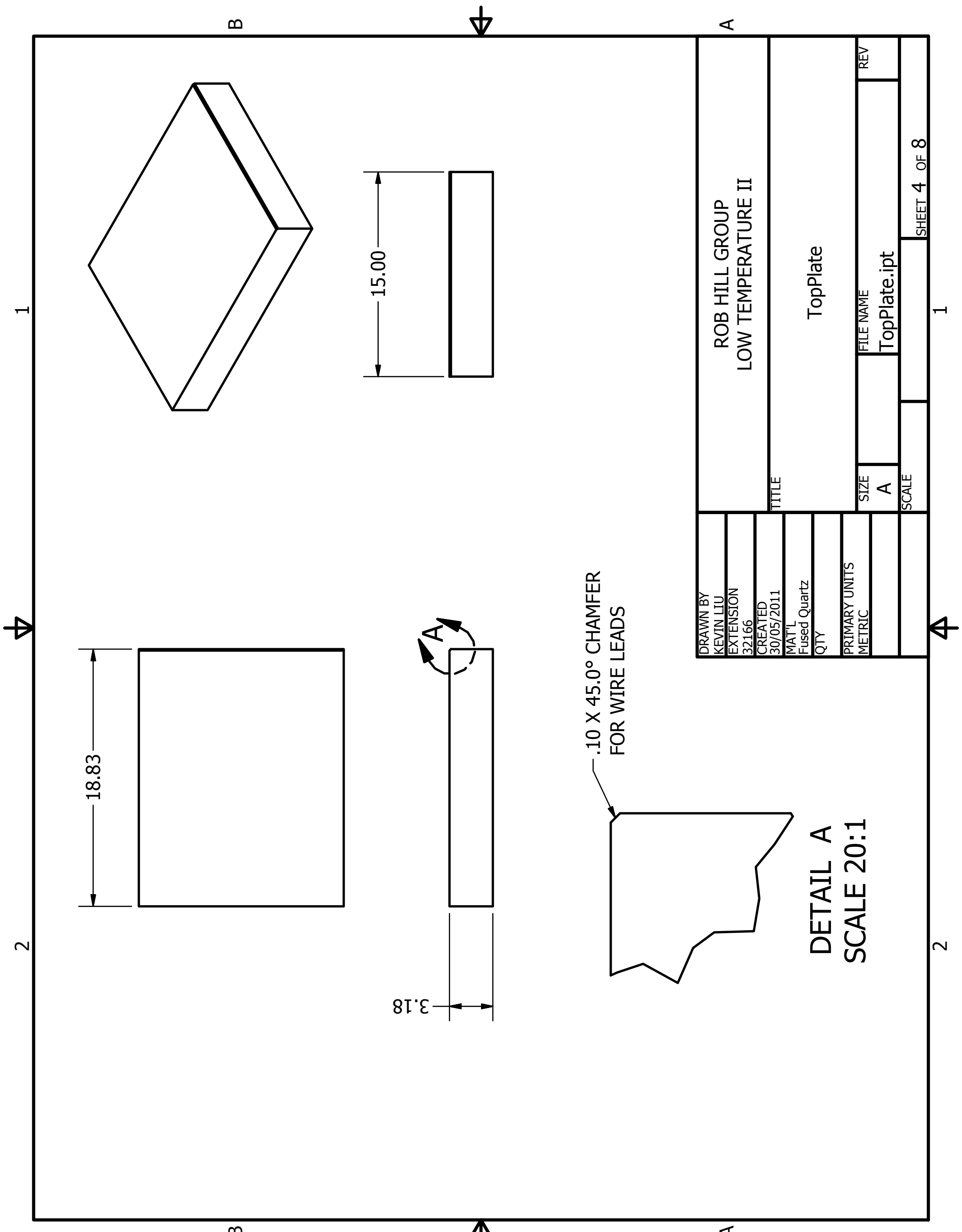

15.00
18.83
3.18
A
.10 X 45.0° CHAMFER
FOR WIRE LEADS
DETAIL A
SCALE 20:1
ROB HILL GROUP
LOW TEMPERATURE II
TITLE
TopPlate
SIZE
A
FILE NAME
TopPlate.ipt
REV
SCALE
SHEET 4 OF 8
DRAWN BY
KEVIN LIU
EXTENSION
32166
CREATED
30/05/2011
MAT'L
Fused Quartz
QTY
PRIMARY UNITS
METRIC

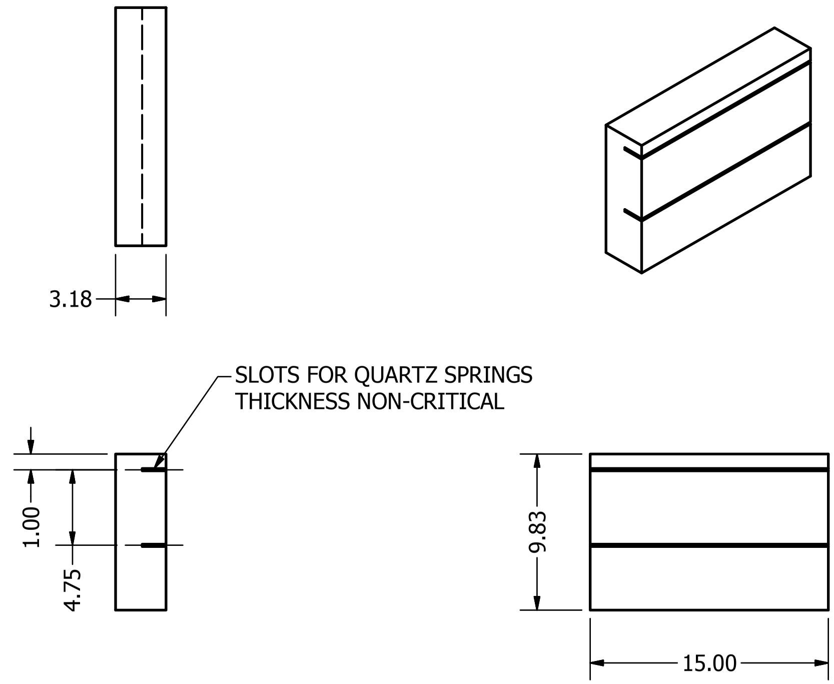

DRAWN BY KEVIN LIU	ROB HILL GROUP LOW TEMPERATURE II			
EXTENSION 32166				
CREATED 20/05/2011	TITLE TopWall			
MAT'L Fused Quartz				
QTY				
PRIMARY UNITS METRIC	SIZE A		FILE NAME TopWall.ipt	REV
	SCALE		SHEET 5 OF 8	

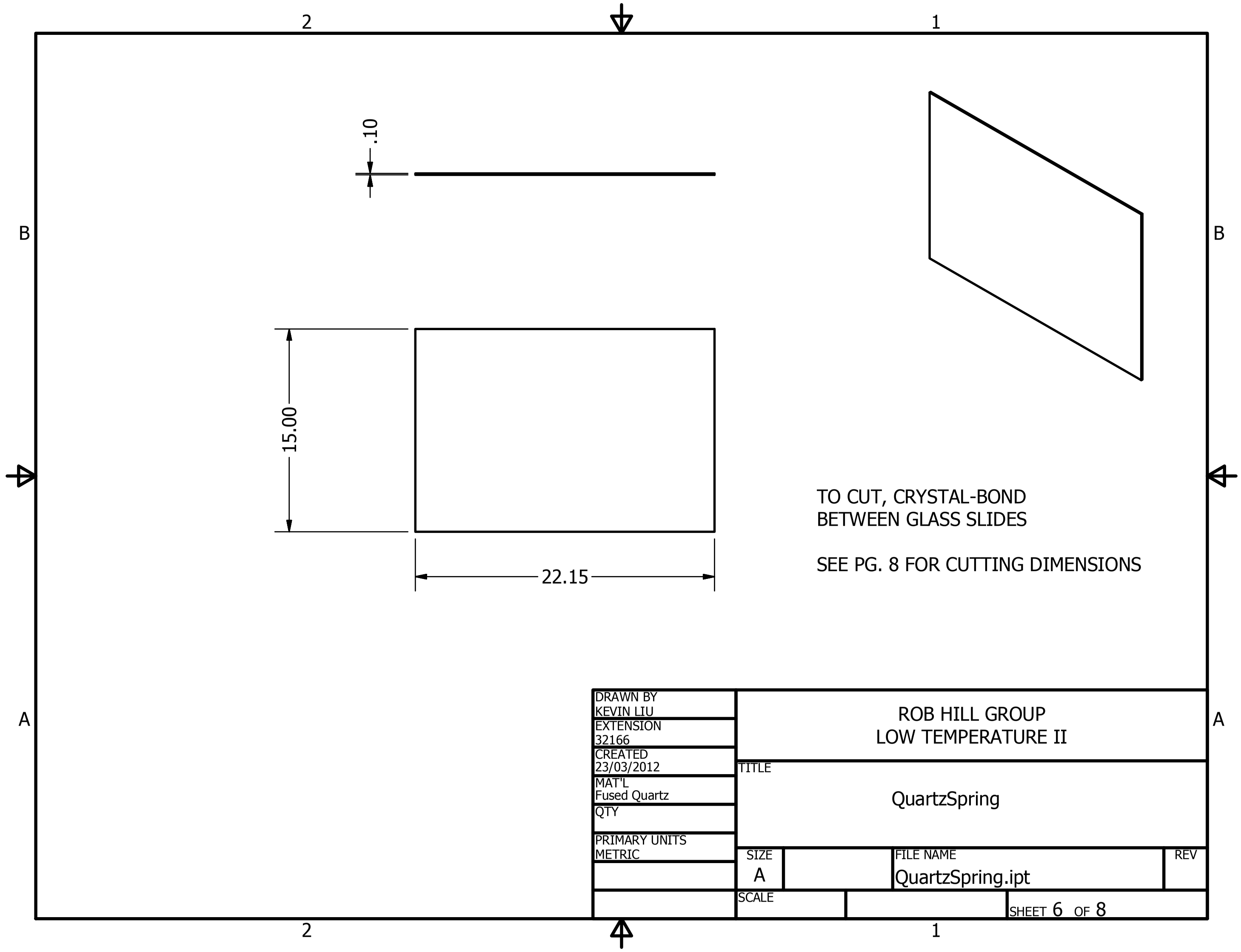
2
1
B
A
.10
15.00
22.15
TO CUT, CRYSTAL-BOND
BETWEEN GLASS SLIDES
SEE PG. 8 FOR CUTTING DIMENSIONS
DRAWN BY
KEVIN LIU
EXTENSION
32166
CREATED
23/03/2012
MAT'L
Fused Quartz
QTY
PRIMARY UNITS
METRIC
ROB HILL GROUP
LOW TEMPERATURE II
TITLE
QuartzSpring
SIZE
A
FILE NAME
QuartzSpring.ipt
REV
SCALE
SHEET 6 OF 8

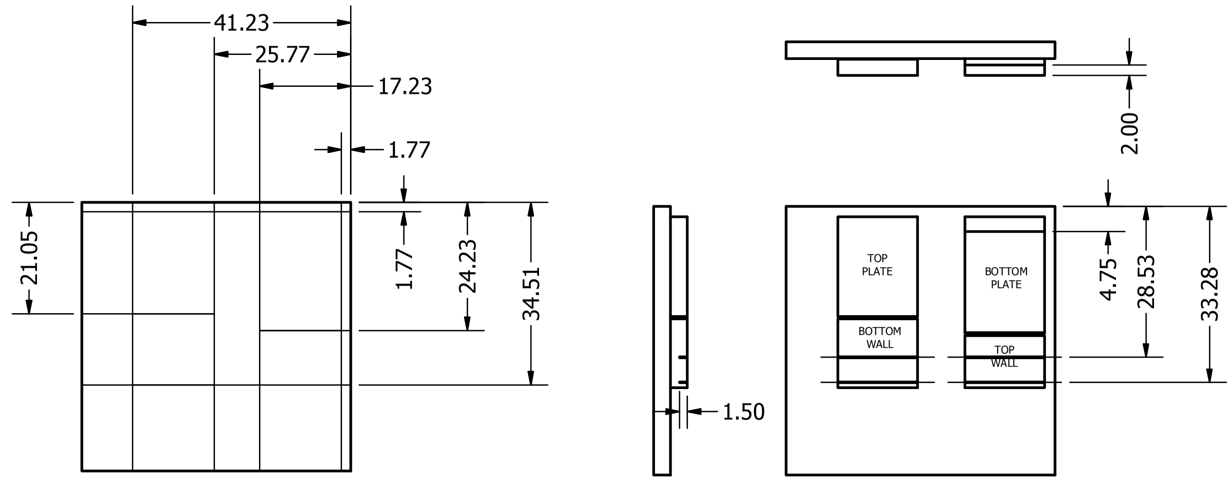

THIS IS THE REFERENCE FOR CUTTING
THE COMPONENTS OUT OF THE STOCK
QUARTZ WINDOW 2"X2"X1/8"
POSITIONED WITH TOP RIGHT CORNER
FLUSH TO ALUMINUM PLATE CORNER

DIMENSIONS ACCOUNT FOR CUTTING WIDTH OF 0.050"
ADJUST ACCORDINGLY

DRAWN BY KEVIN LIU	ROB HILL GROUP LOW TEMPERATURE II
EXTENSION 32166	
CREATED 18/01/2012	TITLE Component Cutting Configuration
MAT'L Default	
QTY	
PRIMARY UNITS METRIC	SIZE A / FILE NAME QuartzStock.ipt / REV
	SCALE / SHEET 7 OF 8

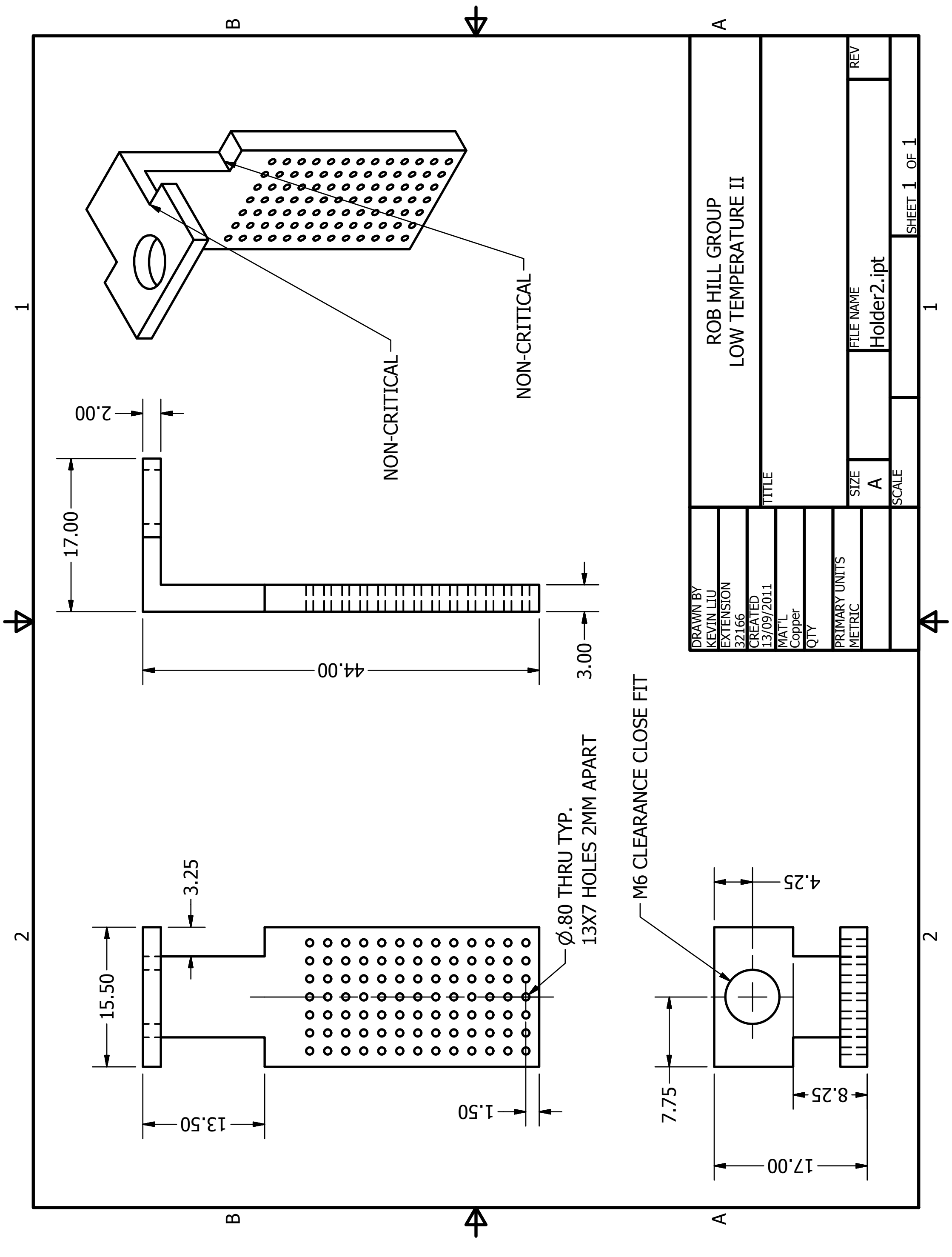

ROB HILL GROUP
LOW TEMPERATURE II
TITLE
DRAWN BY
KEVIN LIU
EXTENSION
32166
CREATED
13/09/2011
MAT'L
Copper
QTY
PRIMARY UNITS
METRIC
SIZE
A
SCALE
FILE NAME
Holder2.ipt
SHEET 1 OF 1
REV
NON-CRITICAL
NON-CRITICAL
Ø.80 THRU TYP.
13X7 HOLES 2MM APART
M6 CLEARANCE CLOSE FIT
2.00
17.00
44.00
3.00
3.25
15.50
13.50
1.50
4.25
7.75
8.25
17.00

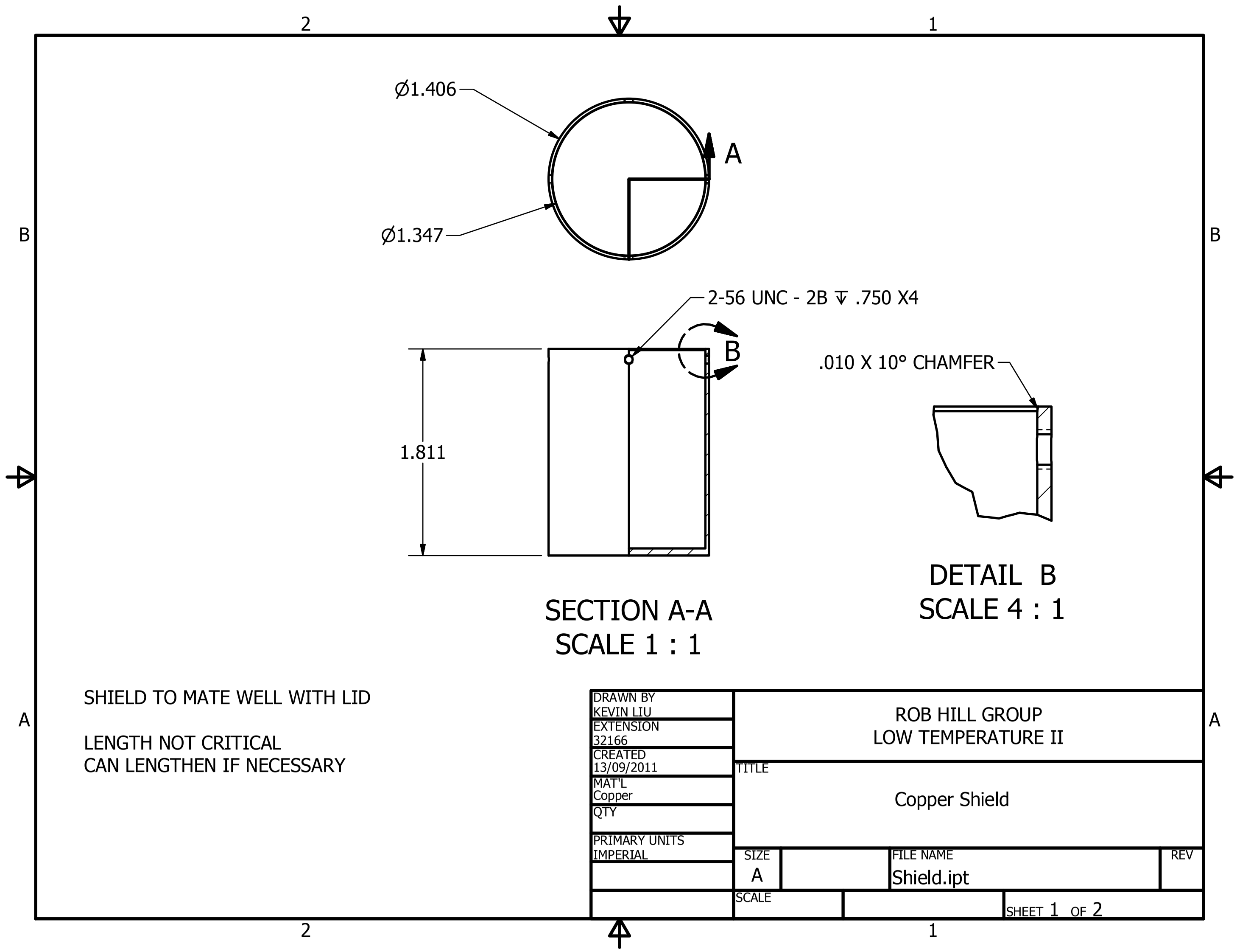
Ø1.406
Ø1.347
A
2-56 UNC - 2B ↧ .750 X4
B
1.811
.010 X 10° CHAMFER
SECTION A-A
SCALE 1 : 1
DETAIL B
SCALE 4 : 1
SHIELD TO MATE WELL WITH LID
LENGTH NOT CRITICAL
CAN LENGTHEN IF NECESSARY
DRAWN BY
KEVIN LIU
EXTENSION
32166
CREATED
13/09/2011
MAT'L
Copper
QTY
PRIMARY UNITS
IMPERIAL
ROB HILL GROUP
LOW TEMPERATURE II
TITLE
Copper Shield
SIZE
A
FILE NAME
Shield.ipt
REV
SCALE
SHEET 1 OF 2

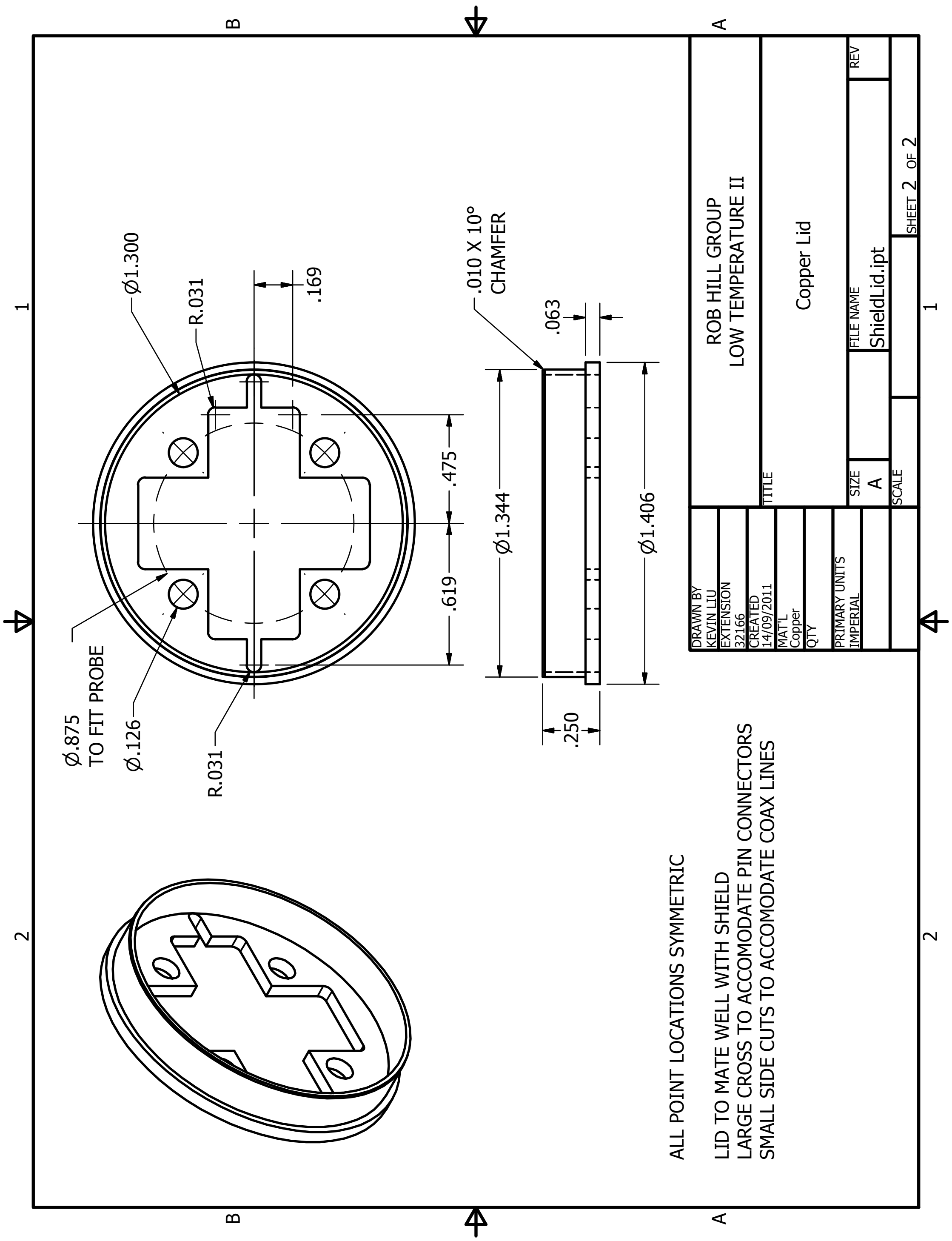
Ø1.300
R.031
.169
.010 X 10°
CHAMFER
.063
.475
.619
Ø1.344
Ø1.406
Ø.875
TO FIT PROBE
Ø.126
R.031
.250
ALL POINT LOCATIONS SYMMETRIC
LID TO MATE WELL WITH SHIELD
LARGE CROSS TO ACCOMODATE PIN CONNECTORS
SMALL SIDE CUTS TO ACCOMODATE COAX LINES
ROB HILL GROUP
LOW TEMPERATURE II
TITLE
Copper Lid
DRAWN BY
KEVIN LIU
EXTENSION
32166
CREATED
14/09/2011
MAT'L
Copper
QTY
PRIMARY UNITS
IMPERIAL
SIZE
A
FILE NAME
ShieldLid.ipt
REV
SCALE
SHEET 2 OF 2

Appendix E

Copper Dilatometer Schematic Drawings

In this section, the newest dilatometer schematics are shown. As discussed, this design is still in the prototype phase however the principle of this design is quite elegant and could be the next design for capacitive dilatometry.

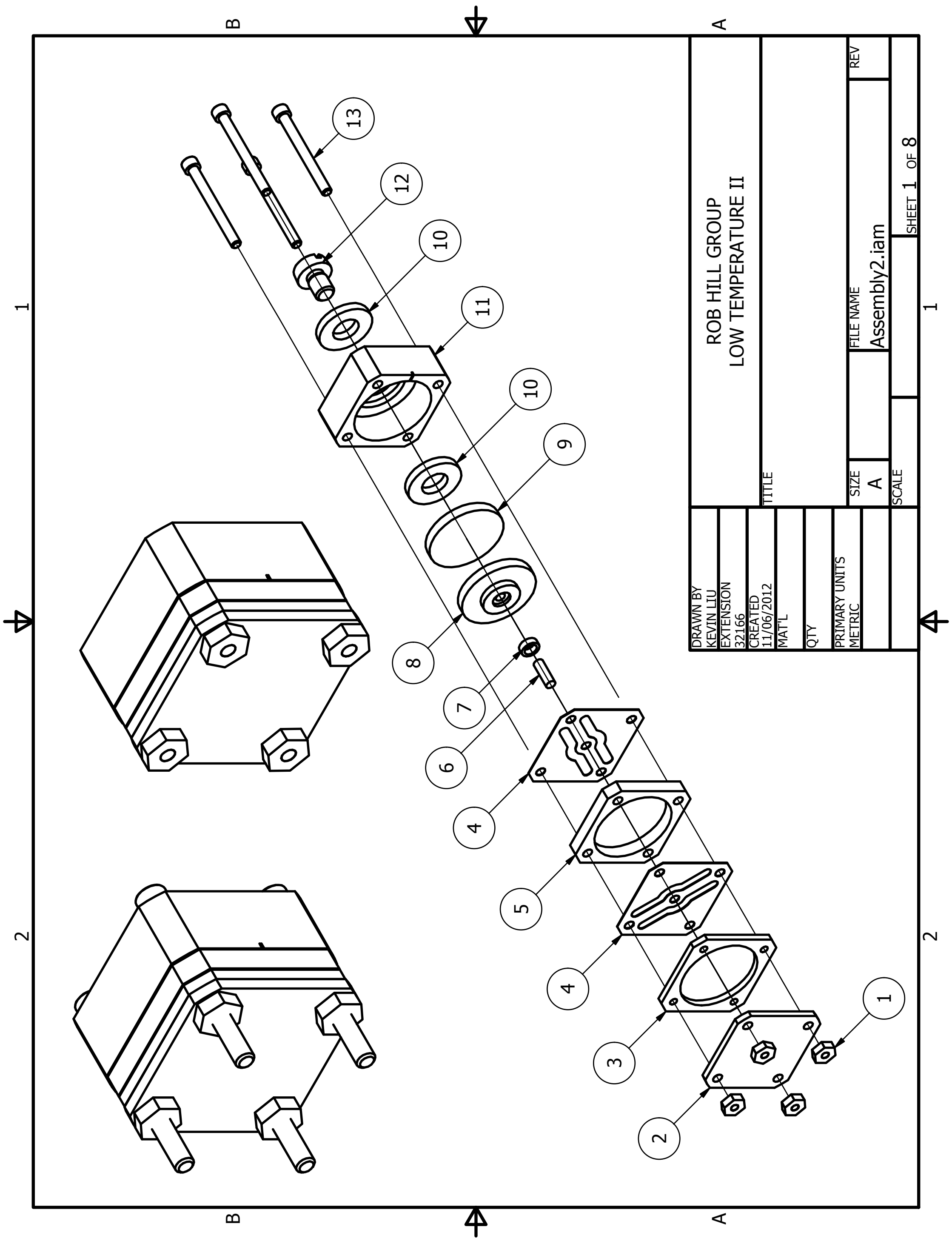
ROB HILL GROUP
LOW TEMPERATURE II
TITLE
SIZE A
SCALE
FILE NAME Assembly2.iam
SHEET 1 OF 8
REV
DRAWN BY KEVIN LIU
EXTENSION 32166
CREATED 11/06/2012
MAT'L
QTY
PRIMARY UNITS METRIC

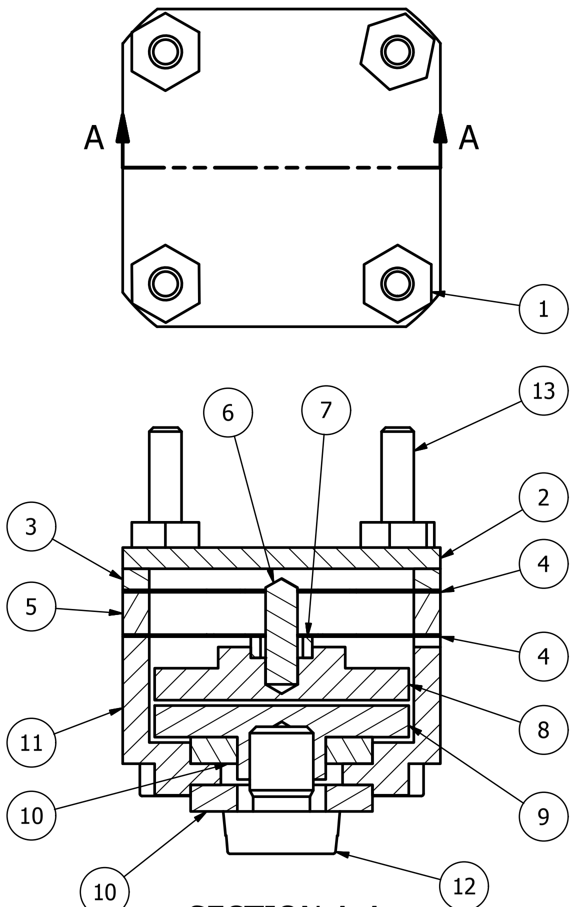

SECTION A-A
SCALE 4 : 1

PARTS LIST			
ITEM	QTY	PART NUMBER	MATERIAL
1	4	0-80 Low Profile Nut	Brass
2	1	TopShell	Copper
3	1	CompressionRing	Copper
4	2	SpringSingle	BeCu
5	1	SpringSeparator	Copper
6	1	TopPost	Sapphire
7	1	TopRing	Sapphire
8	1	TopPlate	Copper
9	1	BottomPlate	Copper
10	2	BottomSapphire	Sapphire
11	1	BottomShell	Copper
12	1	M3 x 4 Screw	Brass
13	4	0-80 UNF Screw	Brass

DRAWN BY KEVIN LIU	ROB HILL GROUP LOW TEMPERATURE II
EXTENSION 32166	
CREATED 11/06/2012	TITLE
MAT'L	
QTY	
PRIMARY UNITS METRIC	SIZE A · FILE NAME Assembly2.iam · REV
	SCALE · SHEET 2 OF 8

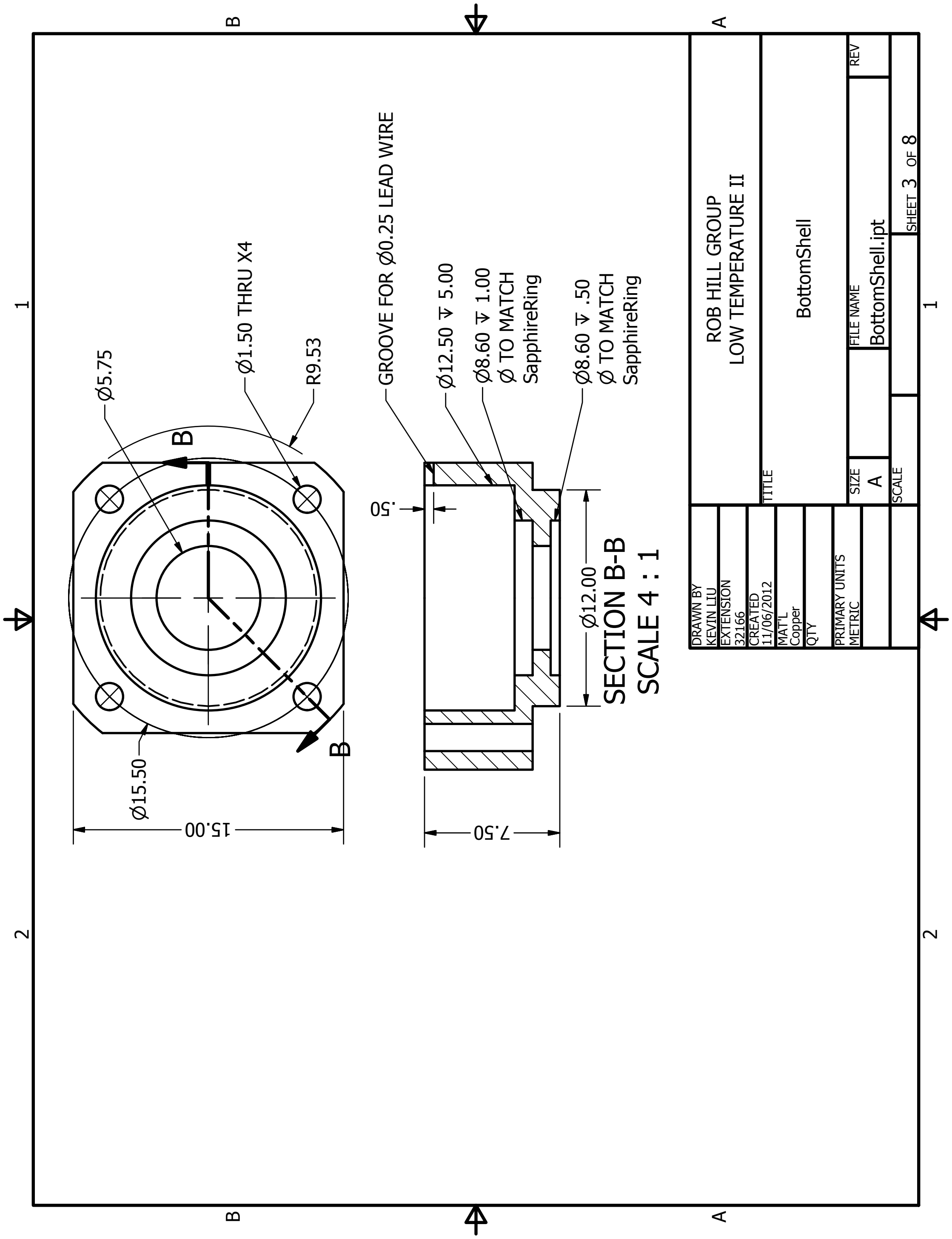

Ø5.75
Ø1.50 THRU X4
R9.53
GROOVE FOR Ø0.25 LEAD WIRE
Ø12.50 ↧ 5.00
Ø8.60 ↧ 1.00
Ø TO MATCH
SapphireRing
Ø8.60 ↧ .50
Ø TO MATCH
SapphireRing
B
B
.50
Ø15.50
15.00
7.50
Ø12.00
SECTION B-B
SCALE 4 : 1
ROB HILL GROUP
LOW TEMPERATURE II
TITLE
BottomShell
FILE NAME
BottomShell.ipt
SIZE
A
SCALE
SHEET 3 OF 8
REV
DRAWN BY
KEVIN LIU
EXTENSION
32166
CREATED
11/06/2012
MAT'L
Copper
QTY
PRIMARY UNITS
METRIC

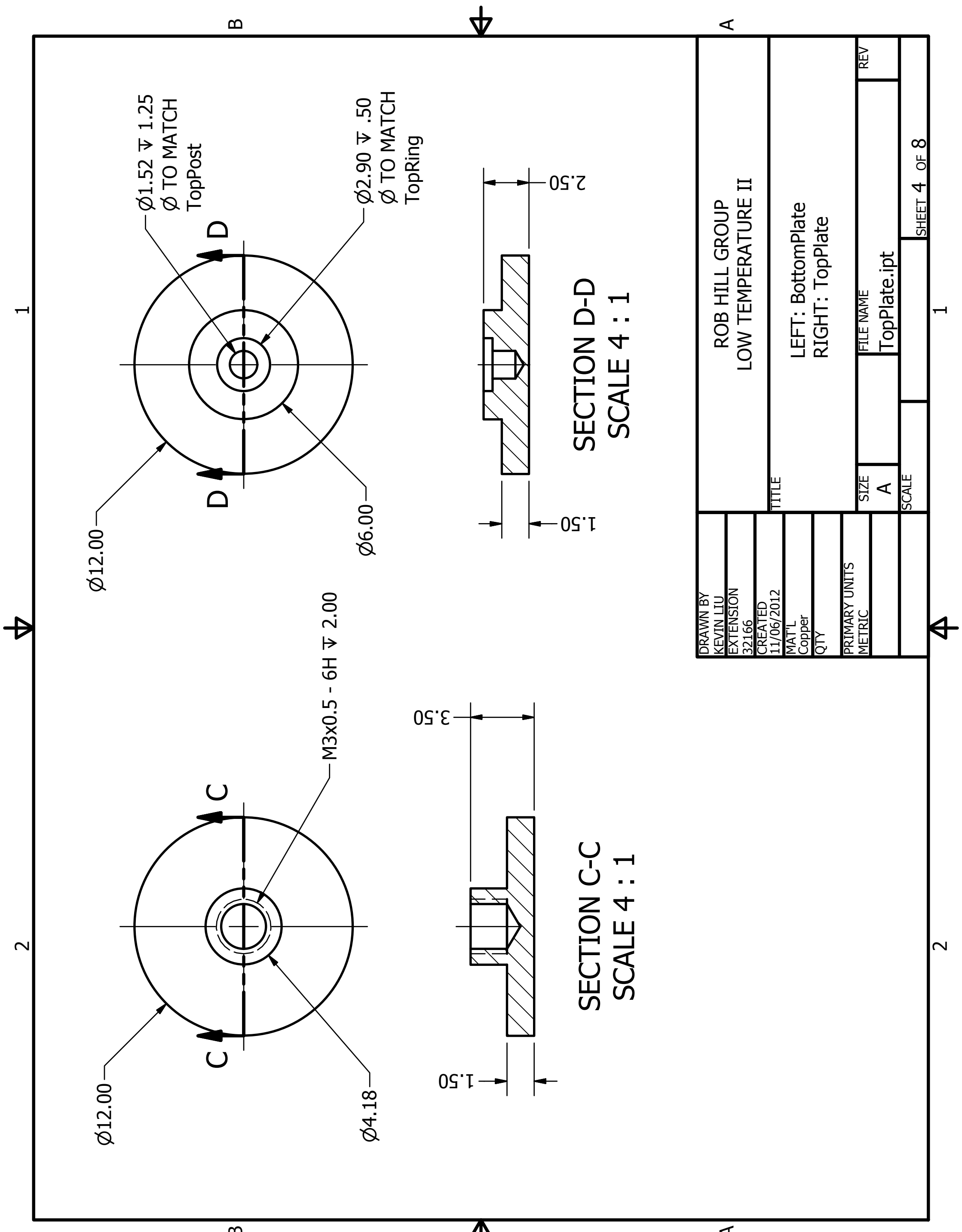

Ø1.52 ↧ 1.25
Ø TO MATCH
TopPost
Ø2.90 ↧ .50
Ø TO MATCH
TopRing
D
D
Ø12.00
Ø6.00
2.50
1.50
SECTION D-D
SCALE 4 : 1
M3x0.5 - 6H ↧ 2.00
C
C
Ø12.00
Ø4.18
3.50
1.50
SECTION C-C
SCALE 4 : 1
ROB HILL GROUP
LOW TEMPERATURE II
TITLE
LEFT: BottomPlate
RIGHT: TopPlate
DRAWN BY
KEVIN LIU
EXTENSION
32166
CREATED
11/06/2012
MAT'L
Copper
QTY
PRIMARY UNITS
METRIC
SIZE
A
SCALE
FILE NAME
TopPlate.ipt
SHEET 4 OF 8
REV

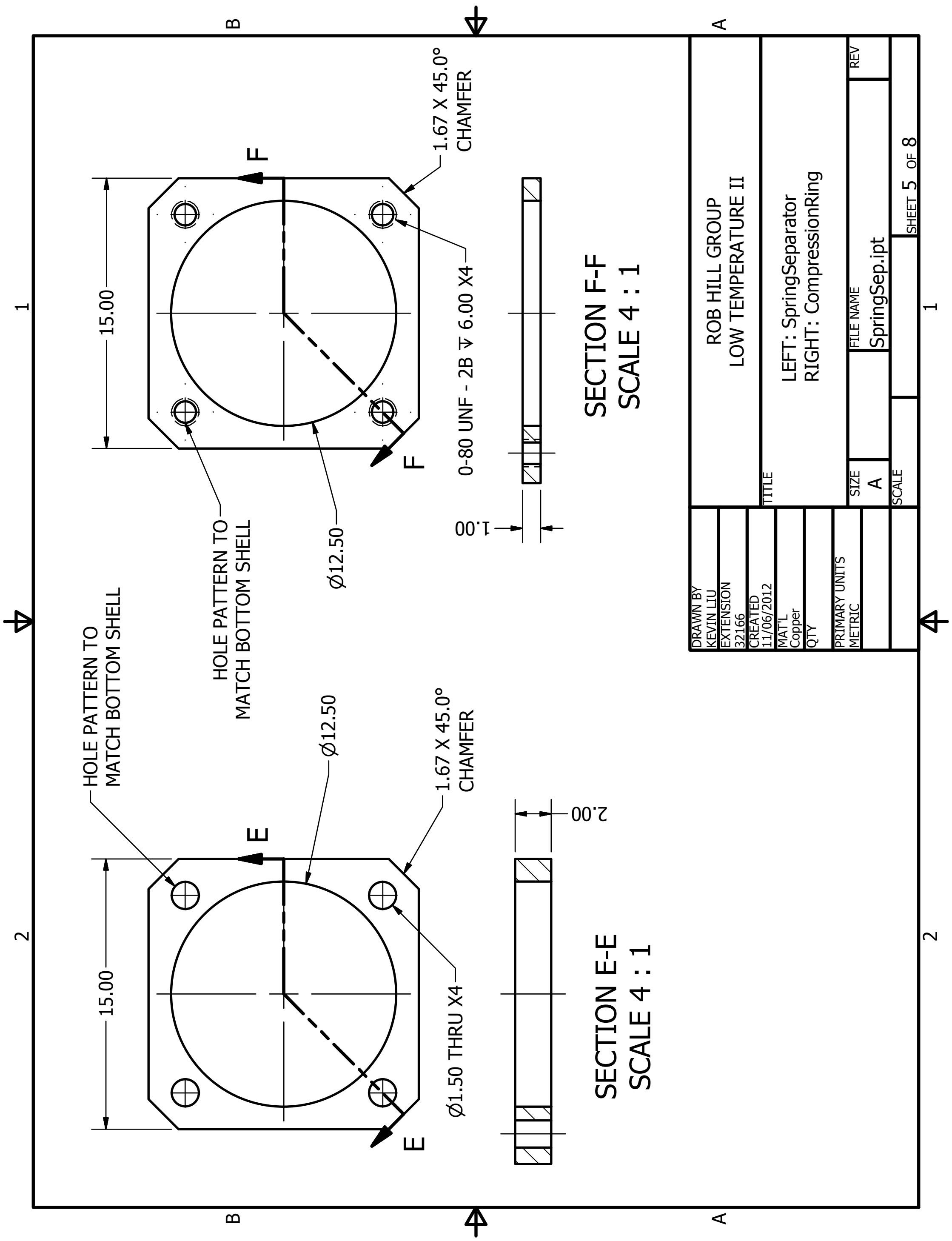

SECTION E-E
SCALE 4 : 1
SECTION F-F
SCALE 4 : 1
15.00
15.00
Ø12.50
Ø12.50
Ø1.50 THRU X4
0-80 UNF - 2B ↧ 6.00 X4
1.67 X 45.0°
CHAMFER
1.67 X 45.0°
CHAMFER
HOLE PATTERN TO
MATCH BOTTOM SHELL
HOLE PATTERN TO
MATCH BOTTOM SHELL
2.00
1.00
E
E
F
F
DRAWN BY
KEVIN LIU
EXTENSION
32166
CREATED
11/06/2012
MAT'L
Copper
QTY
PRIMARY UNITS
METRIC
ROB HILL GROUP
LOW TEMPERATURE II
TITLE
LEFT: SpringSeparator
RIGHT: CompressionRing
SIZE
A
FILE NAME
SpringSep.ipt
REV
SCALE
SHEET 5 OF 8

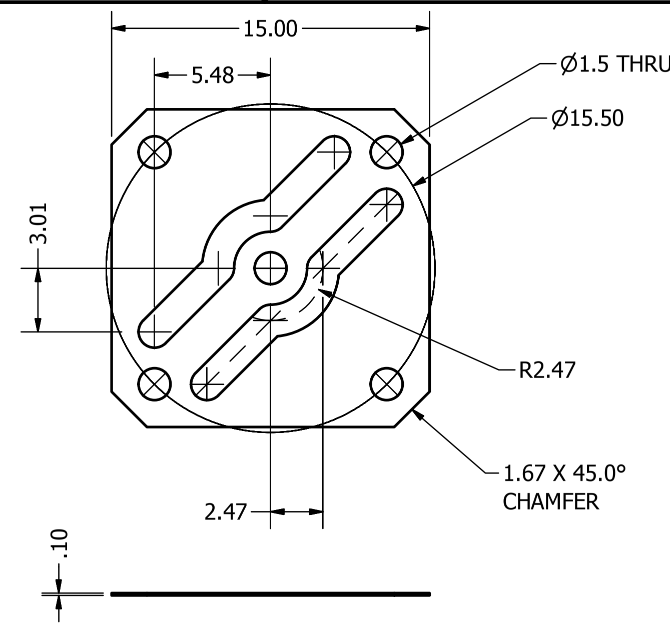

0.100MM THICK BECU STOCK

SLOTS CUT FROM GIVEN DIMENSIONS
ALL HOLE/POINT REFERENCES ARE SYMMETRIC
ALL CUTTING ACHIEVABLE BY SINGLE TOOL (0.06" BIT)

VACUUM ANNEAL 2 HOURS AT APPROX 200°C

DRAWN BY KEVIN LIU	ROB HILL GROUP LOW TEMPERATURE II
EXTENSION 32166	
CREATED 11/06/2012	TITLE
MAT'L Copper Beryllium	
QTY	
PRIMARY UNITS METRIC	SIZE A
	FILE NAME SpringSingle.ipt
	REV
	SCALE
	SHEET 6 OF 8

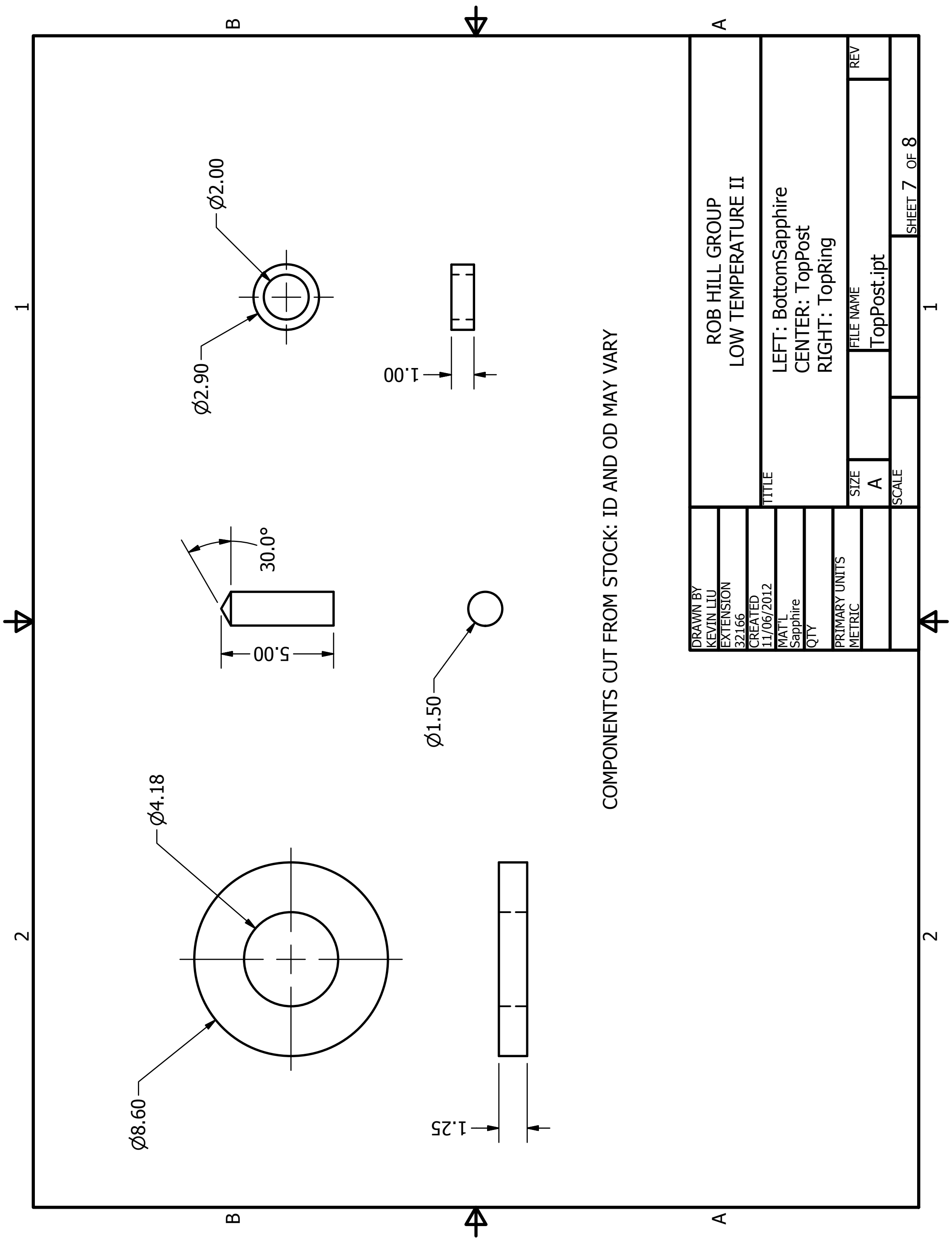
ROB HILL GROUP
LOW TEMPERATURE II
TITLE
LEFT: BottomSapphire
CENTER: TopPost
RIGHT: TopRing
FILE NAME
TopPost.ipt
SIZE
A
SCALE
SHEET 7 OF 8
REV
DRAWN BY
KEVIN LIU
EXTENSION
32166
CREATED
11/06/2012
MAT'L
Sapphire
QTY
PRIMARY UNITS
METRIC
COMPONENTS CUT FROM STOCK: ID AND OD MAY VARY
Ø2.00
Ø2.90
1.00
30.0°
5.00
Ø1.50
Ø4.18
Ø8.60
1.25

Appendix F

User Guides

The process of evaporating the silver onto the quartz plates is found here. The initial instructions were the instructions given from the 360/460 physics lab at the University of Waterloo for thin film evaporation. An extended guide was written by Steffanie Freeman covering the process in further detail. Additional observations will be noted here from experience evaporating. The preparation and curing guide for Stycast 2850 epoxy is also found here.

UNIVERSITY OF WATERLOO

Physics 360/371 - Experiment 19

VACUUM EVAPORATION OF DIELECTRIC INTERFERENCE FILTERS

References: Practical Vacuum Techniques; Brunner & Batzer, Chapter 2
Principles of Optics; Born & Wolf, Sect. 7.6.6
Thin Film Technology; Berry, Hall & Harris, Sect. 2.3, 2.4, 2.6, 3.6
Vacuum Deposition of Thin Films; L. Holland

Introduction: The purpose of the experiment is to familiarize students with vacuum systems and the techniques of vacuum evaporation, and simple optical measurements.

The basic principles of the Fabry-Perot interferometer can be easily extended to the case of an interference filter where a dielectric material is used to separate two semitransparent reflecting layers. These filters can be used to transmit a fairly narrow band of wavelengths in the visible spectrum. With vacuum evaporation techniques it is possible to prepare uniform and continuous dielectric films and metallic reflecting layers in the thickness range of hundreds of Angstroms. These relatively small thicknesses are required to attain semi-transparency of the reflecting coatings and low order interference to sufficiently separate the wavelengths transmitted.

1. Preparation:

Check the initial conditions of the system are as follows:

Main valve control	closed
Mains power	off
Leak valve	closed
Diffusion pump	off
Rotary pump	off
Air admittance	off

2. Turn on the cold water-cooling supply and turn the mains power to the coating unit on. Start the rotary pump by depressing the pump switch at the top of the control console. Now open the backing valve by turning the main valve control a quarter turn clockwise. Observe the Pirani guage and allow the pressure to drop below 0.3 mbar, once this is attained you may start the diffusion pump by depressing the switch. The diffusion pump oil will reach operating temperature in approx. 25 mins.

3. Carefully lift off the bell jar and place it in the holder. It is important that the rubber seal and sealing surfaces are kept clean. Turn on the frequency meter and check that the crystal oscillator used for sample thickness monitoring has a frequency within 200 KHz of 5 MHz. The relationship between deposition thickness (t), frequency change (?f) and density of evaporated material (?) is

$\Delta f = \frac{rt}{1.9}$	where ?f is in Hz ? is in gm/cc t is in angstroms	(i)

	Density	Melting Point	Refractive Index
Al	2.7 gm/cc	660° C	
Na_3AlF_6	2.9 gm/cc	1000° C	1.33

4. Prepare tungsten (W) and molybdenum (Mo) helix sources as described in appendix A and load as described with Al wire and Na_3AlF_6 powder. Mount the sources (2 of each) on the support posts. Measure distances between sources, slides and oscillator; then weigh and mount clean glass slides in position. Refer to appendix B.

5. Replace the bell jar, and the lucite implosion shield.

6. Pumpdown. Close the backing valve and open the roughing valve by rotating the main valve control one half-turn counter clockwise. Allow the pressure (Pirani gauge) to drop to at least 0.8 mbar. Turn off the oscillator and turn on the glow discharge by selecting the H.T. control and increase the current to a maximum of 20 as read off the meter. Once the glow has diminished, zero the potentiometer and turn off the H.T. control then return the main valve control to the backing position. SLOWLY open the H.V. Valve by turning it one half-turn clockwise. Switch on the Penning gauge and set to range 1. Range 2 may be selected as the pressure in the bell jar is reduced. Using great care when handling, you may now fill the cold trap with liquid nitrogen.

7. Using the source selector and LT control, evaporate 300 angstroms Al, 3000 angstroms of cryolite and 300 angstroms Al. Increase the potentiometer slowly at first for each source so it is allowed to outgas. During evaporation keep the pressure below 1×10^{-4} mbar with rates between 5 and 50 Hz per second as read on the oscillator frequency meter. Once you have the required thickness return the potentiometer to zero and select another source. For the sources listed in appendix A, depending on source load and condition, this corresponds to meter readings of:

Al	16-20 (10V)	40-50 (30V)
Cryolite	20-22 (10V)	50-55 (30V)

Once all evaporation is completed deselect the LT control and allow the sources and slides to cool for 5 minutes.

8. Close the H.V. valve by turning the valve control 180 degrees counter-clockwise to return it to the backing position. ONLY when this is completed should the air admittance switch be depressed. Carefully remove the bell jar and the prepared films.

9. Weigh the glass slides and verify the constant in the frequency equation, using

$$\text{constant} = \frac{W}{A\Delta f}$$

where: W is total weight evaporated

?f is total frequency change

A is area of the slide.

10. System off. Replace bell jar and turn off diffusion pump. Wait 30 mins, and then return main valve control to the closed position. Turn off the rotary pump and the mains power and close the valve on the cooling water supply.

11. Using the spectrophotometer - computer set-up, you may obtain transmission versus wavelength plots for your prepared filters as well as plots for several commercially prepared filters. (These plots can be prepared during the period you are pumping down and evaporating.) The control program "SPECT" is used. This is a comprehensive program which allows maximum flexibility in tailoring your output. A program flowchart is attached to illustrate the various features of this program.

12. Since the metallic reflecting layer absorbs some of the light, an effective phase shift occurs at the interface such that for 1st order

$$\frac{l_0}{2} = \frac{nh}{1-\frac{f}{p}}$$

where ?$_0$ is wavelength of transmitted peak intensity

h is thickness of dielectric

ø is effective phase shift

n is refractive index of dielectric

For 1st order reflection from thin metallic films at normal incidence

$$d = \frac{l}{F\left(1 - \frac{f}{p}\right)} \qquad \text{(Born and Wolf, Sect. 7.6.6)} \qquad \text{(iv)}$$

and $$F = \frac{p\sqrt{R}}{1 - R} \qquad \text{(Born and Wolf, Sect. 7.6.2)} \qquad \text{(v)}$$

where d is the width of the transmission peak at half intensity

R is reflectivity of the dielectric metal interface.

From your plot of optical transmission versus wavelength, determine the reflectivity of the dielectric metal interface.

Appendix A: Computer - Spectrometer usage

To operate the setup, you must first turn on the computer, printer, DVM's and the spectrometer. The control program will load automatically. When the CAL message on the spectrometer goes out, set the control switch (located on the bottom front of the unit) to the HOLD position. Use the MODE button to select %T.

To obtain:

i) Background:

- Ensure an **empty** sample holder is properly in place.
- Use the wavelength +/- keys to set the wavelength to 690 nm.
- Depress the Set Ref key (display should read 100%).
- Use the +/- keys to set wavelength to 325 nm **(wait** for a measurement to be displayed)
- Click on the read background button.
- Move the control switch to sweep (SWP). The background is now being recorded.

Note that the background only needs to be recorded once for the experiment.

ii) Filter Spectra:

- Set the control switch to HOLD
- Insert the filter in the appropriate holder and insert into the spectrometer.
- Set the wavelength (+/- keys) to the position of maximum intensity (as displayed on the MEASUREMENT readout). For the commercial filters this will be near the wavelength on the side of the filter, for your prepared filter you will have to "hunt" for the wavelength of maximum intensity.
- Depress the Set Ref key (display will read 100%)
- Set wavelength to 325 nm **(wait** until a reading is displayed).
- Click on read spectra, then switch to sweep (SWP)
- When wavelength reaches 900 nm the program will prompt you for a target filename. The path should be *C:\DATA\filespec.*

There are several other very intuitive options available to you in the program;

- Display Spectra (to screen). A good idea before you print.
- Print Spectra i.e. hard copy.
- Data from file: shows a list of all files in *C:\DATA* click on a file you wish to retrieve.

The Vacuum System

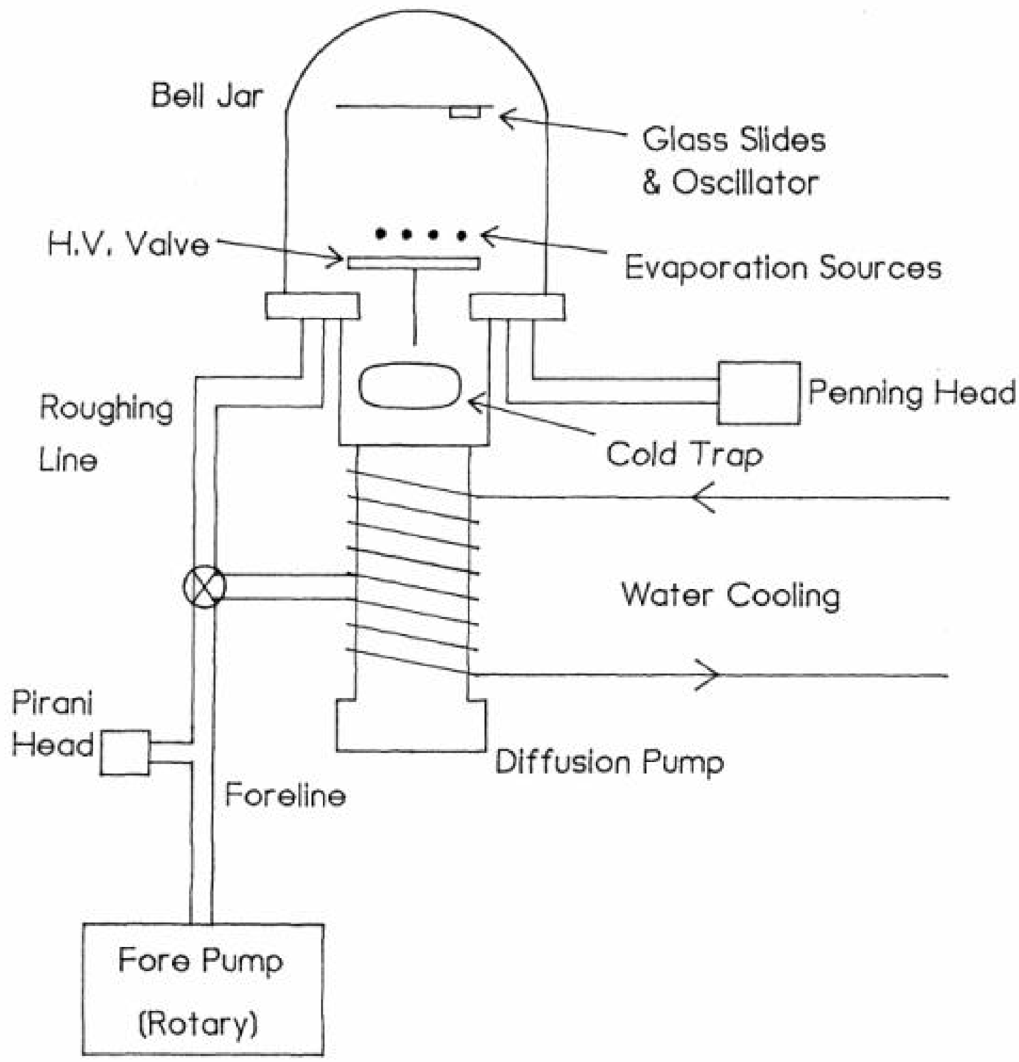

Evaporation Guide

$$t = \frac{1.9 * \Delta f}{\rho}$$

t : thickness of evaporated material to obtain
Δf: change in oscillation frequency of quartz crystal
ρ: density of material to be evaporated

For a description of how these types of vacuums work, visit http://tinyurl.com/4yttwfv

Step 1: The vacuum chamber allows you to put a maximum of three crucibles in the evaporator. They are labelled 1, 2 and 3, 1 being on the far left and 3 being on the far right. Insert the filled crucible(s) into a basket heater and place it in the chamber. Remember which slot(s) you have put your crucible(s) into. The ends of the basket heater attach by placing them between washers and tightening the screws going through the washers. (It is a good idea to place an extra crucible into the evaporator in case one of the heaters does not work.) Turn on the frequency output and check that the frequency is within 200 KHz of 5 MHz . If not, you will need to replace the crystal located in the box on the sample mounting stage.

Step 2: Make sure the arrow on the front handle is set to “backing”. If it is set to 'valves closed', turn the handle clockwise to select 'backing'. Turn off the return lines (with the yellow and orange tags) to the left of the evaporator by turning the black handles to sit perpendicular to the pipes. Turn on the rotary pump by pressing the 'rotary pump' button at the top end of the control panel. Let the pressure reach approximately .3 mbar before turning on the diffusion pump, labelled 'diff pump'. Allow the diffusion pump to heat up the oil for 30 minutes before proceeding to step 2.

Step 3: Begin to alternate between “roughing” and “backing” by turning the front handle to the corresponding positions (clockwise for backing, counter-clockwise for roughing, aka. keep the arrow on the front handle on the bottom half of the dial - switching with the arrow on the top half operates different controls). These should be switched every few minutes until a pressure below 10^{-1}T is reached on the top gauge. While it is set to roughing, you may turn on the button labelled “HT” at the bottom of the control panel and slowly turn up the dial to its left to a maximum of 20 as read off the guage. This will allow you to reach the appropriate pressure more quickly. You should see a purple glow appear as you turn up the dial (ionizing Nitrogen). Reduce the dial to zero after a few minutes and turn off the HT button before switching back to “backing”. Make sure you always turn this dial to zero before turning off the LT or HT buttons, or switching heaters.

Step 4: Once the appropriate pressure is reached, you should now open the return lines to the left of the evaporator. Now open the valves using the front handle, you will feel the handle pop out before you switch to open the valves, slowly turn the handle clockwise, you will see the valve open in the chamber. Fill the metal container to the left of the bell-jar with liquid nitrogen. Turn on the frequency output via the switch to the right of the digital reading. This will read the oscillation frequency of the quartz which determines the thickness deposited onto your sample.

Step 5: Turn the heater knob to the number corresponding to the crucible you wish to heat (1, 2 or 3). Then push the “LT” button and very slowly turn up the black dial until you reach a rate of frequency change which will allow your evaporated thickness to be achieved in a timely manner, around 10-30 minutes, depending on thickness. Once the desired frequency is reached, you may switch to another heater (remembering to turn down the dial to zero and shut off LT before switching) or, if finished, you can switch the handle back to the 'backing' position. Wait 5 minutes to let the sample cool, then press the air admittance button at the top of the control panel. You may now retrieve your sample.

Step 6: Turn off the diffusion pump by pushing the corresponding button at the top of the control panel. Wait approximately 30 minutes, then shut off the rotary pump and close the return lines.

Emerson & Cuming
a National Starch & Chemical Company

Internet Address:
www.emersoncuming.com

Technical Data Sheet

STYCAST® 2850 FT
Thermally Conductive Epoxy Encapsulant

Key Feature:	Benefit:
- Good thermal conductivity	• Dissipation of heat from embedded components
• Low coefficient of thermal expansion	• Low stress on embedded components

Product Description:

STYCAST 2850 FT is a two component, thermally conductive epoxy encapsulant that can be used with a variety of catalysts. It features a low coefficient of thermal expansion and excellent electrical insulative properties. The STYCAST 2850 FT Blue is recommended for use in high voltage applications where surface arcing or tracking is a concern.

Applications:

STYCAST 2850 FT is designed for encapsulation of components which need heat dissipation and thermal shock properties.

Instructions For Use:

Thoroughly read the information concerning health and safety contained in this bulletin before using. Observe all precautionary statements that appear on the product label and/or contained in individual Material Safety Data Sheets (MSDS).

To ensure the long term performance of the potted or encapsulated electrical / electronic assembly, complete cleaning of components and substrates should be performed to remove contamination such as dust, moisture, salt, and oils which can cause electrical failure, poor adhesion or corrosion in an embedded part.

Some filler settling is common during shipping or storage. For this reason, it is recommended that the contents of the shipping container be thoroughly mixed prior to use. Power mixing is preferred to ensure a homogeneous product.

Accurately weigh resin and hardener into a clean container in the recommended ratio. Weighing apparatus having an accuracy in proportion to the amounts being weighed should be used.

Blend components by hand, using a kneading motion, for 2-3 minutes. Scrape the bottom and sides of the mixing container frequently to produce a uniform mixture. If possible, power mix for an additional 2-3 minutes. Avoid high mixing speeds which could entrap excessive amounts of air or cause overheating of the mixture resulting in reduced working life.

To ensure a void-free embedment, vacuum deairing should be used to remove any entrapped air introduced during the mixing operation. Vacuum deair mixture at 1-5 mm mercury. The foam will rise several times the liquid height and then subside. Continue vacuum deairing until most of the bubbling has ceased. This usually requires 3-10 minutes. To facilitate deairing in difficult to deair materials, add 1-3 drops of an air release agent, such as ANTIFOAM 88, into 100 grams of mixture. Gentle warming will also help, but working life will be shortened.

Pour mixture into cavity or mold. Gentle warming of the mold or assembly reduces the viscosity. This improves the flow of the material into the unit having intricate shapes or tightly packed coils or components. Further vacuum deairing in the mold may be required for critical applications.

Properties of Material As Supplied:

Property	Test Method	Unit	Value
Chemical Type			Epoxy
Appearance	Visual		Black or blue liquid
Density	ASTM-D-792	g/cm^3	2.35 - 2.45
Brookfield Viscosity	ASTM-D-2393 5 rpm # 7	Pa.s cP	200 - 250 200,000 - 250,000

Choice of Curing Agents			
Curing agent	Catalyst 9	Catalyst 23 LV	Catalyst 11
Description	General purpose with good chemical resistance and physical strength.	Low color, low viscosity, long pot life. Excellent, thermal shock and impact resistance. Excellent low temperature properties and adhesion to glass.	Long pot life, excellent chemical resistance, good physical and chemical properties at elevated temperatures.
Type of cure	Room	Room	Heat
Viscosity Pa.s cP	0.080 to 0.105 80 to 105	0.020 to 0.030 20 to 30	0.035 to 0.060 @ 65 °C 35 to 60 @ 65 °C

Properties of Material As Mixed:

Property	Test Method	Unit	Value		
			Catalyst 9	Catalyst 23 LV	Catalyst 11
Mix Ratio - Amount of Catalyst per 100 parts of STYCAST 2850 FT		By Weight By Volume	3.5 8.5	7.5 17.5	4.5 9.5
Working Life (100 g @ 25°C)	ERF 13-70		45 minutes	60 minutes	>4 hours
Density	ASTM-D-792	g/cm^3	2.29	2.19	2.29
Brookfield Viscosity	ASTM-D-2393	Pa.s cP	58 58,000	5.6 5,600	64 64,000

Cure Schedule:

Cure at any one of the recommended cure schedules. For optimum performance, follow the initial cure with a post cure of 2-4 hours at the highest expected use temperature. Alternate cure schedules may also be possible. Contact your Emerson & Cuming Technical Representative for further information.

Temperature	Cure Time		
°C	Catalyst 9	Catalyst 23 LV	Catalyst 11
25	16-24 hr	16-24 hr	-
45	4-6 hr	4-6 hr	-
65	1-2 hr	2-4 hr	-
80			8-16 hr
100			2-4 hr
120			30-60 min

Properties of Material After Application:

Property	Test Method	Unit	Value		
			Catalyst 9	Catalyst 23 LV	Catalyst 11
Hardness	ASTM-D-2240	Shore D	96	92	96
Flexural Strength	ASTM-D-790	mPa psi	92 13,300	106 15,300	117 17,000
Compressive Strength	ASTM-D-695	mPa psi	155 22,500	120 17,400	193 27,900
Linear Shrinkage	ASTM-D-2566	cm/cm	0.002	0.003	0.002
Water Absorption (24 hours)	ASTM-D-570	%	0.03	0.02	0.05
Coefficient of Thermal Expansion α^1 α^2	ASTM-D-3386	 10^{-6}/°C 10^{-6}/°C	 35.0 98.9	 39.4 111.5	 31.2 97.9
Glass Transition Temperature	ASTM-D-3418	°C	86	68	115
Thermal Conductivity	ASTM-D-2214	W/m.K Btu-in/hr-ft^2-°F	1.25 8.7	1.02 7.1	1.28 8.9
Temperature Range of Use		°C	-40 to +130	-65 to +105	-55 to +155
Outgassing(1) TML CVCM	ASTM-E-595	 % %	 0.25 0.01		 0.29 0.02
Dielectric Strength	ASTM-D-149	kV/mm V/mil	14.4 365	14.8 375	15.0 380
Dielectric Constant @ 1 mHz	ASTM-D-150	-	5.01	5.36	5.36
Dissipation Factor @ 1 mHz	ASTM-D-150	-	0.028	0.051	0.043
Volume Resistivity @ 25°C	ASTM-D-257	Ohm-cm	>10^{15}	>10^{15}	>10^{15}

(1) per NASA Reference Publication 1124. Samples tested were cured for 24 hours @ 25°Cusing Catalyst 9, and 4 hours @ 80°C using Catalyst 11.

Storage and Handling:

The shelf life of STYCAST 2850 FT is 12 months at 25°C. For best results, store in original, tightly covered containers. Storage in cool, clean and dry areas is recommended. Usable shelf life may vary depending on method of application and storage temperature. Certain resins and hardeners are prone to crystallization. If crystallization does occur, warm the contents of the shipping container to 50-60°C until all crystals have dissolved. Be sure the shipping container is loosely covered during the warming stage to prevent any pressure build-up. Allow contents to cool to room temperature before continuing.

Health and Safety:

The STYCAST 2850 FT, like most epoxy compounds possesses the ability to cause skin and eye irritation upon contact. Certain individuals may also develop an allergic reaction after exposure (skin contact, inhalation of vapors, etc.) which may manifest itself in a number of ways including skin rashes and an itching sensation. Handling this product at elevated temperatures may also generate vapors irritating to the respiratory system.

Good industrial hygiene and safety practices should be followed when handling this product. Proper eye protection and appropriate chemical resistant clothing should be worn to minimize direct contact. Consult the Material Safety Data Sheet (MSDS) for detailed recommendations on the use of engineering controls and personal protective equipment.

This information is only a brief summary of the available safety and health data. Thoroughly review the MSDS for more complete information before using this product.

Attention Specification Writers:
The values contained herein are considered typical properties only and are not intended to be used as specification limits. For assistance in preparing specifications, please contact Emerson & Cuming Quality Assurance for further details.

Europe
Nijverheidsstraat 7
B-2260 Westerlo
Belgium
☎ : +(32)-(0) 14 57 56 11
Fax: +(32)-(0) 14 58 55 30

North America
46 Manning Road
Billerica, MA 01821
☎ : 978-436-9700
Fax : 978-436-9701

Asia-Pacific
100 Kaneda, Atsugi-shi
Kanagawa-ken, 243-0807
Japan
☎ : (81) 46-225-8815
Fax : (81) 46-222-1347

1755-2850-FT/06-01

References

[1] L. Reichl, *A Modern Course in Statistical Physics*. University of Texas Press, 1980.

[2] H. Stanley, *Introduction to Phase Transitions and Critical Phenomena*. Clarendon Press, 1971.

[3] W. Allis and H. Melvin, *Thermodynamics and Statistical Mechanics*. McGraw Hill Inc., 1952.

[4] A. Carter, *Classical an Statistical Thermodynamics*. Pretence-Hall Inc., 2001.

[5] F. Schwabl, *Statistical Mechanics 2nd Edition*. Springer, 2006.

[6] T. Barron, J. Collins, and G. White, "Thermal-Expansion of Solids at Low-Temperatures," *Advances in Physics*, vol. 29, no. 4, pp. 609–730, 1980.

[7] J. Dunn, "Ultra-low temperature dilatometry," 2010.

[8] B. Yates, *Thermal Expansion*. Plenum Press, 1972.

[9] G. M. Schmiedeshoff, A. W. Lounsbury, D. J. Luna, S. J. Tracy, A. J. Schramm, S. W. Tozer, V. F. Correa, S. T. Hannahs, T. P. Murphy, E. C. Palm, A. H. Lacerda, S. L. Bud'ko, P. C. Canfield, J. L. Smith, J. C. Lashley, and J. C. Cooley, "Versatile and compact capacitive dilatometer," *Review of Scientific Instruments*, vol. 77, DEC 2006.

[10] F. Pobell, *Matter and Methods at Low Temperatures 2nd Ed.* Springer, 1996.

[11] J. J. Neumeier, R. K. Bollinger, G. E. Timmins, C. R. Lane, R. D. Krogstad, and J. Macaluso, "Capacitive-based dilatometer cell constructed of fused quartz for measuring the thermal expansion of solids," *Rev. of Sci. Instr.*, vol. 79, MAR 2008.

[12] M. Okaji, N. Yamada, K. Nara, and H. Kato, "Laser Interfermoic Dilatometer at Low-Temperatures - Application to Fused-Silica SRM-739," *Cryogenics*, vol. 35, pp. 887–891, DEC 1995.

[13] R. Corrucini and J. Gniewek, *Thermal Expansion of Technical Solids at Low Temperature.* National Bureau of Standards 29, May 1961.

[14] D. Smith and F. Fickett, "Low-Temperature Properties of Silver," *Journal of Research of the National Institute of Standards and Technology*, vol. 100, pp. 119–171, MAR-APR 1995.

[15] M. Audley, W. Holland, T. Hodson, M. MacIntosh, I. Robson, K. Irwin, G. Hilton, W. Duncan, C. Reintsema, A. Walton, W. Parkes, P. Ade, I. Walker, M. Fich, J. Kycia, M. Halpern, D. Naylor, G. Mitchell, and P. Bastien, "An update on the SCUBA-2 project," in *Millimeter and Submillimeter Detectors for Astronomy II* (Zmuidzinas, J and Holland, WS and Withington, S, ed.), vol. 5498 of *Proceedings of the Society of Photo-Optical Instrumentation Engineers (SPIE))*, pp. 63–77, SPIE, 2004. Conference on Millimeter and Submillimeter Detectors for Astronomy II, Glasgow, SCOTLAND, JUN 23-25, 2004.

[16] R. Pott and R. Schefzyk, "Apparatus for Measuring the Thermal-Expansion of Solids Between 1.5 and 380 K," *Journal of Phys. E-Sci. Instr.*, vol. 16, no. 5, pp. 444–449, 1983.

[17] V. Leus and D. Elata, "Fringing field effect in electrostatic actuators," tech. rep., Irael Institute of Technology, Faculty of Mechanical Engineering, May 2004.

[18] E. Kuester, "Explicit Approximations for the Static Capacitance of a Microstrip Patch of Arbitrary Shape," *J. of Electromagnetic Waves and Applications*, vol. 2, no. 1, pp. 103–135, 1988.

[19] G. White, *Experimental Techniques in Low-Temperature Physics 3rd. Ed.* Clarendon Press, 1979.

[20] E. Marquardt, J. Le, and R. Radebaugh, "Cryogenic matieral properties database," 2000.

[21] D. Zhu and H. Weng, "Thermal-Conductivity and Heat-Capacity Study of a Densified A-SiO2," *J. of Non-Crystalline Solids*, vol. 185, pp. 262–267, JUN 1995.

[22] Value taken from distributor's website http://www.quartzlabware.com/.

[23] D. Bitko, T. Rosenbaum, and G. Aeppli, "Quantum critical behavior for a model magnet," *Phys. Rev. Lett.*, vol. 77, pp. 940–943, JUL 29 1996.

[24] J. L. Dunn, C. Stahl, A. J. Macdonald, K. Liu, Y. Reshitnyk, W. Sim, and R. W. Hill, "Testing the transverse field Ising model in LiHoF4 using capacitive dilatometry," *Phys. Rev. B*, vol. 86, SEP 24 2012.

[25] S. Sachdev, *Quantum Phase Transitions.* Cambridge University Press, 1999.

[26] S. M. A. Tabei, M. J. P. Gingras, Y. J. Kao, and T. Yavors'kii, "Perturbative quantum Monte Carlo study of LiHoF(4) in a transverse magnetic field," *Phys. Rev. B*, vol. 78, NOV 2008.

[27] P. Hansen, T. Johansson, and R. Nevald, "Magnetic-Properties of Lithium Rare-Earth Flourides - Ferromagnetism in LiErF4 and LiHoF4 and Crystal-Field Parameters at Rare-Earth and Li Sites," *Phys. Rev. B*, vol. 12, no. 11, pp. 5315–5324, 1975.

[28] G. Mennenga, L. Dejongh, and W. Huiskamp, "Field-Dependent Specific-Heat Study of the Dipolar Ising Ferromagnet LiHoF4," *Journal of Magnetism and Magnetic Materials*, vol. 44, no. 1-2, pp. 59–76, 1984.

[29] A. Cooke, D. Jones, J. Silva, and M. Wells, "Ferromagnetism in Lithium Holmium Flouride - LiHoF4 .1. Magnetic Measurements," *Journal of Physics C-Solid State Physics*, vol. 8, no. 23, pp. 4083–4088, 1975.

[30] P. Chakraborty, P. Henelius, H. Kjønsberg, A. Sandvik, and S. Girvin, "Theory of the magnetic phase diagram of lihof$_4$," *Phys. Rev. B*, vol. 70, no. 144411, p. 144411, 2004.

[31] H. M. Rønnow, J. Jensen, R. Parthasarathy, G. Aeppli, T. Rosenbaum, D. McMorrow, and C. Kraemer, "Magnetic excitations near the quantum phase transisiotn in the ising ferromagnet lihof$_4$," *Phys. Rev. B*, vol. 75, no. 054426, p. 054426, 2007.

[32] H. Rønnow, R. Parthasarathy, J. Jensen, G. Aeppli, T. Rosenbaum, and D. McMorrow, "Quantum phase transition of a magnet in a spin bath," *Science*, vol. 308, 2005.

[33] S. Salaün, M. T. Fornoni, A. Bulou, M. Rousseau, P. Simon, and J. Y. Gesland, "Lattice dynamics of fluoride scheelites: I. raman and infrared study of liyf$_4$ and lilnf$_4$ (ln = ho, er, tm and yb)," *J. Phys.: Cond. Matt.*, vol. 9, no. 32, p. 6941, 1997.

[34] J. Magariño, J. Tuchendler, P. Beauvillain, and I. Laursen, "Epr experiments in litb$f4$, liho$f4$, and lier$f4$ at submillimeter frequencies," *Phys. Rev. B*, vol. 21, pp. 18–28, Jan 1980.

[35] H. P. Christensen, "Spectroscopic analysis of liho$f$4 and lier$f$4," *Phys. Rev. B*, vol. 19, pp. 6564–6572, Jun 1979.

[36] Purchased from TYDEX, J.S.Co., St. Petersburg, Russia. http://www.tydexoptics.com/.

[37] B. L. Brandt, D. W. Liu, and L. G. Rubin *Rev. Sci. Instrum.*, vol. 70, p. 104, 1999.

[38] E. Burzurí, F. Luis, B. Barbara, R. Ballou, E. Ressouche, O. Montero, J. Campo, and S. Maegawa, "Magnetic dipolar ordering and quantum phase transition in an fe$_8$ molecular magnet," *Phys. Rev. Lett.*, vol. 107, p. 097203, Aug 2011.

[39] H. Takatsu, H. Kadowaki, T. J. Sato, J. W. Lynn, Y. Tabata, T. Yamazaki, and K. Matsuhira, "Quantum spin fluctuations in the spin-liquid state of Tb2Ti2O7," *J.Phys Cond. Matter*, vol. 24, Feb 8 2012.

[40] A. Yaouanc, P. D. de Reotier, Y. Chapuis, C. Marin, S. Vanishri, D. Aoki, B. Fak, L. P. Regnault, C. Buisson, A. Amato, C. Baines, and A. D. Hillier, "Exotic transition in the three-dimensional spin-liquid candidate Tb2Ti2O7," *Phys. Rev. B*, vol. 84, Nov 4 2011.

[41] N. Hamaguchi, T. Matsushita, N. Wada, Y. Yasui, and M. Sato, "Low-temperature phases of the pyrochlore compound Tb2Ti2O7," *Phys. Rev. B*, vol. 69, Apr 2004.

[42] J. S. Gardner, M. J. P. Gingras, and J. E. Greedan, "Magnetic pyrochlore oxides," *Reviews of Modern Physics*, vol. 82, pp. 53–107, Jan-Mar 2010.

[43] R. Melko and M. Gingras, "Monte Carlo studies of the dipolar spin ice model," *Journal of Physics - Condensed Matter*, vol. 16, pp. R1277–R1319, NOV 3 2004.

[44] M. Gingras, B. den Hertog, M. Faucher, J. Gardner, S. Dunsiger, L. Chang, B. Gaulin, N. Raju, and J. Greedan, "Thermodynamic and single-ion properties of Tb3+ within the collective paramagnetic-spin liquid state of the frustrated pyrochlore antiferromagnet Tb2Ti2O7," *Phys. Rev. B*, vol. 62, pp. 6496–6511, Sep 1 2000.

[45] J. Gardner, S. Dunsiger, B. Gaulin, M. Gingras, J. Greedan, R. Kiefl, M. Lumsden, W. MacFarlane, N. Raju, J. Sonier, I. Swainson, and Z. Tun, "Cooperative paramagnetism in the geometrically frustrated pyrochlore antiferromagnet Tb2Ti2O7," *Phys. Rev. Lett.*, vol. 82, pp. 1012–1015, Feb 1 1999.

[46] Y. Chapuis, "Frustration gomtrique, transitions de phase et ordre dynamique," 2009.

[47] T. Taniguchi, H. Kadowaki, H. Takatsu, B. Fak, J. Ollivier, T. Yamazaki, T. J. Sato, H. Yoshizawa, Y. Shimura, T. Sakakibara, T. Hong, K. Goto, L. R. Yaraskavitch, and J. B. Kycia, "Long-range order and spin-liquid states of polycrystalline Tb2+xTi2-xO7+y," *Phys. Rev. B*, vol. 87, Feb 25 2013.

[48] Y. Chapuis, A. Yaouanc, P. D. de Reotier, C. Marin, S. Vanishri, S. H. Curnoe, C. Vaju, and A. Forget, "Evidence from thermodynamic measurements for a singlet crystal-field ground state in pyrochlore Tb2Sn2O7 and Tb2Ti2O7," *Phys. Rev. B*, vol. 82, Sep 2 2010.

[49] J. P. C. Ruff, B. D. Gaulin, J. P. Castellan, K. C. Rule, J. P. Clancy, J. Rodriguez, and H. A. Dabkowska, "Structural fluctuations in the spin-liquid state of Tb(2)Ti(2)O(7)," *Phys. Rev. Lett.*, vol. 99, Dec 7 2007.

[50] L. Yin, J. S. Xia, Y. Takano, N. S. Sullivan, Q. J. Li, and X. F. Sun, "Low-temperature low-field phases of the pyrochlore quantum magnet $tb_2ti_2o_7$," *Phys. Rev. Lett.*, vol. 110, p. 137201, Mar 2013.

[51] J. Gardner, B. Gaulin, and D. Paul, "Single crystal growth by the floating-zone method of a geometrically frustrated pyrochlore antiferromagnet, Tb2Ti2O7," *J. Crystal Growth*, vol. 191, pp. 740–745, Aug 1998.

[52] I. Alkhesho, "Thermal conductivity measurement at ultra low temperatures," 2010.

[53] N. Oeschler, P. Gegenwart, F. Weickert, I. Zerec, P. Thalmeier, F. Steglich, E. Bauer, N. Frederick, and M. Maple, "B-T phase diagram of PrOs4Sb12 studied by low-temperature thermal expansion and magnetostriction," *Phys. Rev. B*, vol. 69, JUN 2004.

[54] N. Hill, "Why are there so few magnetic ferroelectrics?," *J. Phys. Chem. B*, vol. 104, pp. 6694–6709, Jul 27 2000.

[55] N. Spaldin and M. Fiebig, "The renaissance of magnetoelectric multiferroics," *Science*, vol. 309, pp. 391–392, Jul 15 2005.

[56] E. Ascher, H. Rieder, H. Schmid, and H. Stossel, "Some Properties of Ferromagnetoelectric Nickel-Iodine Boracite Ni3B7O13I," *J. App. Phys.*, vol. 37, no. 3, pp. 1404–&, 1966.

[57] V. Markovich, I. Fita, A. Shames, R. Puzniak, E. Rozenberg, Y. Yuzhelevski, D. Mogilyansky, A. Wisniewski, Y. Mukovskii, and G. Gorodetsky, "Magnetic, electric

and electron magnetic resonance properties of orthorhombic self-doped La1-xMnO3 single crystals," *Journal of Physics - Condensed Matter*, vol. 15, pp. 3985–4000, JUN 18 2003.

[58] T. Mizokawa, D. Khomskii, and G. Sawatzky, "Interplay between orbital ordering and lattice distortions in LaMnO3, YVO3, and YTiO3," *Phys. Rev. B*, vol. 60, pp. 7309–7313, SEP 1 1999.

[59] M. Iliev, H. Lee, V. Popov, M. Abrashev, A. Hamed, R. Meng, and C. Chu, "Raman- and infrared-active phonons in hexagonal YMnO3: Experiment and lattice-dynamical calculations," *Phys. Rev. B*, vol. 56, pp. 2488–2494, Aug 1 1997.

[60] N. Hill and A. Filippetti, "Why are there any magnetic ferroelectrics?," *J. Magnetism and Magnetic Mat.*, vol. 242, pp. 976–979, Apr 2002. Joint European Magnetic Symposia (JEMS 01), GRENOBLE, FRANCE, Aug 28-Sep 01, 2001.

[61] S. Kim, S. Lee, T. Kim, T. Zyung, T. Jeong, and M. Jang, "Growth, ferroelectric properties, and phonon modes of YMnO3 single crystal," *Crystal Research and Technology*, vol. 35, no. 1, pp. 19–27, 2000.

[62] K. Marty, P. Bordet, V. Simonet, M. Loire, R. Ballou, C. Darie, J. Kljun, P. Bonville, O. Isnard, P. Lejay, B. Zawilski, and C. Simon, "Magnetic and dielectric properties in the langasite-type compounds: A(3)BFe(3)D(2)O(14) (A = Ba, Sr, Ca; B = Ta, Nb, Sb; D = Ge, Si)," *Phys. Rev. B*, vol. 81, Feb 2010.

[63] H. D. Zhou, L. L. Lumata, P. L. Kuhns, A. P. Reyes, E. S. Choi, N. S. Dalal, J. Lu, Y. J. Jo, L. Balicas, J. S. Brooks, and C. R. Wiebe, "Ba3NbFe3Si2O14: A New Multiferroic with a 2D Triangular Fe3+ Motif," *Chem. Mat.*, vol. 21, pp. 156–159, Jan 13 2009.

[64] K. Marty, V. Simonet, P. Bordet, R. Ballou, P. Lejay, O. Isnard, E. Ressouche, F. Bourdarot, and P. Bonville, "Magnetic characterization of the non centrosymmetric Ba3NbFe3Si2O14 langasite," *J. Magnetism and Magnetic Mat.*, vol. 321, pp. 1778–1781, Jun 2009. Symposium on Multiferroics and Magnetoelectrics Materials held at the 2008 EMRS Spring Conference, Strasbourg, FRANCE, MAY 26-30, 2008.

[65] H. Willemsen, R. Armstrong, and P. Meincke, "Thermal-Expansion Near Displacive Phase-Transition in SrTiO3," *Phys. Rev. B*, vol. 14, no. 8, pp. 3644–3648, 1976.